Accelerated Monte Carlo based Simultaneous Dual-isotope SPECT Reconstruction

ACCELERATED MONTE CARLO BASED SIMULTANEOUS DUAL-ISOTOPE SPECT RECONSTRUCTION

BY

MUHAMMAD IRFAN KARAMAT, M.Sc.

A THESIS

SUBMITTED TO THE DEPARTMENT OF MEDICAL PHYSICS & APPLIED RADIATION SCIENCES

AND THE SCHOOL OF GRADUATE STUDIES

OF MCMASTER UNIVERSITY

IN PARTIAL FULFILMENT OF THE REQUIREMENTS

FOR THE DEGREE OF

MASTER OF APPLIED SCIENCE

Master of Applied Science (2012) McMaster University
(Medical Physics & Applied Radiation Sciences) Hamilton, Ontario, Canada

TITLE:	Accelerated Monte Carlo based Simultaneous Dual-isotope SPECT Reconstruction
AUTHOR:	Muhammad Irfan Karamat M.Sc., Medical Physics) McMaster University, Hamilton, Canada
SUPERVISOR:	Dr. Troy H. Farncombe
NUMBER OF PAGES:	xxii, 112

To my parents Karamat Ali and Shahnaz Begum, my wife Bushra Irfan and my lovely and incredible daughter Areeba Karamat

Abstract

Simultaneous dual-isotope SPECT imaging has a number of applications, for example, cardiac, brain and cancer imaging. The major concern in simultaneous dual-isotop SPECT acquisition is the significant crosstalk contamination between the different isotopes used. The current study focuses on a method of crosstalk compensation between two isotopes in simultaneous dual isotope SPECT acquisition applied to cancer imaging using ^{99m}Tc/^{111}In and breast SPECT using ^{99m}Tc/^{123}I. Monte Carlo (MC), which is thought to offer the most realistic crosstalk and scatter compensation modelling, in typical implementations, has inherent long calculation times (often several hours or days) associated with it. This makes MC unsuitable for clinical applications. We have previously incorporated convolution based forced detection into SIMIND Monte Carlo program which have made MC feasible to use in clinical time frames. In order to evaluate the accuracy of our accelerated MC program a number of point source simulation results were compared to experimentally acquired data in terms of spatial resolution and detector sensitivity. We have developed an iterative MC-based image reconstruction technique that simulates the photon down-scatter from one isotope into the acquisition window of a second isotope. The MC based estimation of scatter contamination contained in projection views is then used to compensate for the photon contamination during iterative reconstruction. We used a modified ordered subset-expectation maximization (OSEM), named as simultaneous ordered subset-expectation maximization (Sim-OSEM), to perform this step. We have undertaken a number of simulation tests and phantom studies to verify this approach in case of both of the dual-isotope combinations (i.e. ^{99m}Tc/^{111}In and ^{99m}Tc/^{123}I). In breast SPECT studies three different breast sizes were simulated. For each of the breast sizes ten combinations of lesions with 3 lesions per combination, were selected randomly for acquisition and reconstruction of simulation data. The images reconstructed using Sim-OSEM showed crosstalk compensation when compared with images reconstructed using simultaneously (with crosstalk) acquired projection data using analytical attenuation based reconstruction. In case of Sim-OSEM the lesion to background ratios were much closer to actual values compared to images reconstructed for both separately (without crosstalk) and simultaneously (with crosstalk) acquired projection data using analytical attenuation based reconstruction. Activity estimation is also possible with Sim-OSEM and yielded accurate estimates of lesion activities with relatively small error compared to deposited activities. The proposed reconstruction technique also evaluated by reconstruction of experimentally acquired projection phantom data in case of ^{99m}Tc/^{111}In. Reconstruction using Sim-OSEM showed very promising results in terms of crosstalk and scatter compensation and uniformity of background compared to analytical attenuation based reconstruction after triple energy window (TEW) based scatter correction of projection data. In our case images obtained using Sim-OSEM showed better small angle scatter compensation and more uniform background even compared to the images reconstructed for separately acquired projection data using analytical attenuation based reconstruction.

Acknowledgements

All the praise for Allah, *The beneficent*, *The Merciful* who guides us in darkness and helps us in difficulties. I firmly believe that Allah never spoils any effort.

All and every kind of praise is for Holy Prophet (PBUH) who is really a source of light for awareness of our minds.

I would like to thank Department of Medical Physics and Applied Radiation Sciences and Hamilton Heath Sciences for giving me chance and privilege to study at one of the top universities of the world.

This work would not have been possible without the funding from numerous organizations. I would like to acknowledge the financial support provided by the Ontario Institute Cancer Research (OICR) under Smarter Imaging Program. I would also like to acknowledge Government of Ontario for providing funds in part for this work.

My deep sense of gratitude and thanks for my research supervisor, Dr. Troy Farncombe for providing me guidance, support, advice and every kind of help in my research work. I feel myself more researcher in his company and supervision.

I express my heart felt gratitude to my teachers and instructors for their exceptional teaching and guidance during the course of my degree.

My great thanks goes to supervisory committee members, Dr. Tom Farrell and Dr. Hao Peng for their guidance, help and time during the course of this work.

I greatly appreciate the help and suggestions from all of my colleagues in Medical Imaging and Instrumentation Group.

I am thankful to staff at Nuclear Medicine Department, McMaster University Medical Center (MUMC) especially Cherryl, Scott, Sandra, Sue and Rania for helping and assisting me in the experiments performed during this work. I would like also to thank administrative staff at Department of Medical Physics and Applied Radiation Sciences and Nuclear Medicine Department at MUMC for helping and facilitating me during the course of this work.

I extend my heart-felt gratitude and special regards to my most respectable and affectionate parents, Karamat Ali and Shahnaz Begum. Although they are no longer in this world but their prayers love and affection will remain an invaluable asset for me. I believe all of my achievements and success are due to their blessings and prayers.

I am grateful to my wife, Bushra for her support encouragement and sacrifices. I can just imagine the difficulties and pains she faced all alone, without me back home in Pakistan. My love and thanks to my daughter Areeba, her birth is the happiest thing in my life. I feel sorry for her as she has to spent almost two beautiful years of her life without me. My regards and love to my mother in law and phopho Riaz Begum, for her prayers and great thanks to her for looking after my family in my absence. Finally I would like to thank my brothers, sisters and friends who always prayed for my success and betterment.

Muhammad Irfan Karamat

February, 2012

List of Abbreviations

CFD	convolution forced detection
cps	counts per second
EGS	electron gamma shower
ETRAN	electron transport
FBP	filtered back-projection
FD	forced detection
FWHM	full with at half maximum
GEANT	geometry and tracking
ITS	integrated tiger series
IEC-NEMA	International Electro-technical Commission and National Electrical Manufacturing Association
JOSEM	Joint order subset expectation maximization
LEHR	low energy high resolution
MC	Monte Carlo
MCNP	Monte Carlo nuclear particle transport
MEGP	medium energy general purpose
MLEM	maximum likelihood expectation maximization
NCAT	nurbs-based cardiac torso phantom
OSEM	ordered subset expectation maximization
PDF	probability density function
PET	positron emission computed tomography
PMT	photomultiplier tube
PSF	point spread function
SPECT	single photon emission computed tomography
Sim-OSEM	simultaneous ordered subset expectation maximization
TEW	triple energy window
VRT	variance reduction technique

Contents

List of Tables

List of Figures

Chapter 1

Preface

Single photon emission computed tomography (SPECT) is a type of functional imaging uses radioisotopes to reveal physiological and anatomical information. In SPECT studies, the radioisotope labelled with a pharmaceutical (radiopharamceutical) is administered to the patient via different routes (e.g. intravenous, oral and inhalation) The pharmaceutical guides the radioisotope to the organ, tissue or system to be imaged. SPECT has number of applications, examples of some such applications are scanning of bones for metastasis or other bone anomalies, myocardial scan to study the function and perfusion of cardiac muscle and brain imaging performed to look for the presence of tumour or to study different mental conditions.

The current study focusses on the reconstruction of the simultaneously acquired dual isotope SPECT data. In dual isotope SPECT data crosstalk between the isotopes is the problem and this work proposes a reconstruction based crosstalk compensation solution for this problem.

Chapter 2 of this thesis gives an overview of the different steps involved in nuclear medicine imaging specifically SPECT. It also gives a brief account of equipment and tools required for SPECT data acquisition and reconstruction of the data to get 3D map of deposited activity.

The detailed account of dual isotope SPECT and its applications is given in chapter 3. As this work mainly deals with two combinations of dual isotopes namely, ^{111}In/^{99m}Tc (cancer imaging) and ^{123}I/^{99m}Tc (breast tomoscintigraphy). The chapter describes in detail the severity of crosstalk effect in both the combinations. The solutions to correct for the effects proposed by different researchers and research groups are briefly discussed in the chapter.

The materials and methods for simultaneous SPECT acquisition and subsequent reconstruction for dual isotope combinations (i.e. ^{111}In/^{99m}Tc and ^{123}I/^{99m}Tc) studied in this work are described in the chapter 4. The chapter gives a detailed description of Monte Carlo (MC) methods in SPECT imaging and variance reduction techniques (VRTs) used to make MC faster. The detailed description of the proposed dual isotope reconstruction algorithm named as simultaneous ordered subset expectation maximization (Sim-OSEM), were also provided in this chapter. The method uses accelerated MC to correct for the crosstalk between the isotopes in dual isotope SPECT. The description of phantoms used in simulation and experimental acquisition of data is also included in this chapter.

The chapter 5 contains the details of results obtained for all the isotope duos used in this work and their related discussions.

Final chapter of this thesis describes the conclusions of this work and future directions.

Chapter 2

Nuclear Medicine Imaging Basics

Nuclear medicine involves therapeutic and diagnostic use of radionuclides. This work will focus only on the diagnostic aspect of nuclear medicine. In diagnostic nuclear medicine trace amounts of radioactivity is administered in order to provide informations of diagnostic importance. There are two main classes of nuclear medicine imaging, Single Photon Emission Computed Tomography (SPECT) and Positron Emission Tomography (PET). In nuclear medicine imaging a radionuclide (gamma ray or positron emitter) is tagged with a target-specific pharmaceutical, called as a radiopharmaceutical and is administered to a patient. With the decay of the administered radiopharmaceutical gamma rays are emitted and detected using an external gamma camera. This work mainly focusses on SPECT imaging which involves the use of gamma ray emitting radionuclides. A schematic of SPECT imaging from radiotracer synthesis to SPECT data acquisition is shown in Figure 2.1. The final step in nuclear medicine imaging using SPECT projection data is the reconstruction of the data with the help of different reconstruction algorithms. All the steps involved in SPECT will be discussed briefly in the following paragraphs.

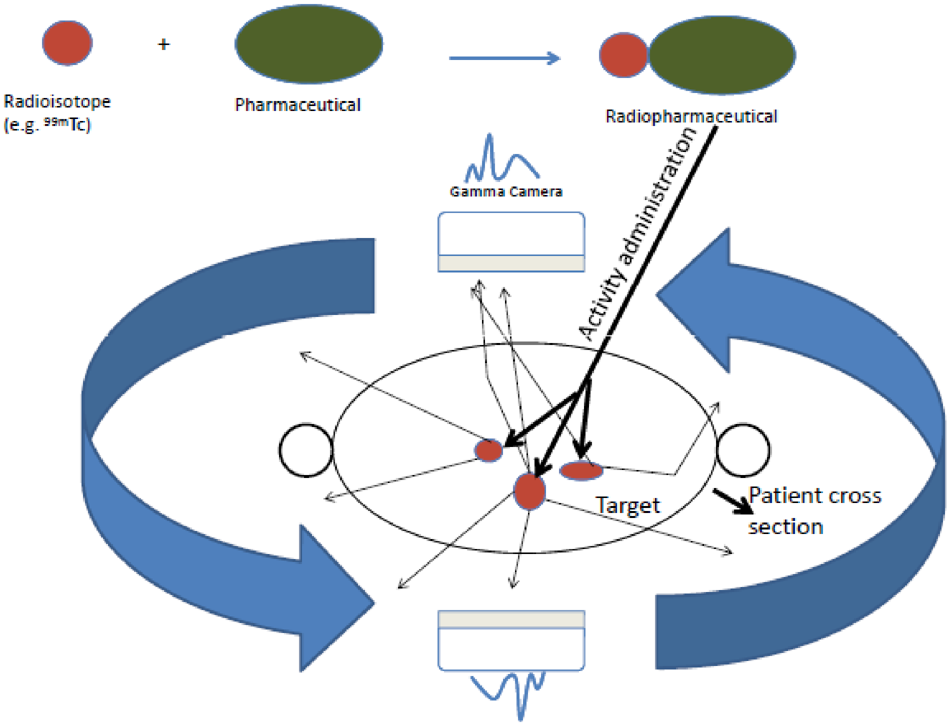

Figure 2.1: Schematic of SPECT from radiopharmaceutical synthesis to acquisition of SPECT projection data.

2.1 Radioisotope Selection

Radioisotopes used in nuclear medicine in their elemental form generally do not reach target organs if administered directly into the patient. One of very a few example of radionuclides which can be administered in its elemental form is ^{131}I. Iodine (^{131}I) is used in thyroid imaging. Thus radionuclides are almost always injected in the form of *radiopharmaceuticals* (radionuclide labeled to a pharmaceutical). The factors which are involved in the selection of a relevant radionuclide includes, type and energy of emission, half life, the specific activity, radionuclidic, chemical properties of the radionuclide and cost of production [1].

In SPECT, the type of radiation involved are gamma rays. The suitable gamma ray energy range used in SPECT imaging is 50-363 keV.

The physical half life is another important consideration in radioisotope selection. The suitable half life for SPECT imaging is preferably on the order of minutes to hours. The physical half life should be neither too short to give sufficient time for radiopharmaceutical synthesis and injection to the patient nor too long as to cause prolonged data acquisition time to get reasonable number of counts, increased radiation dose to the patient and pose storage and disposal problems.

The specific activity defined as activity per unit mass of the substance is another important factor to be considered in selection of an appropriate radioisotopes. As nuclear medicine relies on the radiotracer doses that do not interfere with biological systems under study, radioisotopes available in high specific activity are required for nuclear medicine imaging.

Radionuclidic contaminants which are often produced during synthesis of a desired radionuclide pose problems such as increased patient dose and detector issues. High radionuclidic purity, defined in Equation 2.1, is essential for radionuclide used in nuclear medicine applications.

$$\text{Radionuclidic Purity} = \frac{\text{Activity of desired radionuclide in a given sample}}{\text{Total activity present in given sample}} \tag{2.1}$$

For example in the case of ^{99}Mo/^{99m}Tc generator the acceptable radionuclidic purity is >99.985% [1]. A list some important radionuclides with their half lives are given in Table 2.1. The chemical properties such as ability to produce useful precursors or able to undergo a wide range of chemical synthesis are important factors in the selection of radioisotopes to be used in SPECT. However, some elements (e.g. metals such as ^{99m}Tc and ^{67}Ga) are chosen on the basis of their desirable imaging properties. For

Table 2.1: Some commonly used SPECT radioisotopes.

Radioisotope	**Half life**
^{99m}Tc	6.02 hrs
^{123}I	13.3 hrs
^{111}In	67.2 hrs
^{201}Tl	72.9 hrs
^{67}Ga	78.1 hrs
^{133}Xe	125.8 hrs

elements selected on the basis of their suitability for imaging the different technique have been developed to shield the metal atom from the biological active sites of the molecule.

The cost of production of radionuclide is another important factor in the selection of radioisotopes. As has been mentioned previously, radionuclides are almost always used in the form of radiopharmaceuticals (radioisotope labelled to pharmaceutical). The loss of specific activity during radiopharmaceutical synthesis is an important factor when considering a pharmaceutical or method of preparation of that pharmaceutical.

Radiochemical and chemical purity also play an important role in the evaluation of a radiopharmaceutical. Radiochemical purity defined as fraction of the activity present in a given sample in desired chemical form. Radiochemical impurities often arise from the competing reactions or due to radiation induced chemical reactions during the synthesis of the radiopharmaceutical.

2.2 Nuclear Medicine Image Acquisition

The first step in nuclear medicine imaging is to administer a radiopharmaceutical into the patient. The next step is to detect emitted photons using an external detection

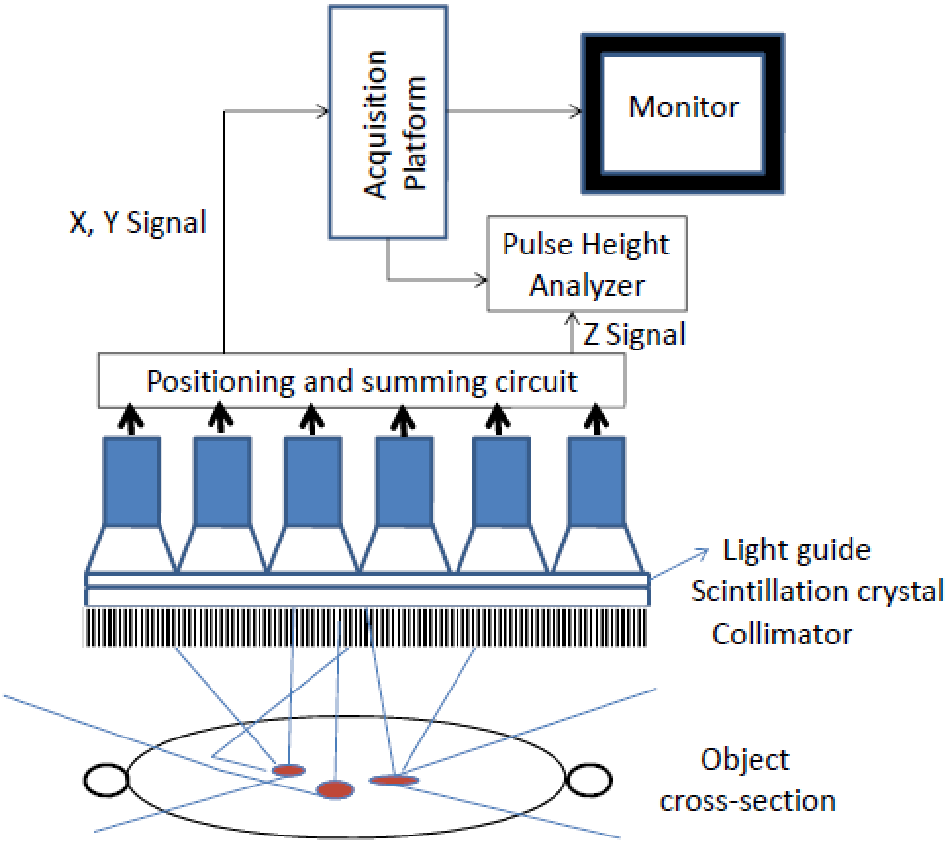

Figure 2.2: Schematic of gamma camera for SPECT.

system. This external detector is known as a gamma camera. The main components of the gamma camera include the collimator, scintillation crystal, photomultiplier tubes, positioning and summing circuits and a computer. Figure 2.2 shows a schematic of a gamma camera.

2.2.1 Collimator

In order to image the activity distribution accurately the selective absorption of γ-rays is performed with the help of a collimator. A collimator is an essential part of a SPECT gamma camera as it develops a correspondence between the position of an emission event within the object and its detected position on the detector crystal.

A collimator consists of a lead (Pb) honeycomb in which the photons parallel to the hole orientation can pass through and γ-rays that hit the collimator walls (known as septa) generally get absorbed. Collimators are generally categorized on the basis of their holes orientation and energy range. Most collimators fall into the following four categories shown in Figure 2.3.

1. **Pinhole collimator** consists of a small pinhole aperture in a piece of lead as shown in Figure 2.3(a). Similar to a *box camera* which helps in magnifying image of small size objects. Frequently used in paediatric and small animal imaging.

2. **Parallel hole collimator** is the most commonly used collimator type in SPECT imaging and is shown in Figure 2.3(b). Lead septa generally prevent γ-rays from penetration. It projects the activity distribution without any kind of size modifications.

3. **Converging collimator** are used to project magnified, non-inverted image of the activity distribution as shown in Figure 2.3(c). This kind of collimator is often used to produce a magnified image of small or overlapping organs.

4. **Diverging collimator** is shown in Figure 2.3(d) and is often used in small crystal gamma cameras to image large organs such as liver and lung in one projection.

Parallel hole collimators are the most commonly used and can be specified completely by lattice structure of the hole pattern and three parameters namely, i) collimator thickness (T), ii) the hole separation ($HoleSep$) and iii) the hole size l (in case of

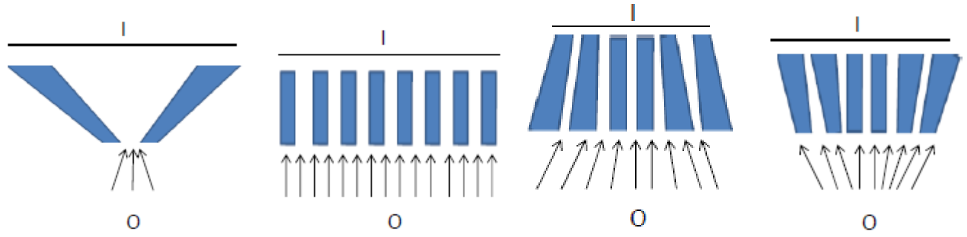

(a) Pinhole (b) Parallel (c) Converging (d) Diverging

Figure 2.3: Collimator types based on hole orientation. o denoted object and I denotes corresponding image

hexagonal holes face to face distance ($f2f$) where$f2f = \sqrt{3}l$). Three typical hole patterns involved i) hexagonal holes in hexagonal array shown in Figure 2.4(a), ii) square holes in a square array shown in Figure 2.4(b) and iii) triangular holes in point to point array shown in Figure 2.4(c). Among all the holes orientation and shapes

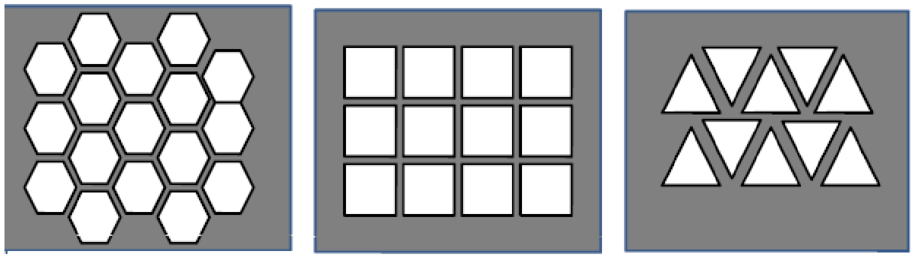

(a) Hexagonal (b) Square (c) Triangular

Figure 2.4: Different collimator hole shapes with hexagonal, square and triangular unit cells.

parallel hole collimator with hexagonal holes is the most widely used collimator type.

2.2.2 Scintillation Crystal

The component next to the collimator is the detector crystal. In the detector crystal the interaction of γ-rays via photoelectric effect cause excitation of energy bands. Subsequent de-excitation of these bands gives rise to scintillation photons in the visible region. The most commonly used detector crystal material in SPECT imaging is thallium activated sodium iodide, NaI(Tl) detector. Usually one visible light photon is produced for every 23 eV of energy absorbed [2]. With photon energies >250 keV Compton scattering (discussed in Section 4.1.2) becomes the dominant mode of interaction within the crystal material, which results in reduced detection efficiency.

2.2.3 Photomultiplier Tubes (PMTs)

The photomultiplier tube (PMT) is a vacuum tube which produces a current pulse when activated by a weak light signal (schematic shown in Figure 2.5). The internal surface of entrance window (the photocathode) is coated with a photo-emissive material, which emits electrons when visible light photons interact with it. The typical value of quantum efficiency for photocathode, defined as number of electrons emitted per photon absorbed, is 1-3 electrons per 10 visible photons striking it. The electrons given off by the photocathodes are then accelerated through an array of metal plate

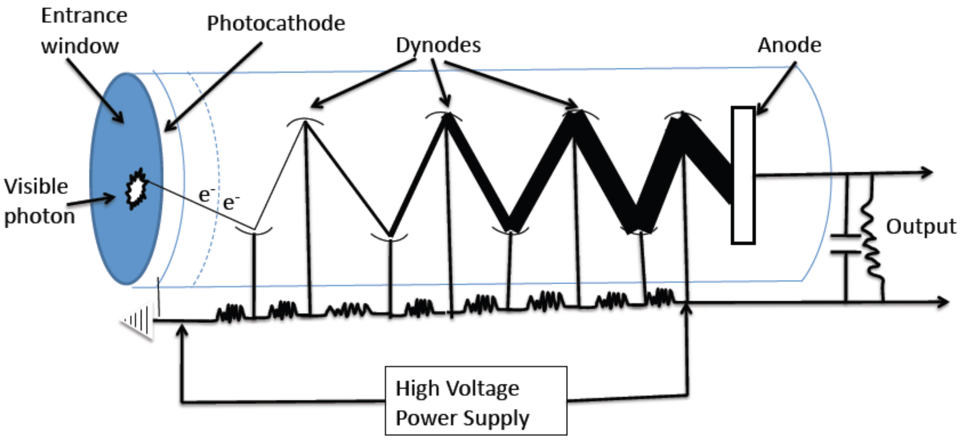

Figure 2.5: Schematic of photomultiplier tube (PMT).

with increasing potential (dynodes) whose internal surface coated with material having high secondary emission. These electrons get accelerated towards the end of the tube and get amplified to large pulse of current due to emission of secondary electrons at each dynode step. A gamma camera usually has an array of these PMT tubes.

2.2.4 Positioning and Summing Circuits

The PMT array output is fed to an event positioning system. Figure 2.6 shows a resistor based positioning of a conventional analog gamma camera. The X^+, X^-, Y^+, Y^- are combined to get X and Y position signal as given in Equation 2.2 and 2.3.

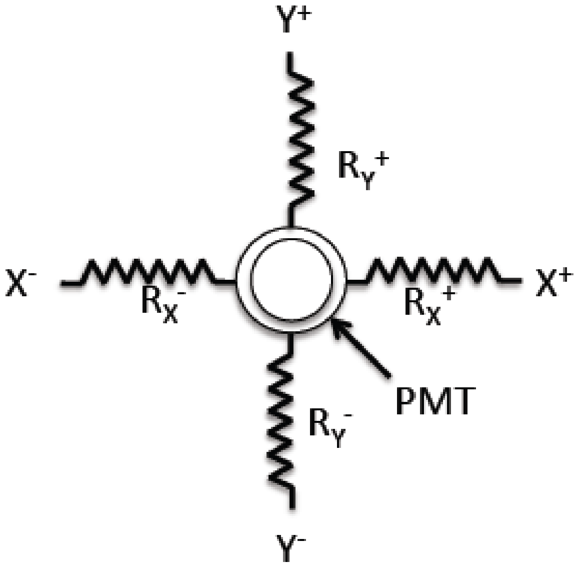

Figure 2.6: Signals for PMTs split using resistors onto four output lines, designated as X^+, X^-, Y^+, Y^-.

$$X = \frac{X^+ - X^-}{X^+ + X^-} \tag{2.2}$$

$$Y = \frac{Y^+ - Y^-}{Y^+ + Y^-} \tag{2.3}$$

The X and Y position signals are normalized in order to make the interaction position independent of the pulse height measured in terms of Z-signal and proportional to the total light produced by scintillation events in the crystal. It should be noted that nonlinearity of PMT output with interaction position, defects in crystal and reflection at the edges give rise to different artefacts (e.g. pincushion artefact). The detailed account of these artifacts can be seen in reference [3].

In modern digital cameras more sophisticated algorithms are employed to incorporate non linearities discussed above and the position of interaction is found with the help of software. A commonly used way to improve positioning accuracy include thresholding of the PMT signals. This not only allow PMT's with significant pulse height to be included in position determination but also make simultaneous event positioning possible.

2.3 Image Reconstruction Methods

The data acquired using the gamma camera at a given projection angle gives a two dimensional projection of three dimensional activity distribution. The two dimensional projection may have very little depth information but in many cases it is diagnostically useful e.g. a whole body bone scan image provides enough information as there is no tracer uptake in tissue lying above and below of skeletal system. More commonly however, in SPECT acquisition data has to be acquired. This consists of acquiring data at many different angles and estimating the underlying 3D-activity distribution using image reconstruction methods.

The reconstruction methods can be broadly categorized into two categories as i) Analytical Reconstruction and ii) Iterative Reconstruction procedures.

2.3.1 Analytical Reconstruction Procedures

One of the first attempts to perform reconstruction of 3D activity distribution analytically using 2D projection views acquired around the object was made by Radon in 1917. In this work, analytical formulation of a 2D projection in a given direction or *Radon transform* can be treated as the three dimensional integral of activity distribution along a given direction. The *inverse Radon transform* of the acquired data should give the original three dimensional activity distribution but this is not the case unless an infinite number of projections are acquired.

The simplest way to perform reconstruction is to backproject transaxial slices into transaxial image independently. This is done through the use of projection sinogram. The sinogram can be described as the stack of number of counts in each camera bin as a function of projection angle. Figure 2.7 shows sinogram of 2D Shepp Logan phantom.

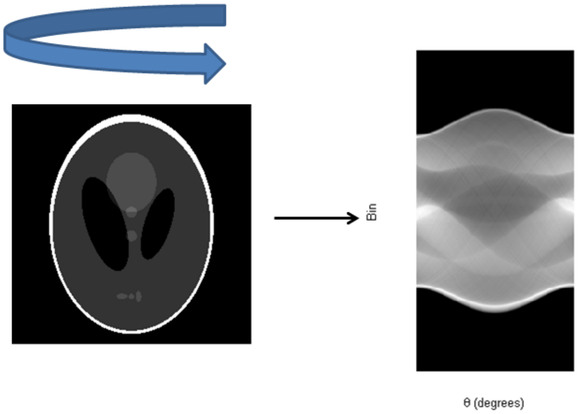

Figure 2.7: Stacking of projection data into sinogram for analytical tomographic reconstruction.

One of the most commonly used analytical reconstruction methods is the filtered backprojection (FBP). In this method the projection data is convolved with suitable filter in the spatial domain and then backprojected. In order to avoid the convolution step in spatial domain, the Fourier transform of projection data is taken. The projection data in the frequency domain is filtered by multiplying it with a low pass frequency domain filter to correct for high frequency noise. An inverse Fourier transform of the filtered data is taken and finally the filtered projection data is back-projected to get the image. The detail description of FBP and other analytical image reconstruction algorithms can be found in [4].

2.3.2 Iterative Reconstruction Procedure

Filtered back projection (FBP) is a one step process which only enable correction of data (e.g. for attenuation or scatter) with the help of filters. FBP is not able to accurately correct for other image degradation effects as scatter and attenuation. In order to avoid the inaccuracy problem associated with Radon model based reconstruction, modern iterative reconstruction algorithms can be used. These algorithms describe imaging problem as a system of linear equations. However it should be noted that in order to achieve accuracy, efficiency has to be sacrificed to some extent, as iterative algorithms are much more computation intensive compared to FBP.

The iterative algorithms involve solving a system of linear equations or minimization of an objective function (e.g. likelihood function). We can consider reconstruction of SPECT data as a *linear inverse problem* for which we can write projection data at a given angle as in Equation 2.4.

$$\mathbf{Hf} = \mathbf{p} \tag{2.4}$$

Where, $\mathbf{H}$ is the system matrix which maps a 3D activity distribution $\mathbf{f}$, to projection space to form a projection **p**.

In 2D, the system matrix, **H** in practical imaging situations is a rectangular matrix and able to represent effects such as attenuation and any other blurring mechanism. Each element h_{ij} of the system matrix **H**, can be thought to represent the mean contribution of each pixel j to each data bin i. The linear model can take into account different effects such as attenuation, detector response and scatter by considering average contribution from many pixel into one imaging bin. Whereas in case of Radon model only the contribution from a pixel along the line of response (LOR) into an imaging bin is taken into account. The system matrix is generally a large sized rectangular matrix which is usually difficult to invert and generalized inverse can be found using least-square minimization and singular value decomposition method [5].

There are a number of iterative reconstruction techniques being used for emission tomographic reconstruction. Figure 2.8 shows the flow of an iterative image reconstruction algorithm in general. The maximum likelihood expectation maximization (MLEM) or its accelerated version ordered set expectation maximization (OSEM) are the most widely used iterative algorithms and are discussed in following paragraphs.

Maximum Likelihood Expectation Maximization (MLEM)

MLEM and its variations are the leading iterative algorithm and used for a long time after its use demonstrated for SPECT in 1984 [6, 7] for first time. The algorithm is based on the fact that the emission of photon within a certain time interval from a radioactive source can described by a Poisson distribution. The detailed derivation of this algorithm can be found in reference [6]. MLEM in SPECT can be expressed

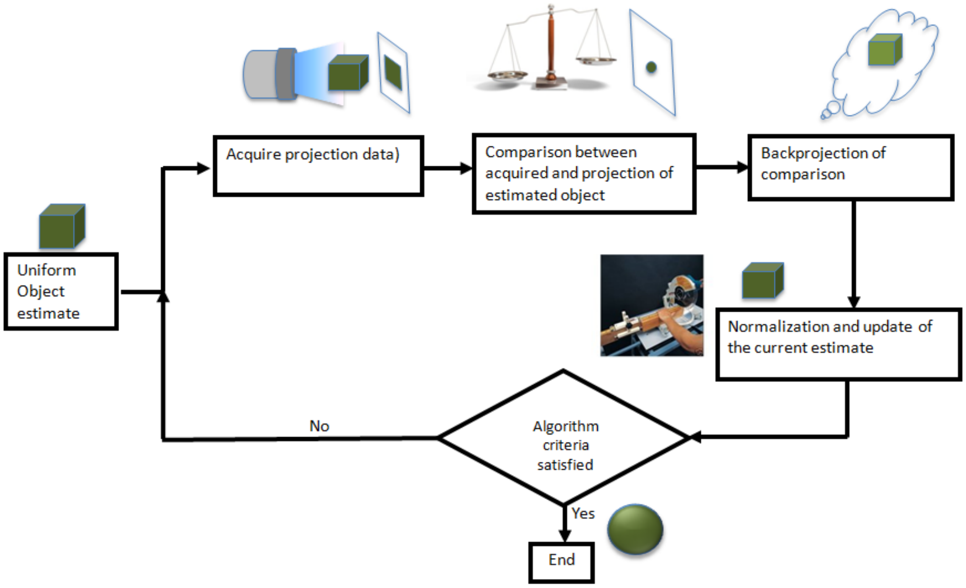

Figure 2.8: Flow diagram of iterative image reconstruction algorithms in general

as

$$f^{new} = \frac{f^{old}}{\sum H^T} \sum H^T \frac{p}{\sum H f^{old}} \tag{2.5}$$

The implementation of MLEM can be described in the following steps:

1. Consider the initial guess f^{old} of the object to be uniform map of activity or base your guess on a priori knowledge about the shape of the object.

2. Use the system matrix to forward project the current estimate of activity and compare it with the corresponding measured projection data as:

$$\frac{p}{\sum H f^{old}}$$

3. Backproject the ratio of measured and estimated projection data as:

$$\sum H^T \frac{p}{\sum H f^{old}}$$

4. Update the current estimate of object as:

$$f^{old} \sum H^T \frac{p}{\sum H f^{old}}$$

5. Normalize the updated estimate of the object to get new estimate as given in Equation 2.5.
6. Use new estimate (f^{new}) as initial guess for next iteration.
7. Terminate the iterative process either if the noise level in the reconstructed image becomes acceptable or if number of iterations reaches its maximum given value.

There are two main shortcomings of MLEM i) the convergence of the algorithm is very slow. An acceptable solution may require 30-50 iterations. ii) After many iterations MLEM algorithm tries to fit the noise present in the measured data hence degrading the reconstructed image quality. Therefore the reconstruction has to be interrupted before too much image degradation occurs. The selection of the stopping point is usually subjective and based on the user's experience.

Ordered Subset Expectation Maximization (OSEM)

As discussed earlier, convergence of MLEM is slow due to the fact that the update of the current object estimate is performed after going through the whole set of projection data. One way to accelerate the reconstruction is to increase the number of updates per iteration. This can be done by a method proposed by H.M. Hudson and R.S. Larkin [8] known as ordered subset expectation maximization (OSEM). In this algorithm projection data is divided into a number of sets known as ordered subsets and the current estimate is updated to get a new estimate after each subset. Figure 2.9 shows an example of how the projection view are divided into subsets. Note in this case there will be 4 updates per iteration using OSEM compare to 1 in

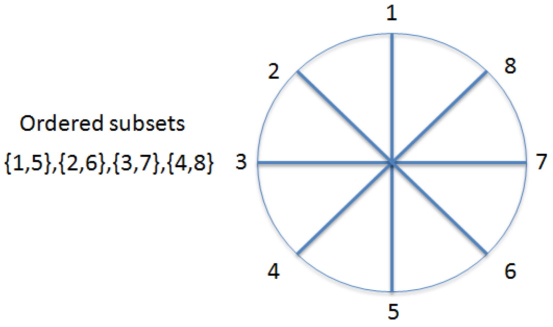

Figure 2.9: Total of 8 projection view divided into 4 subsets.

case of MLEM. OSEM which is variant of MLEM can be described by Equation 2.6.

$$f^{new} = \frac{f^{old}}{\sum_{a\epsilon s} H_a^T} \sum_{a\epsilon s} H_a^T \frac{p}{\sum_{a\epsilon s} H_a f^{old}} \tag{2.6}$$

where, s represents a ordered subset of the projection data. It is important to note that despite of all the similarities of OSEM with MLEM it is quite different from MLEM as it has no proof of convergence for the data with noise. In OSEM, the speed of convergence can be increased by increasing the number of subsets, by making the subsets size small. However the cost of improved speed is the increased noise level for the same level of bias compared to MLEM [9]. In OSEM acceleration of about 8-10 time can be achieved with very little increase in noise levels.

2.4 Sources of Image Degradation in SPECT

The factors which cause degradation of nuclear medicine images include attenuation, scatter and distance dependant collimator-detector response as well as the patient and physiological motion of organs and changes in organ positions (e.g due to respiration).

Attenuation refers to process of loss of photons due to absorption or scattering away from the detector field of view (FOV).The fraction of photons transmitted, F_T through a medium with overall attenuation coefficient, μ (cm^{-1}) over a distance x cm in the medium can be calculated using Equation 2.7.

$$F_T = e^{-\mu x} \text{ where } \mu = \int_0^x \mu(l)\, dl \tag{2.7}$$

It should be noted that the attenuation coefficient depends on the type and thickness of the medium. Therefore the presence of lung, muscle or bone will make a difference to the number of photons which are attenuated. The attenuation correction can be performed either by estimation of patient specific attenuation maps or with the use of attenuation correction algorithms incorporated into reconstruction algorithm.

The patient specific attenuation map can be estimated using one of the following strategies.

1. Import and registration of attenuation maps from other modalities such as CT [10, 11, 12].
2. Performing a transmission scan in addition to emission scan with gamma camera [13, 14, 15].
3. Estimation of attenuation map purely from the emission data [16, 17, 18].

There are a number of attenuation correction methods that have been developed which can be incorporated in analytical and iterative reconstruction algorithms [19, 20, 21, 22]. One of the techniques used to compensate for the attenuation is to use Monte Carlo simulation discussed as in Section 4.1.

The second main source of the image degradation effects are the scattered photons detected in projection data which are able to reach the detector. The scatter compensation can be performed either by modelling the scatter contribution to correct the projection data or by incorporating scatter correction function into a reconstruction algorithm.

The pre-reconstruction scatter correction methods include energy distribution based compensation on a pixel level and spatial distribution based methods use to estimate scatter contribution in projection data based on the photopeak data. Examples of energy distribution based correction are Compton window (CW) scatter compensation [23], dual photopeak energy window (DPW) scatter correction [24, 25] and triple energy window correction methods [26]. Convolution-subtraction is an example of spatial distribution based method [27].

Reconstruction based scatter correction methods are the methods that incorporate the underlying mechanisms of scatter contribution in projection data into the reconstruction process. Monte Carlo based effective scatter source estimation (ESSE) is an example of reconstruction based scatter correction method [28]. These methods are generally more accurate but have limited applicability due to complexity and require high computation speed.

The third source of image degradation is the distance dependant spatial resolution of imaging system. There are two main components of spatial resolution i) intrinsic resolution of detector and electronics, can be modelled as Gaussian function and ii) Distance dependant spatial resolution of collimator which can also be modelled again as Gaussian function excluding septal penetration and scatter. The spatial resolution compensation is performed during analytical or iterative reconstruction. In case of analytical reconstruction restoration filters such as Metz or Wiener filter are used to compensate for distance dependant collimator response to some extent [29, 30, 31]. An example of collimator response model which can be incorporated in iterative reconstruction is discussed in Section 4.2.1.

Chapter 3

Dual Isotope SPECT

Some nuclear medicine studies requires the patient to undergo several scanning procedures using different radionuclides with different emission energies. Scanning these radionuclides separately not only increases the patient discomfort but also results in the potential misregistration of images caused by patient motion. Dual-isotope imaging has a number of applications, for example, cardiac, brain and cancer [32, 33, 34, 35, 36, 37]

3.1 Simultaneous dual isotope SPECT

In order to improve system throughput, reduce patient discomfort and to avoid misregistration, simultaneous acquisition of all the radionuclides is the preferred option. SPECT imaging has the advantage over PET imaging in the fact that SPECT is able to image multiple radioisotopes simultaneously using energy discrimination. Now despite of associated advantages and multiple energy windows acquisition capabilities of SPECT the reason for infrequent use of simultaneous multi-isotope acquisition in clinical application is discussed below.

3.1.1 Issue with simultaneous dual isotope SPECT

The major concern in simultaneous dual-isotope SPECT is the significant crosstalk contamination between the multiple isotopes used. In order to understand the severity of cross-contamination issue in simultaneous dual isotope SPECT, a simple simulation exercise was performed. A small source of activity (radius = 0.88 cm) placed in the center of a non-radioactive water filled cylinder (radius = 14 cm, height= 28 cm). The simulation was performed with the source containing either ^{99m}Tc or ^{111}In and then with ^{99m}Tc and ^{123}I in equal amounts respectively. The spectrums obtained are shown in Figure 3.1(a). It was observed that 54% of the counts collected within the ^{99m}Tc photopeak were actually downscattered from ^{111}In. In order to avoid overlapping asymmetric acquisition windows (126-150 keV for ^{99m}Tc and 151-174.9 keV for ^{123}I) were used in the case of ^{99m}Tc and ^{123}I. It was observed that about 66% of counts detected under the ^{99m}Tc peak were actually downscattered from ^{123}I energy peak, whereas spillover from ^{99m}Tc into ^{123}I window was only about 3%.

3.1.2 Proposed solutions

As seen, the problem with simultaneous dual isotope SPECT is the crosstalk between the isotopes involved. Solutions proposed by different researchers and research groups are discussed in the following paragraphs.

Many researchers have previously developed different pre-reconstruction crosstalk compensation methods, which involved subtraction of a crosstalk estimate or restoration by deconvolution of crosstalk blurring function from acquired projection data.

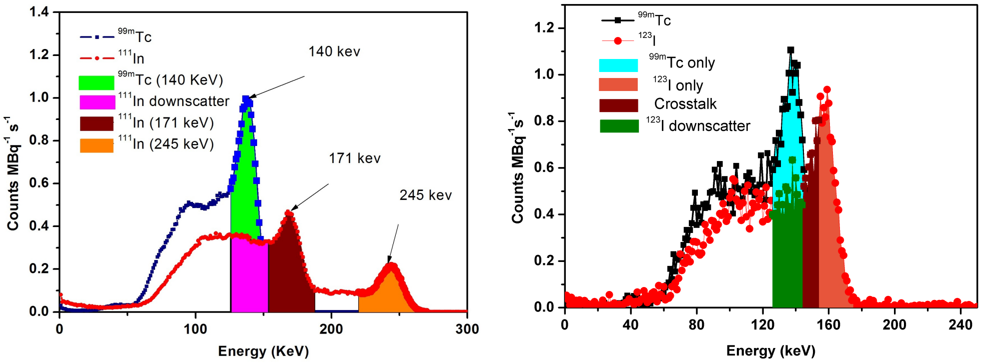

(a) (b)

Figure 3.1: Energy spectrum for (a) ^{99m}Tc & ^{111}In and (b) ^{99m}Tc & ^{123}I respectively indicating crosstalk (spillover and downscatter) between the isotopes.

Ichihara *et al* and Hademenos *et al* [25, 26] have made use of a third energy window data multiplied by a scaling factor to estimate the downscatter for subsequent subtraction from acquired data. In a simulation study involving ^{99m}Tc/^{201}Tl Moore *et al* [38] estimated ^{99m}Tc contamination in the 70 keV window for ^{201}Tl using a third window at 100 keV. The contamination was scaled down using an appropriate scaling factor and blurred with a Gaussian function in order to match the 70 keV photons distribution from ^{99m}Tc. The 140 keV image was also scaled and blurred with Gaussian function to correct for lead x-rays from collimator. Knesaurek *et al* [39] compared the correction method proposed by Moore *et al* with their previously developed transformation crosstalk technique. In this method, a crosstalk contribution estimated using a third window transformed into energy windows for isotopes involved in imaging using predetermined transformation factors. The transformation factors were determined using applicable point spread function (PSF) for both the isotopes using different energy windows in water. Links *et al* [40] made use of a vector Wiener filter in order to improve contrast, reduce noise and reduce or eliminate crosstalk contribution between the isotopes involved in simultaneous dual isotope imaging. Tsuji *et al* [41] acquired planar images of ^{201}Tl or ^{123}I line source placed within a water tank. They used crosstalk ratios and crosstalk images obtained from line sources in order to design a low pass filter to correct for crosstalk in simultaneous dual isotope projection data. A spectral deconvolution method called photon energy recovery was developed by Hannequin *et al* [42] for the case of dual isotope acquisition using three energy windows for ^{99m}Tc/^{201}Tl. The photon energy recovery is based on the principle for single energy such that the spectrum at each pixel is a linear combination of primary and scattered photons. They used different ROIs in order to calculate crosstalk ratios using a dual window acquisition. Based on crosstalk images and ratios a blurring filter was designed for crosstalk compensation. It should be noted that most subtraction or restoration methods are intended to reduce the effect of crosstalk rather than perfect compensation.

The subtraction (restoration) based methods also have disadvantages such as requirement to determine of scaling factors (blurring function) for each imaging situation. In the absence of this, the resulting crosstalk estimate may not be accurate in all cases.

Eric Frey's group at Johns Hopkins Institute USA have developed number of model based crosstalk compensation methods in dual isotope SPECT [43, 44, 45]. X. Song *et al* [46] has developed and evaluated a model based crosstalk compensation method in simultaneous ^{99m}Tc/ ^{201}Tl myocardial SPECT, previously developed by their group. In this study they showed that this model yielded good estimates of crosstalk and Pb x-ray produced in the collimator. More recent approaches used for crosstalk compensation in simultaneous dual-isotope SPECT, involved the use of artificial neural networks [47, 48] and independent component analysis [49, 50]. These techniques are very good at compensating for crosstalk, however the major limitation in these methods is the large number of energy windows required. Jingming Bai *et al* [51] recently used three energy window data as an input for artificial neural networks in simultaneous ^{99m}Tc/^{123}I myocardial and brain SPECT and was able to obtain images comparable to those of single isotope scans. Shcherbinin *et al* [52] has recently proposed an analytical photon distribution (APD) algorithm, which analytically computes correction and includes Compton scatter of order up to 2 and first order Rayleigh scatter. Reconstructed images showed significant improvement but corrections were insufficient. de Jong *et al* [53] used Monte Carlo based down scatter correction in simultaneous ^{99m}Tc/ ^{201}Tl dual isotope SPECT. According to the authors, the correction for downscatter can be achieved by first reconstructing ^{99m}Tc and then simulating ^{99m}Tc downscatter window in ^{201}Tl window and using that to correct ^{201}Tl image during reconstruction of ^{201}Tl.

The current study focuses on a Monte Carlo (MC) based method of crosstalk compensation between two isotopes in dual isotope SPECT imaging and applied to simultaneous SPECT cancer imaging using ^{99m}Tc & ^{111}In and breast tomoscintigraphy using ^{99m}Tc & ^{123}I. MC based scatter compensation is thought to offer the most realistic crosstalk and scatter compensation modelling. Now the question is, why MC is not used more frequently in practical scenario. Before answering this question let us briefly discuss what Monte Carlo is and how it works.

3.1.3 Monte Carlo (MC) in nuclear medicine

MC is a statistical technique based on probability density functions (PDFs) uses random numbers to perform simulation of nuclear medicine imaging. MC provides a way to simulate the emitted photon trajectories through an object based on photon interactions, such as scattering and absorption. In MC, photon transport is described as a set of probability distributions involving step size of photon movement, type of interaction and updated trajectory in the case of photon scatter. The probabilities and cross-sections related to physical processes involved in photon transport are so accurately formulated that MC simulations can easily used to get realistic results in a photon transport experiment.

MC is a very important tool in studying the effects of different detector parameters and components of a nuclear medicine imaging system on image quality (e.g phantom size, collimator hole shape, crystal size etc.). MC is helpful in testing novel systems and individual component characteristics without building a system. In situations where experiments may not be performed due to economic or safety considerations MC simulation is useful in modelling and studying arbitrary geometries and situations. Therefore we can say that MC offers endless opportunities in terms of simulating any kind of nuclear medicine imaging system without any need of practically building that system.

Now after a brief introduction to Monte Carlo technique let us address the question of the use of MC in clinical time frames. In typical implementations, the inherent long calculation times (often several hours or days) associated with this technique makes it unsuitable for clinical applications. This is because a large number (tens of millions and trillions) of photon histories are needed to make the MC simulation result statistically significant. However, in SPECT simulation MC has a very low detection efficiency and only about 1 in 10,000 of emitted photons is detected [61]. Therefore in order to make MC methods clinically implementable in nuclear medicine its speed has to increase. The so called variance reduction techniques used for this purpose will be discussed in the next chapter

3.2 Conclusion

In order to make reconstruction of simultaneously acquired dual-isotope SPECT data possible, an accurate method for compensation of crosstalk (i.e. downscatter) between the isotopes is required. Different methods of crosstalk compensation have been proposed by many researchers but the MC methods may hold the greatest precision of modelling the crosstalk accurately. However in order to make the MC implementable in clinical time frames variance reduction techniques have to be used.

Chapter 4

Materials and Methods

The main objective of this work is to focus on a method of crosstalk compensation between two isotopes in dual isotope SPECT imaging and applied to simultaneous SPECT, such applications include cancer imaging using ^{99m}Tc & ^{111}In and tomoscintimammography using ^{99m}Tc & ^{123}I. Monte Carlo (MC) based scatter compensation is thought to offer the most realistic crosstalk and scatter compensation modelling. In order to understand fully let us discuss MC in simulating a SPECT study in some details.

4.1 Monte Carlo (MC) in SPECT

MC is a numerical technique that uses random numbers to solve statistical problems. In nuclear medicine MC is an important tool for research. In MC simulations the information such as photon path length, type of particle interaction and detector response are expressed in terms of probability density functions (PDFs). A PDF of random variable x usually satisfy conditions given in (4.1).

$$\begin{aligned} &\text{i)} \quad 0 \leq PDF(x) \leq 1 \\ &\text{ii)} \quad \textstyle\int_{-\infty}^{\infty} PDF(x)\, dx = 1 \end{aligned} \tag{4.1}$$

Using PDFs a random variable can be sampled and can be used in simulation.

There are a number of MC codes available that can be used in nuclear medicine. These fall into two main categories of MC codes:

1. **General purpose MC codes** with nuclear medicine applications (e.g Monte Carlo nuclear particle transport (MCNP), geometry and tracking (GEANT), electron gamma shower (EGS), electron transport (ETRAN), integrated tiger series (ITS).)

2. **MC codes specific to nuclear medicine** applications.

    (a) **MC codes for SPECT only** (e.g. SIMIND, simulation system for SPECT (SIMSPECT).)

    (b) **MC codes for PET only** (e.g. simulation system for PET (SIMPET).)

    (c) **MC codes for both PET and SPECT** (e.g. simulation system for emission tomography (SIMSET) and general architecture for text engineering (GATE).)

We will focus on SIMIND MC program only as it has been used in this thesis work [54]. The SIMIND MC program was selected for this work as we needed a standard, simple easy and fast MC based forward projector to be used in SPECT studies. The code has been written in FORTRAN and can easily simulate different detection system and geometries. The code requires that an activity source and density map be specified in simple binary formats. It can easily run on different operating systems and is compatible with various programming tools such as MATLAB. It is convenient to use standard digital as well as pixelated phantoms in SIMIND. SIMIND output includes projection data, energy spectra and scattered photon fraction. The basic structure of a MC simulator used in nuclear medicine imaging specifically SIMIND is discussed in the following paragraphs.

4.1.1 Random number generator

A random number generator is a fundamental part of any MC based simulation as a large number of random number sampling is required during the simulation. Practically the generation of true random numbers is not possible as true Random number imply numbers which cannot be calculated. However a computer algorithm may be used to generate random numbers through a random number generator. One of the simpler example of pseudo-random number generator is called as linear congruential generator (LCG). LCG can generate a sequence of random numbers N_1, N_2........ each between 0 and $k-1$ by the recurrence relation 4.2 [55].

$$N_{i+1} = (a(N_i) + b)mod(k) \tag{4.2}$$

where k is called modulus, a & b are called as multiplier and increment respectively. In order to keep generated random numbers as uniform deviates between 0 and 1, each number has to be normalized by k. It should be noted that the same initial (the seed) value in the sequence will produce same sequence of random numbers. Therefore in order to compare two simulations it is important to change this initial value. However, it can be helpful to take same sequence of random numbers for debugging purposes. Even though LCG is fast and needs only a few operation per call, the numbers generated may not be perfectly independent of each other. There are some other random number generators which can be seen in reference [55].

4.1.2 Data Sampling

In all MC calculations, a stochastic or random variable is sampled from PDF with the help of uniformly distributed random numbers. Therefore after the random number generator the next in line in a standard MC code for SPECT is the modelling of PDFs involved in a SPECT simulation and use of random number generator to sample random variable from the PDFs. It should be noted that in a photon transport experiment all the processes involved which include the distance travelled by photon before interaction, type of photon interaction (scattering or absorption) and detector and collimator response are random in nature. This means that even if the initial condition (or starting point) is known, there are many possibilities each of the process might go to, but some paths may be more probable and others less so. It is a well known fact that the physics of all the random or stochastic processes, including probability density functions involved in photon transport experiment is well established. A MC based SPECT simulation includes initiation of photon history, cross-section generation, photon path length, type of interaction sampling which will be discussed in the following paragraphs.

Photon Path Length

After initiation of photon history, photon travels a certain distance before interacting with the material. The distance travelled by a photon of given energy in the material depends on the attenuation coefficient of the material. The attenuation coefficient in turn depends upon the photon energy and density of material. The photon path length in the material varies directly with photon energy and varies inversely with the density of material but will not be unique for all the photons of given energy. The path length, l (cm) can be sampled using the PDF given in Equation 4.3 [56].

$$p(l) = \mu e^{-\mu l} \tag{4.3}$$

where μ (cm^{-1}) is the linear attenuation coefficient in the material. The probability that a photon will travel a distance x in given medium can be obtained using the probability distribution function in Equation 4.4.

$$P(l = x) = \int_0^x \mu e^{-\mu l}\, dl = 1 - e^{-\mu x} \tag{4.4}$$

Using Equation 4.4 the travelled path length, x can be sampled using a random number N as given in Equation 4.5.

$$x = -\frac{1}{\mu} ln(1 - N) \tag{4.5}$$

Since $0 \leq N \leq 1$, so as $1 - N$, therefore we can write 4.5 as 4.6.

$$x = -\frac{1}{\mu} ln(N) \tag{4.6}$$

Type of Photon Interaction

At higher energies a photon may undergo scattering (coherent or incoherent), absorption or pair production(only for isotopes with photon energy greater than 1.022 MeV). The finite probability associated with each of the interactions is known as the cross-section. The sum of individual cross-sections for each of the mentioned interaction types gives rise to the overall attenuation coefficient as given in Equation 4.7.

$$\mu = \tau + \sigma_r + \sigma_c + \kappa \tag{4.7}$$

where, τ, σ_r, σ_c and κ represent photoelectric, Rayleigh (coherent) scattering, Compton (incoherent) scattering and pair production cross-section respectively.

It should be noted that pair production occurs at photon energies higher than 1.022 MeV, whereas Rayleigh scattering is important at photon energies $\leq$ 50 keV. In the usual nuclear medicine energy range (100-511 keV) pair production is impossible to occur and Rayleigh scattering is highly unlikely to occur within this energy range. For example at peak energy of 140 keV the probability of Rayleigh scattering in the human body and crystal material is less than 1% [57]. Therefore in practice MC based SPECT simulation Compton Scattering and photoelectric effect are considered as the most likely mode of photon interactions. Therefore a random number, N can be sampled using Equation 4.8 under the assumption that at usual nuclear medicine energies Compton scattering and photoelectric effect are the dominant interaction types.

$$\begin{array}{ll} \text{Photoelectric effect} & N \leq \frac{\tau}{\mu} \\ \text{Compton Scattering} & \frac{\tau}{\mu} < N \leq \frac{(\tau+\sigma_c)}{\mu} \end{array} \tag{4.8}$$

where, $\frac{(\tau+\sigma_c)}{\mu}$ will be approximately equal to 1. Now we can see that the Compton scattering cross section, σ_c needs to be sampled which results in photoelectric effect cross section (τ) equal to $1 - \sigma_c$. In MC modelling, the cross section of each individual photon interaction and the attenuation coefficient calculated using a specific computer program called XCOM [58]. XCOM generates cross section tables related to material composition, photon scattering and photon energies. These generated tables are then utilized in simulation at each photon travelling step in order to calculate the photon weight at each step. In the case of photon scattering, after the path length calculation, the photon direction is updated. Compton scattering cross section under the assumption of unbounded electron is calculated using Klein Nishina (KN) Equation 4.9.

$$d\sigma_{KN} = \frac{r_e^2}{2}\left(\frac{E^{'}}{E_o}\right)^2\left(\frac{E_o}{E^{'}} + \frac{E^{'}}{E_o} - \sin^2\theta\right)d\Omega \tag{4.9}$$

where, $d\sigma_{KN}$ is the differential cross section to be sampled, r_e is the classical electron radius, E_o is the initial photon energy, $E^{'}$ is the scattered photon energy calculated using Equation 4.10 and θ is the scattering angle.

$$E^{'} = \frac{E_o}{1 + \frac{E_o}{m_oc^2}(1 - \cos\theta)} \tag{4.10}$$

where, m_oc^2 is the electron rest mass energy. With electron in bound state KN need be modified by incoherent scattering factor in order to include atomic effects as given in Equation 4.11 [56].

$$d\sigma_c = d\sigma_{KN}S(m_t, Z) \tag{4.11}$$

where, $d\sigma_c$ Compton scattering cross section, $S(m_t, Z)$ incoherent scattering factor,

Z is atomic number and m_t is momentum transfer parameter given as:

$$m_t = \frac{E_o}{2hc} \sin\left(\frac{\theta}{2}\right) \tag{4.12}$$

Kahn introduced scatter angle sampling method [59] described below:

1. A scattering angle was sampled from normalized distribution in Equation 4.9.
2. A momentum transfer parameter, m_t is then calculated on the basis of sampled value of θ.
3. The θ obtained from sampled m_t in form of a random number, N is only accepted if $N < (S(m_t, Z)/S_{max}(m_t, Z))$

After sampling of new direction and path length, Cartesian coordinates for new photon interaction point needs to be calculated. Let θ_1 & ϕ_1 be the initial and θ_2 & ϕ_2 the final polar and azimuthal angles for the photon respectively. Hence in this case final direction cosines ($u^{'}$, $v^{'}$, $w^{'}$) can be calculated from initial direction cosines (u, v, w) as given in 4.13.

$$\begin{aligned}
u^{'} &= u\cos\theta_2 + \sin\theta_2(w\cos\phi_2\cos\phi_1 - \sin\phi_2\sin\phi_1) \\
v^{'} &= v\cos\theta_2 + \sin\theta_2(w\cos\phi_2\sin\phi_1 - \sin\phi_2\cos\phi_1) \\
w^{'} &= w\cos\theta_2 - \sin\theta_2\sin\theta_1\cos\phi_2 \\
u &= \sin\phi_2\sin\theta_1 \\
v &= \sin\theta_1\cos\phi_1 \\
w &= \cos\theta_1
\end{aligned} \tag{4.13}$$

The updated Cartesian coordinates ($x^{'}$, $y^{'}$, $z^{'}$) are then calculated by the direction cosines at path length d as per Equation 4.14.

$$\begin{aligned} x^{'} &= x + du^{'} \\ y^{'} &= y + dv^{'} \\ z^{'} &= z + dw^{'} \end{aligned} \tag{4.14}$$

Even though Rayleigh scattering is not negligible at photon energies less than 100 keV, the exact calculation, modelling and sampling of Rayleigh scattering is complicated and will not discuss here. Details can be found in [56].

4.1.3 Detection System Simulation

The hardware of detector system includes the collimator, crystal and other electric components. Therefore, the simulation of the effect of all the components require proper modelling of the effects. The effect of a typical detector system includes crystal, light guide, photo cathodes, photomultiplier tubes (PMTs) and other electronic components, are modelled in terms of energy resolution.

Energy Resolution Simulation

The ability of the detection system to distinguish two photon energies is called energy resolution. When two energies are separated by less than the Full Width Half Maximum (FWHM), the system might not be able to distinguish them as independent events. Once the photon hits the detector following factors effect the energy resolution.

1. **Type of crystal material** which effects amount of light emitted.
2. **The effect of light guide** and amount of light collected by PMTs.

3. **The efficiency of the photo cathodes** in the PMTs in converting the light into photoelectrons.

4. **Electron collection efficiency** of PMT anode.

5. The electronics associated with signal processing.

Collimator Simulation

The component of the detection system which is between the crystal and the incoming photon is the collimator. The collimator allows only those incoming photons to reach the crystal which are exactly aligned with the collimator hole direction. However, there is a chance that the photon may undergo penetration through the septa or may get scattered within the collimator and get detected. The photons passing through the holes of the collimator gives rise to geometric response of the collimator and is modelled as a Gaussian function. In SPECT imaging, the overall detector resolution is a combination of the detector intrinsic resolution, R_i and collimator geometric resolution, R_c. The intrinsic resolution refers to the ability of detector and associated electronics to resolve the event location precisely. The overall detection system resolution can be described in terms of the full width at half maximum as given in Equation 4.15 [3].

$$FWHM = \sqrt{R_i^2 + R_c^2} \tag{4.15}$$

where, R_c in case of parallel hole collimator can be determined using the empirical relation 4.16.

$$R_c \approx h\left(\frac{l_e + d}{l_e}\right) \tag{4.16}$$

where, h is the collimator hole size, l_e is the effective collimator thickness ($l_e = 1 - 2\mu^{-1}$, where μ is the linear attenuation coefficient) accounts for septal penetration up to some extent and d denotes the source to collimator distance. However, collimator scatter or septal penetration is more difficult to describe mathematically and has to be modelled externally based on photon energies and source-detector distance. Ljunberg *et al* [60] has described a delta ray tracing method to model the effect of septal penetration and collimator scatter in SIMIND MC code. The method is based on the path length sampling using the method similar to the one mentioned in Section 4.1.2. In this method collimator was considered as a heterogeneous medium consisting of collimator holes with air and lead septa. The different steps involved in this method are described as follows:

1. The first path length in collimator is sampled using Equation 4.6.
2. After path length sampling the ratio of attenuation coefficient with lead attenuation coefficient is taken which can only be either 0 in case of air or 1 in case the path length ends in lead. Ljunberg *et al* described criteria to decide weather the photon path ended either within collimator hole or in lead. The criteria was based on determination of photon entrance point into hexagonal holes in a parallel hole collimator. In order to determine if the photon entered into the hole in region with air or lead, different hole parameters can bed used.
3. If the photon ends up in the lead the type of interaction is sampled. In this case the scattering path length is sampled at each new step.
4. The entrance point at the lower collimator surface is recorded. If the exit point of the photon lies in the same hole the event will be recorded as geometric

response. In case there are multiple scatterings within the hole with exit point in the same hole the event will be considered as a scattered event, otherwise the photon will be treated as a penetrated photon.

4.2 Variance Reduction Techniques in MC

Accurate modelling of the physical processes involved in SPECT has made MC, a popular simulation tool. However, in typical implementations, the inherent long calculation times (often several hours or days) associated with this technique makes it unsuitable for clinical applications. The reason for this is the low detection sensitivity of SPECT. For example consider a 1 minute planar acquisition in which 20 mCi of activity is administered to the patient to give 400,000 counts. In this time (20×10^{-3} Ci $\times$ 60 sec $\times 3.7 \times 10^{10}$ disintegrations/sec/Ci =) 4.4×10^{10} disintegrations took place within the patient body and only 4×10^5 are detected, which means $111,000$ events has given rise to one detected event. This makes MC simulation in nuclear medicine a very inefficient technique. This means that the number of detected photons would be very small compared to actual number of photon emissions and hence the variance is large. The methods used to increase the ratio of detected events to the actual photon emission are known as *variance reduction techniques (VRTs).* In variance reduction techniques a weight based method is used. In order to increase the number of detected photons compared to total number of photons histories generated a weight must be attached to each photon history that is generated by MC simulation code.

One of the techniques to improve MC efficiency is known as forced detection (FD) [61]. In this method the angular or spatial distribution function is modified in order to force as many photons as possible to hit the detector. In this method the ratio of detected photons to the total number of photon histories generated is increased by generating a copy of photon at each interaction site towards the collimator by modifying the photon weight. A suitable photon distribution within maximum polar angle, θ_{max} can be obtained using Equation 4.17.

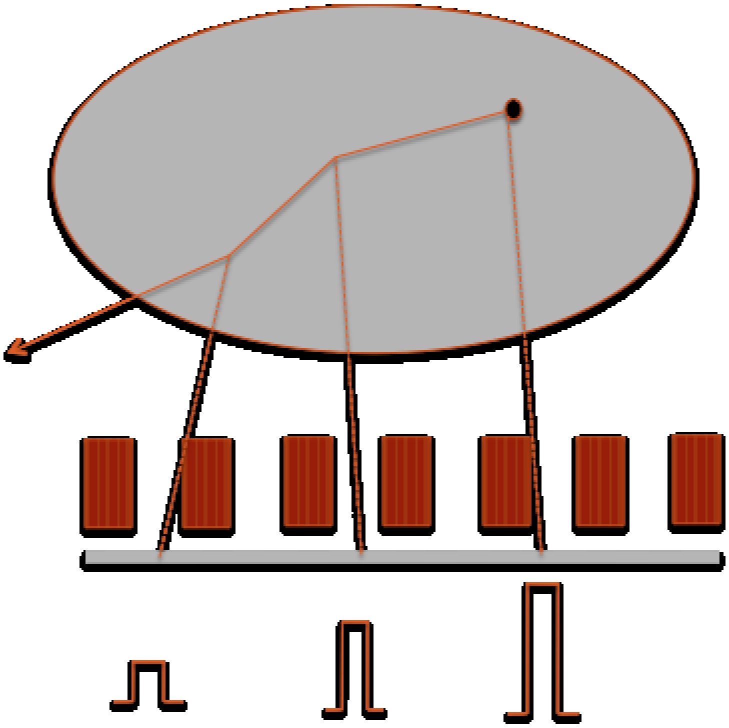

Figure 4.1: Schematic of FD. The solid lines are the scattered photon paths, and the dashed lines are the copies of scattered photons forced to the detector after photon weight modification.

$$\begin{aligned}\theta &= \cos^{-1}\left(1 - N[1-\cos\theta_{max}]\right)\\ \phi &= 2N\pi\end{aligned} \tag{4.17}$$

where, N is a random number and ϕ is a uniformly distributed azimuthal angle. Similarly, the photons can also be forced towards the detector by changing the photon path length to less than or equal to maximum path length d_{max}, as given in Equation 4.18

$$d = -\frac{1}{\mu} ln \left(1 - N\left(1 - e^{-\mu d_{max}}\right)\right) \tag{4.18}$$

Since the angular or spatial probability distribution has been modified, the photon weights has to be modified accordingly, as given in Equation 4.19.

$$w_i = w_{i-1}\left(1 - e^{-\mu d_{max}}\right) \tag{4.19}$$

In addition to weight modification using Equation 4.19, the weight has to be modified using Klein-Nishina cross-section in the forced direction.

4.2.1 Convolution based Forced Detection (CFD) used to Accelerate Monte Carlo

Our lab has previously developed and incorporated a number of different variance reduction techniques (VRT) that have made Monte Carlo-based crosstalk compensation feasible to use in clinical time frames [62].

The convolution based forced detection(CFD) is very similar to FD. The CFD is different from FD only in two aspects. i). the convolution of detection probability with distance dependant collimator response function (Gaussian) and ii). forcing the photons along the paths perpendicular to the collimator in CFD compare to FD as shown in Figure 4.2. It has been shown that the detector response (represented as the distance dependant point spread function, PSF) of collimator can be modelled

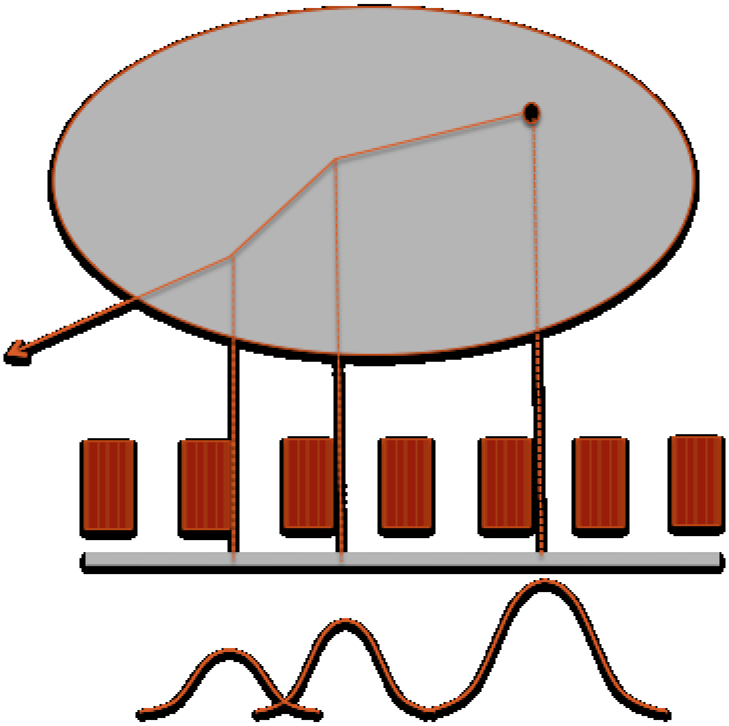

Figure 4.2: Schematic of CFD. The solid lines are the scattered photon paths, and the dashed lines are the copies of scattered photons forced to the detector after photon weight modification.

as a Gaussian as shown in Equation 4.20.

$$PSF(x,y)\mid_{d}=\frac{1}{2\sigma_x\sigma_y}.e^{-\frac{1}{2}\left(\frac{x-x_o}{\sigma_x}\right)^2-\left(\frac{y-y_o}{\sigma_y}\right)^2} \tag{4.20}$$

where(x_o, y_o) is the center pixel where photons are detected on the collimator face and σ_x and σ_y are derived using Equation 4.15 for collimator. As discussed in Section 4.1.2 Compton scattering and photoelectric effect are the main mode of photon interaction in SPECT. In this case the sum of probabilities for Compton scattering and photoelectric effect can be considered as 1 and probability of Compton scattering can be determined approximately as $(1-P_{photo}(E))$, where $P_{photo}(E)$ is probability of photon of energy E to undergo photoelectric effect. The probability of photon detected by a detector at an angle, α using CFD can be evaluated using Equation 4.21 [62].

$$P(\alpha) = w_i \times (1 - P_{photo}(E)) \times d\sigma_{KN}(\phi) \times e^{-\int_0^{l_{fd}} \mu(E)\, dl} \tag{4.21}$$

where,

w_i = Photon history weight initially set at 1.

$1 - P_{photo}(E)$ = Probability that photon is not absorbed by photoelectric effect (approximately equal to probability of Compton scattering).

$d\sigma_{KN}(\phi)$ = Klein-Nishina cross-section for a photon to scatter at an angle ϕ.

$e^{-\int_0^{l_{fd}} \mu(E)\, dl}$ = Photon attenuation factor due to forced path length of l_{fd}.

In this work accelerated SPECT Monte Carlo simulation using convolution based force detection (CFD), is being used to accelerate the Monte Carlo photon transport modelling in SIMIND MC program. Figure 4.3 shows the flow chart diagram of SIMIND MC program with CFD implemented to accelerate the code.

4.3 Phantoms used in This Work

Phantoms can either be realistic or mathematical description of physical activity distributions and attenuation materials. The accuracy and compatibility of MC acceleration using convolution based forced detection (CFD) was evaluated using a point source data for ^{111}In/^{99m}Tc. There are two sets of dual isotope data namely, ^{111}In/^{99m}Tc (cancer imaging) and ^{123}I/^{99m}Tc (tomoscintimammography), were used in this work. In the case of ^{111}In/^{99m}Tc experimental verification of proposed MC based reconstruction was performed using the IEC PET body phantom set by Data

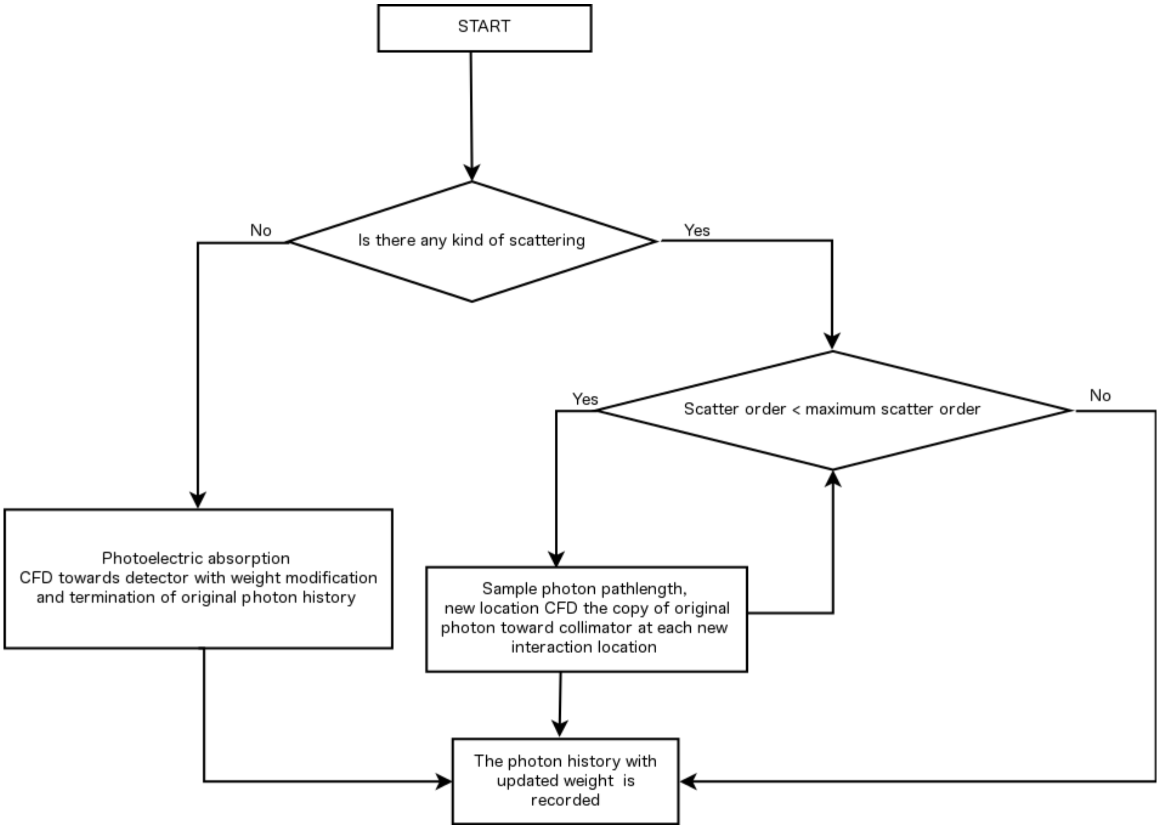

Figure 4.3: Flow chart of SIMIND with CFD incorporated.

Spectrum Inc. USA. Only simulation exercises and data reconstruction has been performed in the case of ^{123}I/^{99m}Tc SPECT. The list of phantoms used in this work is as follows:

- Point source
- NEMA IEC^{TM} body phantom set
- Sources in a cylinder
- NURBS based Cardiac Torso (NCAT) Phantom
- Breast phantom

4.3.1 Point Source

A point source is one of the standard phantom geometries used in nuclear medicine imaging. It is generally used to verify the accuracy of the simulated detector system. A point source projection appears as a two dimensional (2D) Gaussian shape representing the collimator-detector response.

The spatial resolution was evaluated in terms of full width at half maximum (FWHM). FWHM is calculated using Equation 4.22 from the standard deviation, σ of a fitted Gaussian function to the profiles in both horizontal and vertical dimensions.

$$FWHM = 2\sigma\sqrt{2ln2} \tag{4.22}$$

The sensitivity was evaluated in terms of counts per seconds (CPS). The accuracy and compatibility of MC acceleration using convolution based forced detection (CFD) was evaluated using point source data for ^{111}In/^{99m}Tc in terms of spatial resolution and sensitivity.

The gamma camera used for experimental data acquisition was a GE Infinia gamma camera (General Electric Company, USA).

4.3.2 NEMA IEC Body Phantom Set^{TM}

In order to evaluate performance of the MC based reconstruction, phantom simulations and experimental studies using NEMA IEC body phantom set (shown in Figure 4.4) was performed in case of ^{99m}Tc/^{111}In simultaneous SPECT acquisition. In order to acquire dual-isotope projection data using ^{99m}Tc and ^{111}In for simulation study activity was deposited in the centeral spheres of the phantom and the body of the phantom filled with non radioactive water. Three of the spheres (diameter (ϕ) = 13, 22 and 37 mm respectively) were filled uniformly with 7.75 MBq of ^{99m}Tc and an activity of 17.25 MBq of ^{111}In, was deposited uniformly in the remaining three spheres (ϕ = 10, 17 and 28 mm respectively). The activity values were calculated to provide an activity concentration ratio of 1:5 between ^{99m}Tc and ^{111}In respectively.

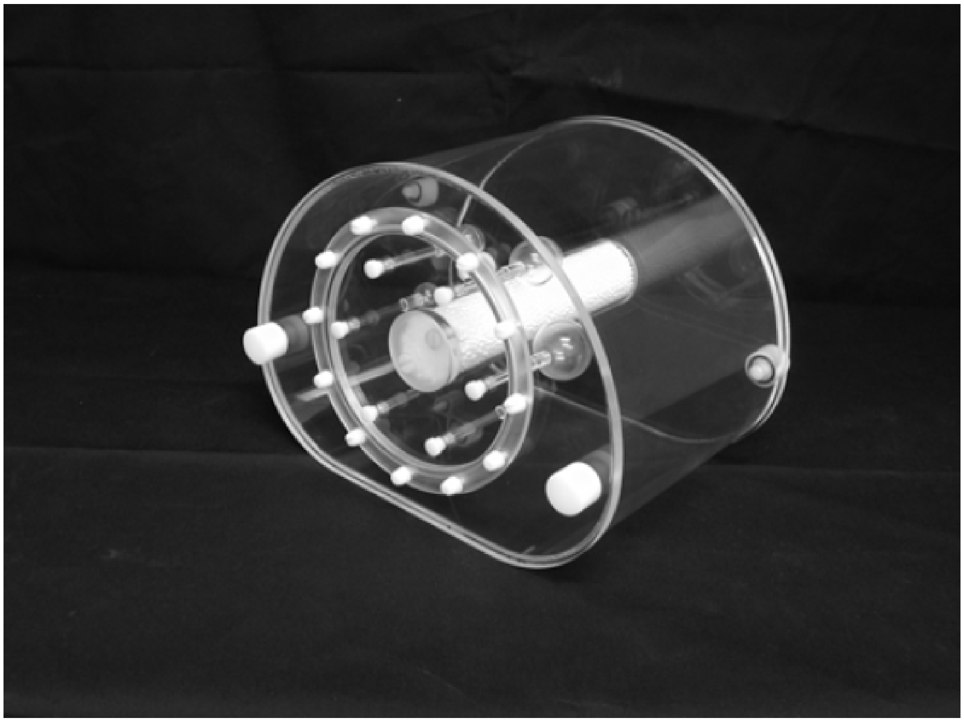

Figure 4.4: NEMA IEC body phantom set^{TM} by Data Spectrum Corporation, USA.

4.3.3 Sources in a Cylinder

In order to acquire dual-isotope projection data using ^{99m}Tc and ^{123}I a pixelated phantom consisted of a non radioactive water filled cylinder (ϕ =56 cm) having six spheres of varying radius in the center as shown in Figure 4.5. Three of the spheres (ϕ = 11, 7 and 4 cm respectively, shown in blue in Figure 4.5) were filled uniformly with ^{99m}Tc while ^{123}I, was deposited uniformly in the remaining three spheres ($\phi =$ 9, 5 and 2 cm respectively, shown in gray in Figure 4.5).

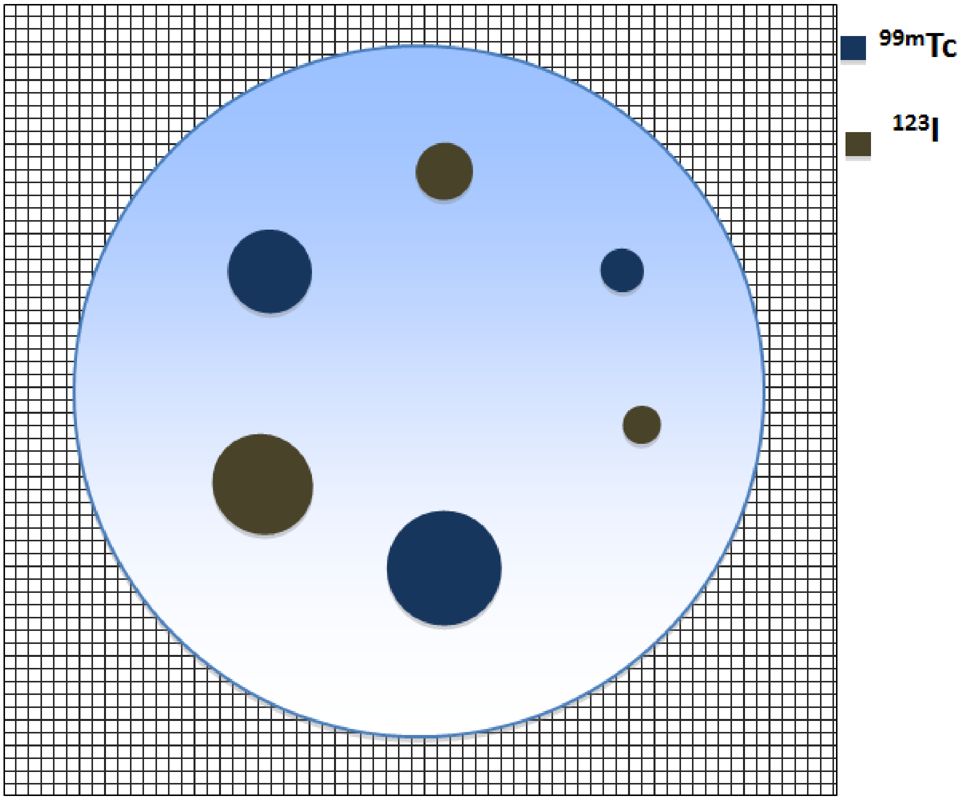

Figure 4.5: Cross sectional view of a cylindrical phantom with six spheres of varying radius in a 128 × 128 × 128 grid.

4.3.4 NURBS based Cardiac Torso (NCAT) Phantom

This phantom was designed in order to accurately model anatomical variations in organ shapes and physiological motion. A 4D computer graphic technique known as non-uniform rational B-splines (NURBS) was used to design a NURBS based cardiac torso (NCAT) phantom [63]. In the NCAT phantom, human CT datasets were used as basis for generated surfaces. It also contains beating heart and respiratory motion modelling. Reconstructed images obtained through gated magnetic resonance imaging (MRI) were used to model the beating heart whereas respiratory motion was modelled with the help of realistic respiratory physiology. The NCAT phantom data can be used to simulate realistic bone scan studies, cardiac imaging or organ studies such as, liver, lungs or kidney. The NCAT phantom allows flexibility in terms of specifying various geometric properties such as height, body size etc. and relative concentration of activity within different organs. In this work we have used NCAT phantom to simulate a tumour in the axillary region within non uniform attenuation map (bones) for ^{123}I/^{99m}Tc. The simulation was performed in order to test the accuracy of proposed reconstruction method.

4.3.5 Breast Phantom

In order to simulate dual-isotope imaging for breast cancer, a mathematical breast phantom was developed. Three different breast sizes, small, medium and large, were modelled. The breast soft tissue was modelled as half ellipsoid with semi spherical nipple [64] as shown in Figure 4.6. Table 4.1 shows the length of semi axis and tilt introduced in the breast phantom [65]. In this case the coordinates (x, y, z) rotated at an angle θ were calculated from the standard Cartesian coordinates (x_o, y_o, z_o)

Table 4.1: Parameters used in pixelated breast modelling of different sizes

	Semi-axis length (cm)			
Breast Size	**a**	**b**	**c**	**Tilt (θ)**
Small	4.0	4.0	4.0	10^o
Medium	6.5	5.5	5.5	7.5^o
Large	8.0	7.0	7.0	5^o

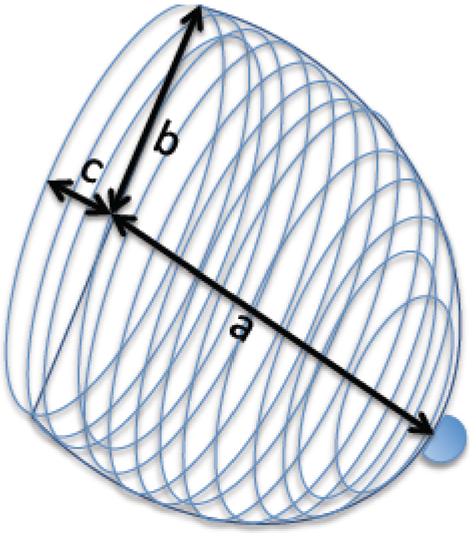

Figure 4.6: Breast shape modelling as tilted half ellipsoidal breast and semi spherical nipple

using Equation 4.23

$$\begin{aligned} x &= x_o^2 \\ y &= (y_o \cos\theta - (z_o - z_c)\sin\theta)^2 \\ z &= (-y_o \sin\theta + (z_o - z_c)\cos\theta)^2 \end{aligned} \tag{4.23}$$

In this case the center was taken at (0, 0, z_c) where z_c was taken in the middle of the imaging grid. With (x, y, z) values calculated using Equation 4.23 half ellipsoid satisfy conditions given in inequality 4.24.

$$\frac{x^2}{a^2} + \frac{y^2}{b^2} + \frac{z^2}{c^2} \leq 1 \text{ and } z_o \geq z_c \tag{4.24}$$

For each breast size 13 spherical lesions of different sizes were randomly generated (described in Table 4.2). From the generated lesions 10 combinations with 3

Table 4.2: Radii of spherical lesions used for different breast size phantoms

	Lesion	
Breast Size	**Radius (mm)**	**Number**
Small	2.4	5
	4.0	4
	5.6	4
Medium	3.3	5
	5.5	4
	7.7	4
Large	4.2	4
	7.0	4
	9.8	3
	12.6	2

lesions per combination were selected randomly. For each of the sets three lesion were randomly selected and uniform activity of ^{99m}Tc, ^{123}I and both ^{99m}Tc & ^{123}I was deposited respectively.

4.4 Data acquisition

In dual isotope SPECT studies, projection data is acquired using MC for both the isotopes (x and y) simultaneously and can be represented by the linear Equations 4.25 and 4.26.

$$H_X(f_X + f_{Y_s}) = p_X \tag{4.25}$$

$$H_Y(f_{X_s} + f_Y) = p_Y \tag{4.26}$$

Where H_X and H_Y represent the system matrices (MC based forward projector or gamma camera) for isotope X and Y respectively applied over object f having deposition of both the isotopes to get projection matrix p_X and p_Y respectively. An additional subscript s denotes the crosstalk from one isotope detected under the window for the other isotope.

In case of simultaneous ^{111}In/^{99m}Tc SPECT studies, activity deposition scheme used for simulation study (as described in Section 4.3.2) were used for experimental data acquisition of NEMA IEC^{TM} body phantom set on GE Infinia dual head gamma camera. It should be noted the in experimental acquisition specific activity ratio ^{111}In:^{99m}Tc was taken as 1:2. However ^{99m}Tc only image was obtained before injecting ^{111}In into the spheres. Simultaneous ^{111}In/^{99m}Tc acquisition was performed after injecting ^{111}In in remaining spheres with non radioactive water background. In order to obtain SPECT projection data in ^{99m}Tc background, ^{99m}Tc was injected in non radioactive water for final simultaneous ^{111}In/^{99m}Tc data acquisition. ^{99m}Tc was deposited in background to get specific activity ratio ^{111}In:^{99m}Tc in spheres:^{99m}Tc in background as 1:20:40.

For simulation as well as for experimental acquisition of the data 120 projections with matrix size 128 × 128 were acquired. For simulation and experimental data acquisition time of 15 s/projection and 30 s/projection was used respectively. Table 4.3 shows seven energy windows used for ^{111}In and four energy windows for ^{99m}Tc in case of both simulation as well as for experimental data acquisition. The 3 keV scatter windows were acquired to perform triple energy window (TEW) based scatter correction of data [26]. Figure 4.7 shows the ^{99m}Tc and ^{111}In spectrum with windows acquired to perform pixel by pixel based correction of the data using TEW. TEW based compensation uses two narrow energy windows adjacent to each of the primary windows in order to determine crosstalk contribution within each of the full energy peaks. In order to get scatter S_i contribution in ith energy window following

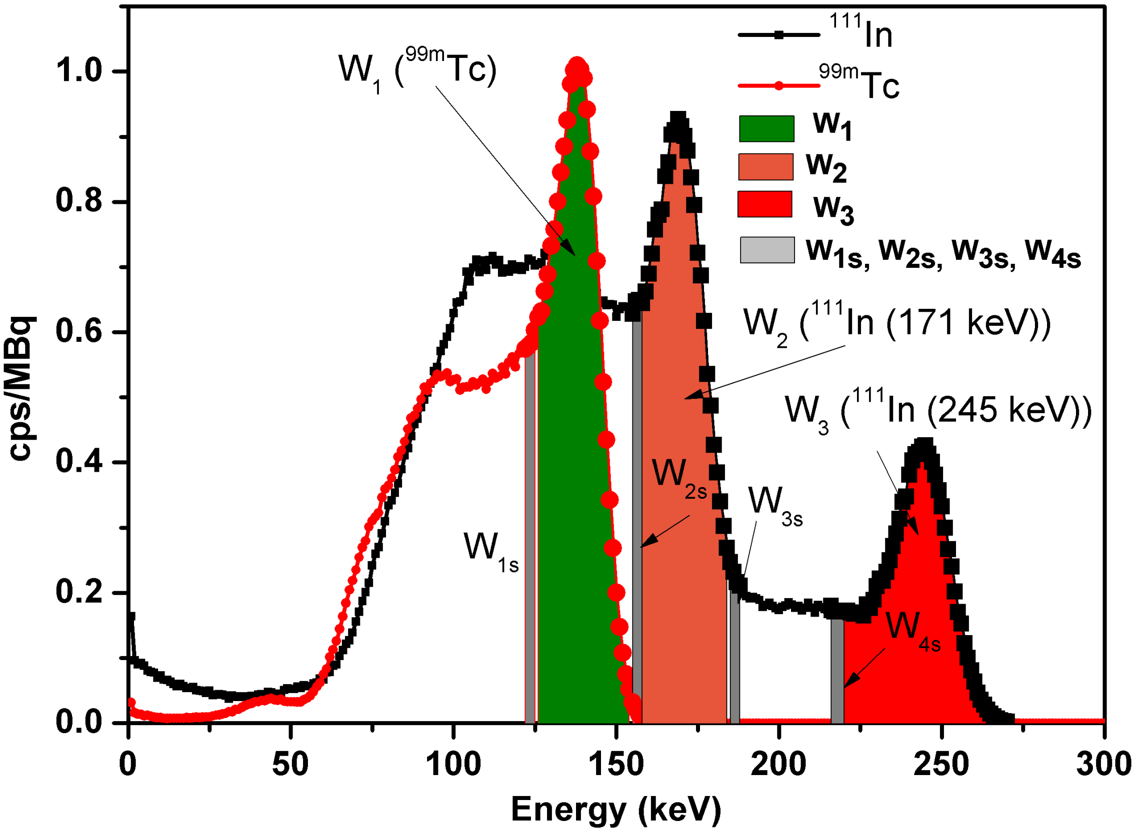

Figure 4.7: ^{99m}Tc/^{111}In spectrum with windows used for TEW based crosstalk correction of projection data.

Equation 4.27 can be used.

$$S_i = \left(\frac{C_{is,j}}{W_{is}} + \frac{C_{i+1s,j}}{W_{i+1s}}\right)\frac{W_{is}+W_{i+1s}}{2} \tag{4.27}$$

where,

W_{is} = window width for ith scatter window on the left side of photopeak

W_{i+1s} = window width for $(i+1)th$ scatter window on the right side of photopeak

$C_{is,j}$ = counts collected in jth pixel of ith scatter window, W_{is}

$C_{i+1s,j}$ = counts detected in jth pixel of $(i+1)th$ scatter window, W_{i+1s}

It should be noted that in case of 245 keV photopeak for ^{111}In $C_{5s,j} = 0$ as $W_{5s} = 0$.

Table 4.3: Energy windows used for projection data acquisition for simultaneous ^{111}In/^{99m}Tc SPECT.

^{111}In energy windows
122-125 keV, 126-154 keV,155-158 keV, 158.2-183.8 keV, 184.8-187.8 keV, 216.5-219.5 keV and 220.5-269.5 keV
^{99m}Tc energy windows
122-125 keV, 126-154 keV,155-158 keV and 158.2-183.8 keV

In case of simultaneous ^{123}I/^{99m}Tc SPECT studies with cylindrical, NCAT and breast phantom for acquisition as well as reconstruction using Sim-OSEM asymmetric (126-150 keV for ^{99m}Tc and 151-174.9 keV for ^{123}I) primary energy windows were used in order to avoid overlapping of two peaks as can be seen from the Figure 3.1(b). For all the simulation studies 120 projections with matrix size 128 × 128 were acquired. In case of breast phantom studies SPECT data acquisition 150 MBq of activity was deposited in total to give specific activity ratio between ^{99m}Tc background in breast soft tissue, ^{99m}Tc in lesions and ^{123}I as 1:5:10 respectively.

4.5 Reconstruction and Activity Estimation

We have developed an iterative MC based image reconstruction technique, simultaneous ordered subset expectation maximization (Sim-OSEM) that simulates the photon down-scatter and spillover in case of overlapping full energy peaks from one isotope into the acquisition window of a second isotope. We use a modified ordered subset-expectation algorithm to perform this step as given in 4.28 and 4.29.

$$f_X^{new} = \frac{f_X^{old}}{\sum_{a\epsilon s} H_{a,X}^T} \sum_{a\epsilon s} H_{a,X}^T \frac{p_X}{\sum_{a\epsilon s} H_{a,X}^{'}(f_X^{old} + f_{Y_s}^{old})} \tag{4.28}$$

$$f_Y^{new} = \frac{f_Y^{old}}{\sum_{a\epsilon s} H_{a,Y}^T} \sum_{a\epsilon s} H_{a,Y}^T \frac{p_Y}{\sum_{a\epsilon s} H_{a,Y}^{'}(f_Y^{old} + f_{X_s}^{old})} \tag{4.29}$$

We have used attenuation correction based analytical backprojector H^T and MC based forward projectors ($H_X^{'}$ and $H_Y^{'}$) in order to update the old estimate to get the new object estimate for a given isotope, as can be seen in equation (4.28) and (4.29).

It is important to note that activity estimation is also possible in case of Sim-OSEM based reconstruction. The result of a MC forward projector is a 2D projection image in units of cps/MBq. In order to perform activity estimation a count based comparison of the acquired data (in counts) and MC based data (in cps/MBq) was performed. This was done to perform an update of the old activity factor in MC based projection of estimate, compared to corresponding acquired projection as shown in Equation (4.30) and (4.31).

$$R_X^{new} = R_X^{old} \frac{\sum_{a\epsilon s} p_X}{\sum_{a\epsilon s} H_{a,X}^{'}(f_X^{old} + f_{Y_s}^{old}) \times t_{acq}} \tag{4.30}$$

$$R_Y^{new} = R_Y^{old} \frac{\sum_{a\epsilon s} p_Y}{\sum_{a\epsilon s} H_{a,Y}^{'}(f_Y^{old} + f_{X_s}^{old}) \times t_{acq}} \tag{4.31}$$

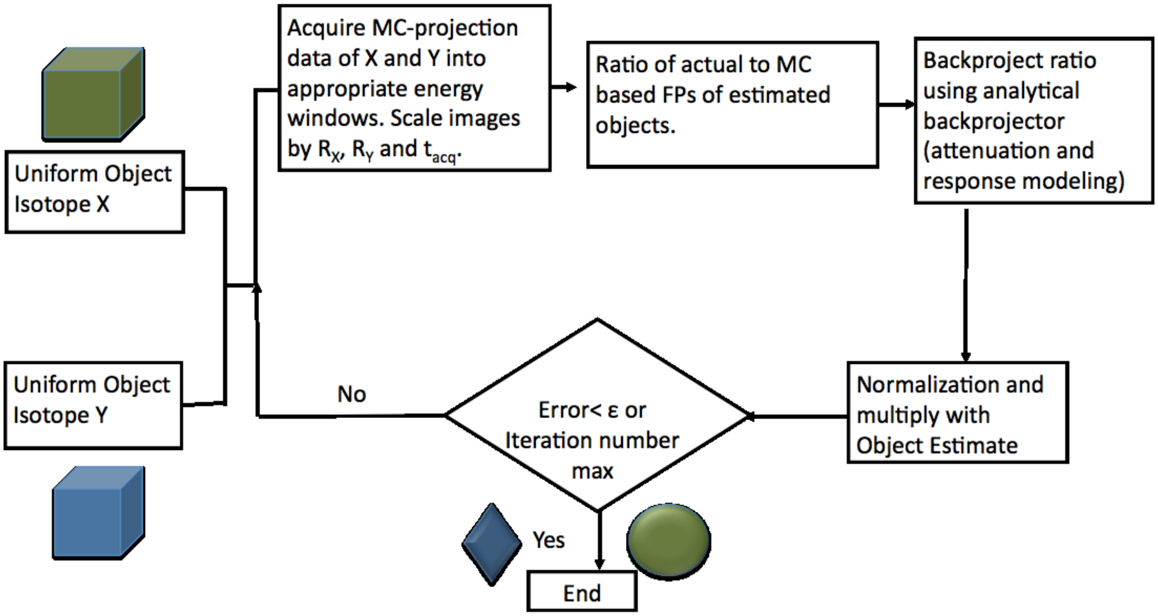

Figure 4.8: Flow chart diagram of Sim-OSEM based dual isotope image reconstruction.

Where t_{acq} is acquisition time per projection in seconds. Figure 4.8 shows the flow chart diagram of Sim-OSEM based simultaneous dual isotope reconstruction.

In case of simultaneous ^{111}In/^{99m}Tc SPECT studies Sim-OSEM based reconstructed images were compared to the images obtained using analytical attenuation based reconstruction of data uncorrected for crosstalk, data corrected using TEW compensation and single isotope data without any crosstalk contribution from other isotope. Analytical attenuation based reconstruction uses analytical projector/backprojector pair incorporated into standard OSEM reconstruction algorithm.

Sim-OSEM based reconstructed images were compared to the images obtained using analytical attenuation based reconstruction of data uncorrected for crosstalk, single isotope data without any crosstalk contribution from other isotope in case of simultaneous ^{123}I/^{99m}Tc SPECT simulation studies.

Chapter 5

Results and Discussions

The main aim of this work is to develop a reconstruction technique which accurately corrects for crosstalk between the isotopes involved in simultaneous dual isotope SPECT acquisition. We have developed a reconstruction method, which realistically corrects for crosstalk as well as scatter in simultaneous dual-isotope SPECT. Our proposed method is different from fast Monte Carlo based joint iterative reconstruction method used by Ouyang *et al* [66]. In method proposed by Ouyang *et al* scatter and crosstalk corrections applied on the images reconstructed using standard OS-EM for number of iterations without scatter correction at first, then the images reconstructed with scatter correction and finally images reconstructed jointly using joint OS-EM (JOSEM). It should also be noted that compare to crosstalk correction using artificial neural networks and independent component analysis, Sim-OSEM requires only primary energy window data for reconstruction rather than data acquired using multiple energy windows. As discussed previously in Section 4.3, this work mainly focusses on two pairs of dual isotopes which are ^{111}In/^{99m}Tc (cancer imaging) and ^{123}I/^{99m}Tc (tomoscintimammography).

5.1 ^{99m}Tc/^{111}In Simultaneous SPECT

Dual isotope ^{99m}Tc/ ^{111}In has potential application in cancer imaging using antibodies ([67] and [68]). As discussed previously simultaneous acquisition of both isotopes have advantages such as reduced patient discomfort, which results in lesser motion artefacts and if there is patient motion during the image acquisition will effect the images for both the isotopes in same way and increased hardware throughput compare to one by one acquisition.

5.1.1 Monte Carlo Evaluation

In order to use Monte Carlo for the reconstruction of experimental data in case of ^{111}In/^{99m}Tc using Sim-OSEM, compatibility of dual head gamma camera with Monte Carlo evaluated in terms of system spatial resolution and sensitivity as shown in Figure 5.1. From Table 5.1, it can be seen that experimental data correlates well with simulated data. However, reason for difference between horizontal and vertical direction in case of MC needs further investigation.

Table 5.1: r^2 values for spatial resolution in horizontal and vertical direction in air.

	r^2 **value**	
Isotope	**Horizontal Head 1, Head 2**	**Vertical Head 1, Head 2**
^{111}In (171 keV)	0.9996, 0.9998	0.9997, 0.9999
^{111}In (245 keV)	0.9999, 0.9991	0.9995, 0.9994
^{99m}Tc (140 keV)	0.9994, 0.9995	0.9995, 0.9994

Table 5.2 shows sensitivity values for ^{111}In and ^{99m}Tc energies respectively at source to collimator distance of 10 cm. Difference between experimental and simulated

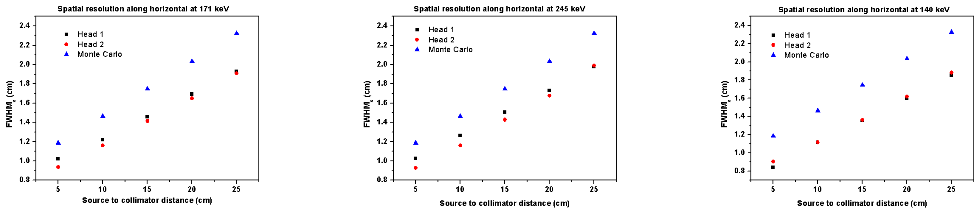

(a) Horizontal ^{111}In (171 keV) (b) Horizontal ^{111}In (245 keV) (c) Horizontal ^{99m}Tc

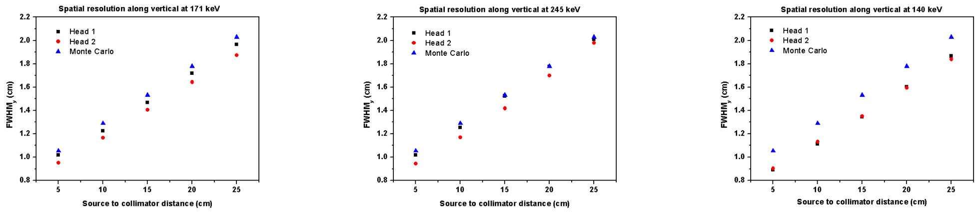

(d) Vertical ^{111}In (171 keV) (e) Vertical ^{111}In (245 keV) (f) Vertical ^{99m}Tc

Figure 5.1: Full width half maximum(FWHM) in horizontal direction for (a) 171 keV (b) 245 keV (c) 140 keV and in vertical direction for (d) 171 keV (e) 245 keV (f) 140 keV respectively.

sensitivity values in case of ^{111}In can be seen in Table 5.2, may be due to absence of septal penetration correction in case of simulated sensitivity values. The septal penetration is not an issue in case of ^{99m}Tc with MEGP collimator as can be seen from the Table 5.2.This may be one of the reasons for errors in estimated activity values discussed in Section 5.1.4.

5.1.2 Simulation Results

From Figure 5.2, it can be seen that image reconstruction using conventional OSEM algorithm with no crosstalk compensation shows significant crosstalk compared to TEW and Sim-OSEM based dual isotope reconstruction. The proposed Sim-OSEM based dual isotope reconstruction produces the least crosstalk contamination and is able to reduce the background contamination significantly. The images reconstructed

Table 5.2: Sensitivity values for medium energy general purpose (MEGP) collimators at source to collimator distance of 10 cm.

	Sensitivity (cps/MBq)		
Isotope	**Head 1**	**Head 2**	**MC**
^{111}In (171 keV)	69.5	68.5	63.4
^{111}In (245 keV)	45.9	45.5	40.3
^{99m}Tc (140 keV)	75.0	72.8	83.9

using Sim-OSEM has shown not only very good crosstalk compensation but also better image quality even when compared to conventional single isotope reconstruction performed using analytical projector/backprojector pairs as can be seen from Figure 5.2. This improved image quality may be due to better compensation of photons scattered at small angles and detected under the photopeak in case of Sim-OSEM as it uses realistic MC based scatter correction. Figure 5.3(a) shows vertical line profile

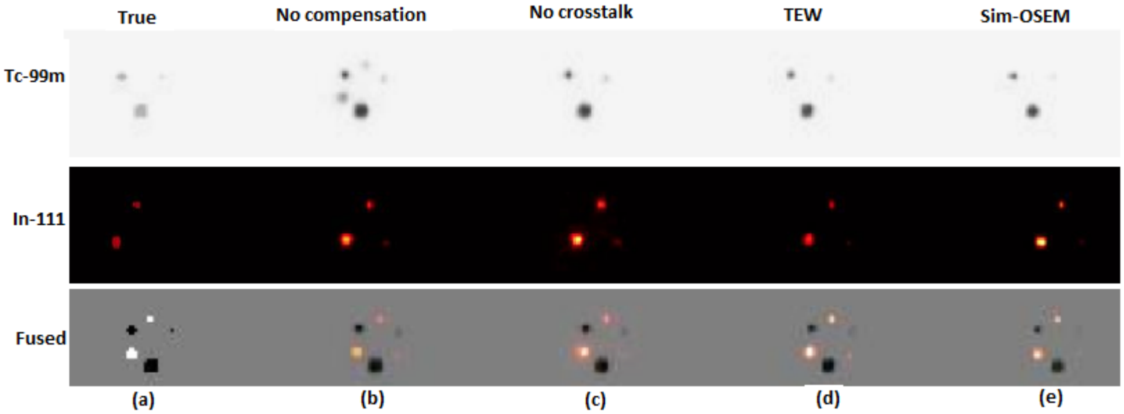

Figure 5.2: At top, in the middle and at bottom are the images for ^{99m}Tc, ^{111}In and fusion of ^{99m}Tc/ ^{111}In respectively. (a) is the true image, (b) is the image reconstructed without crosstalk compensation, (c) image reconstructed using separately acquired data with no crosstalk & (d) image reconstructed using TEW based correction of data with the help conventional analytical reconstruction method and (e) image reconstructed using Sim-OSEM.

through the two spheres having ^{111}In and ^{99m}Tc respectively. Horizontal and vertical profile of maximum counts per pixel in same combined slice of ^{111}In and ^{99m}Tc images, used for profile in Figure 5.3(a), are shown in Figure 5.3(b) and 5.3(c) respectively. The profiles shown in Figure 5.3 indicate improved activity deposition and more uniform background in case of Sim-OSEM compared to TEW based reconstruction. It should be noted that for comparison purposes all the reconstructed data sets except Sim-OSEM (as it already contain activity information) were scaled to actual administered activity levels.

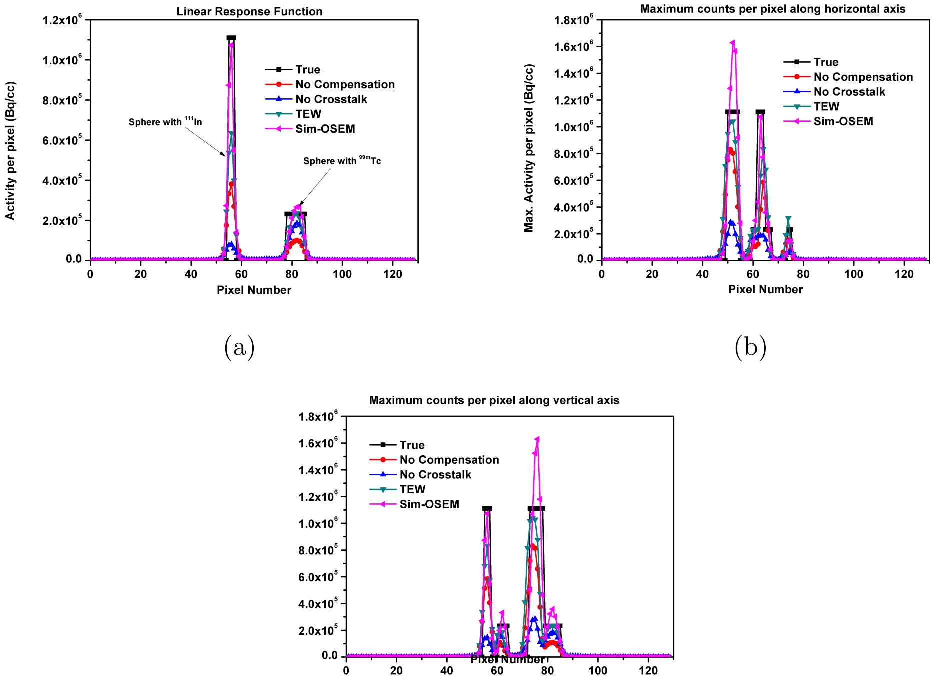

(a)

(b)

(c)

Figure 5.3: (a) Vertical profile showing a line profile through one sphere with ^{99m}Tc and and one ^{111}In showing complete crosstalk compensation and improved spatial resolution, (b)) Horizontal profile showing improved resolution and more uniform background and (c) Vertical profile showing improved resolution and more uniform background in case of Sim-OSEM based reconstruction.

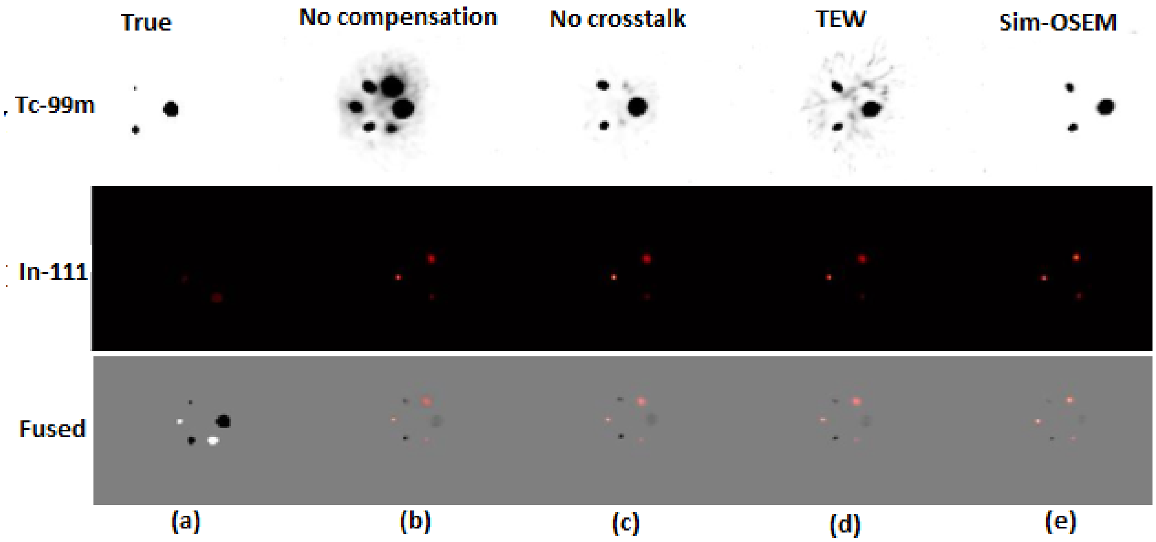

Figure 5.4: At top, in the middle and at bottom are the images for ^{99m}Tc, ^{111}In and fusion of ^{99m}Tc/ ^{111}In respectively. (a) is the true image, (b) is the image reconstructed without crosstalk compensation, (c) image reconstructed using separately acquired data with no crosstalk & (d) image reconstructed using TEW based correction of data with the help conventional analytical reconstruction method and (e) image reconstructed using Sim-OSEM.

5.1.3 Experimental

Data reconstructed from hot sphere phantom studies using a GE Infina dual head gamma camera are shown in Figure 5.4. More uniform background and reduced background activity deposition can be observed (Figure 5.4) for the Sim-OSEM based reconstruction compared to other reconstruction methods.

The results of the proposed method of reconstruction seem to be superior as compared to reconstruction of separately acquired data for each isotope without scatter correction. This is may be due to the fact that better compensation for photons scattered at small angles detected under photopeak can be obtained by Sim-OSEM based reconstruction due to involvement of MC based forward projector in this method.

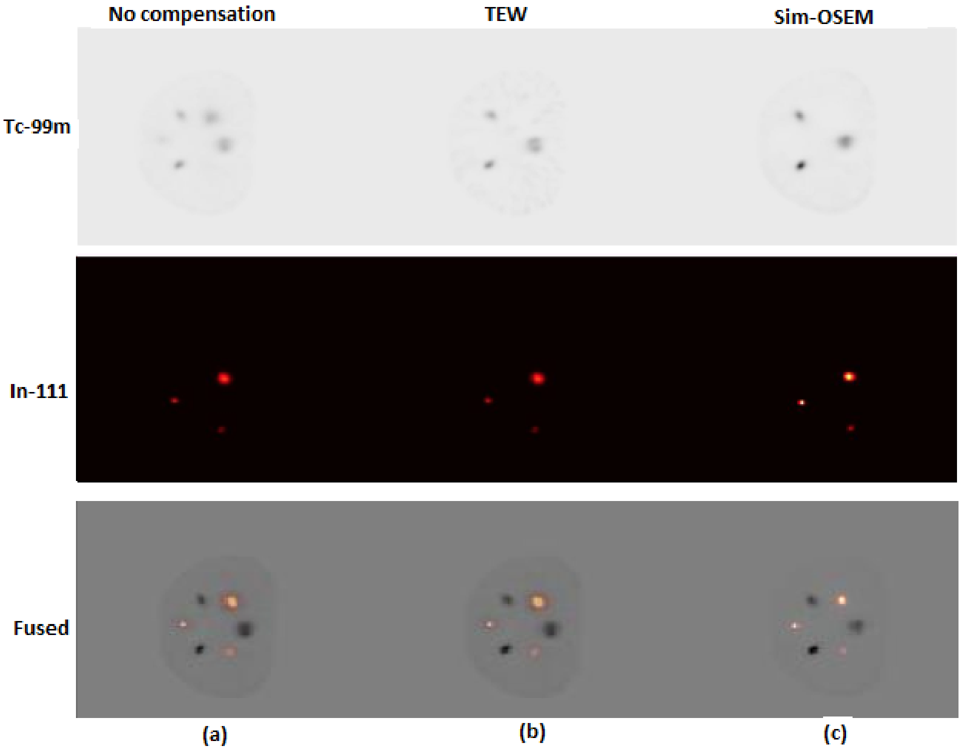

Figure 5.5: At top, in the middle and at bottom are the images for ^{99m}Tc, ^{111}In and fused ^{99m}Tc/ ^{111}In respectively. (a) is the image reconstructed without crosstalk compensation, (b) image reconstructed using TEW based crosstalk correction with the help of conventional analytical reconstruction method and (c) image reconstructed using Sim-OSEM.

Similar results can be seen (Figure 5.5) for the reconstruction of phantom data acquired for hot spheres in ^{99m}Tc background.

5.1.4 Activity Estimation

As mentioned in the previous section, estimation of deposited activity is also possible with our proposed Sim-OSEM based reconstruction method. Table 5.3 shows comparison between actual injected activities to the activity values estimated using Sim-OSEM. Quantitative estimates of activity yielded an overestimation of ^{111}In

Table 5.3: Comparison of actual injected activity with activity values estimated using Sim-OSEM.

		Activity (MBq)		
Acquisition	**Isotope**	**Injected**	**Estimated**	**Error (%)**
MC Simulation	^{99m}Tc	7.75	7.75	0
	^{111}In	17.25	17.15	-0.005
^{99m}Tc/^{111}In in cold background	^{99m}Tc	5.40[a]	4.52	-16.1
	^{111}In	6.70	6.90	3.0
^{99m}Tc/^{111}In in ^{99m}Tc background	^{99m}Tc	118.0 [a]	115.70	-1.9
	^{111}In	6.70	7.33	9.4

[a] activity values after decay correction.

and underestimation of ^{99m}Tc in case of experimental data. This is currently being investigated. However, the quality of images obtained, overestimation of ^{111}In and underestimation of ^{99m}Tc indicates that crosstalk compensation is good.

5.2 ^{99m}Tc/^{123}I Simultaneous SPECT

Simultaneous ^{99m}Tc/^{123}I has shown some potential application in breast SPECT. ^{99m}Tc-MIBI and ^{123}I-estradiol are believed to complement each other in differentiating benign and potentially malignant breast lesions. So far we have performed a number of simulation studies to evaluate simultaneous ^{99m}Tc and ^{123}I SPECT acquisition and reconstruction using Sim-OSEM. The simulation studies include data acquisition

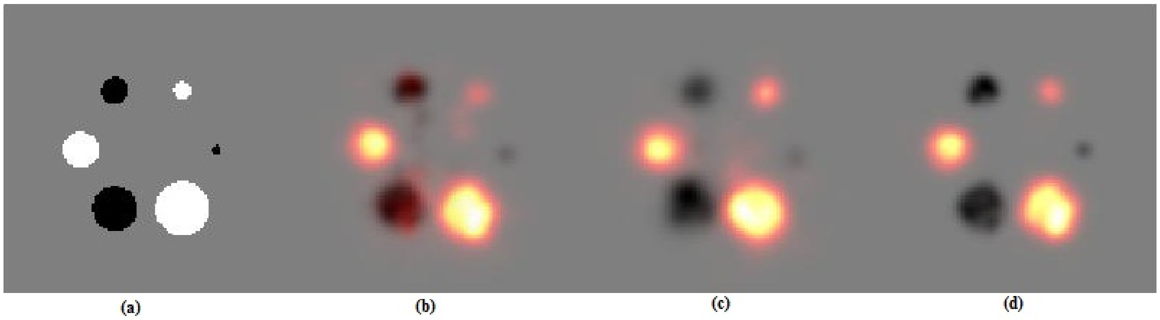

Figure 5.6: (a) True image with white spheres having ^{99m}Tc and black ones of ^{123}I deposited uniformly (b) image reconstructed using conventional analytical projector and backprojector pairs without crosstalk compensation showing significant down-scatter from ^{123}I only spheres into spheres with ^{99m}Tc only (c) Images reconstructed from separately acquired data using conventional reconstruction (d) Images reconstructed using Sim-OSEM showing no crosstalk.

for sources in a water filled cylinder (uniform attenuation map), NCAT phantom (non uniform attenuation map) and SPECT data for different breast sizes. In all the simulation studies MC based forward projector was used to acquire the SPECT data, represented by Equations 4.25 and 4.26. The same forward projector is used for subsequent reconstruction with the help of Sim-OSEM.

5.2.1 Uniform Attenuation Map Simulation

In order to acquire dual-isotope projection data and subsequent reconstruction using MC based forward projector in case of uniform attenuation map, a pixelated cylindrical phantom with six spheres in the centre was used. The pixelated phantom consisted of a non radioactive water filled cylinder (diameter (ϕ) =56 cm) having six spheres of varying radius in the center as shown in Figure 4.5. Three of the spheres (ϕ = 11, 7 and 4 cm respectively, shown in blue in Figure 4.5) were filled uniformly with 20.0 MBq of ^{99m}Tc and an activity of 5.0 MBq of ^{123}I was deposited uniformly

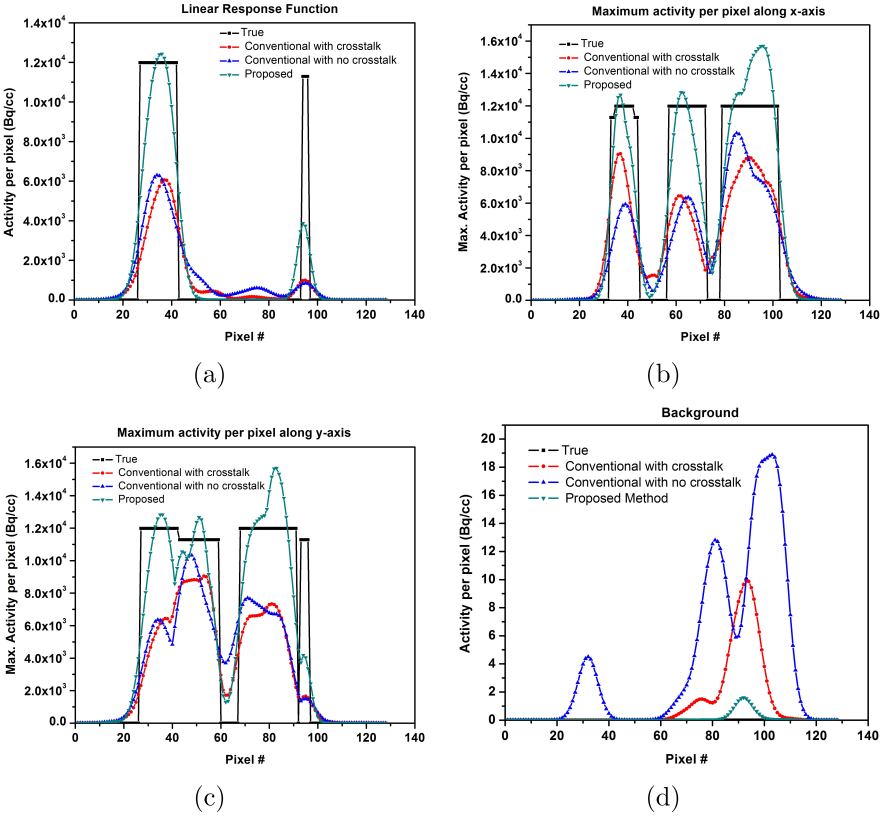

Figure 5.7: (a) Vertical profile showing a line profile through one sphere with ^{99m}Tc and and one ^{111}In showing complete crosstalk compensation and improved spatial resolution, (b)) Horizontal profile showing improved resolution and more uniform background and (c) Vertical profile showing improved resolution and (d) Background profile showing more uniform background in case of Sim-OSEM based reconstruction.

in the remaining three spheres ($\phi = 9$, 5 and 2 cm respectively, shown in green in Figure 4.5). Acquisition and reconstruction using Sim-OSEM made use of asymmetric (126-150 keV for ^{99m}Tc and 151-174.9 keV for ^{123}I) primary energy windows in order to avoid overlapping of two peaks as can be seen from Figure 3.1(b).

From Figure 5.6(d) it can be seen that there is not only very good crosstalk compensation but also some improvement in image quality compared to conventional reconstruction using analytical projector/backprojector pairs (Figure 5.6 (b)). It is also observed that image reconstructed using standard single isotope reconstruction of separately acquired data with no crosstalk, (Figure 5.6(c)) depicts results which are inferior in terms of scatter correction compared to Sim-OSEM. Estimated activity using proposed reconstruction method is 20.05 and 4.76 MBq for ^{99m}Tc and ^{123}I respectively, which is approximately equal to the respective deposited activities.

Figure 5.7(a) shows vertical line profiles through the two spheres having ^{123}I and ^{99m}Tc respectively. Horizontal and vertical profiles of maximum counts per pixel in the same combined slice of ^{123}I and ^{99m}Tc images, used for profile in Figure 5.7(a), are shown in Figure 5.7(b) and 5.7(c) respectively. The profiles shown in Figure 5.7 indicate better activity deposition and more uniform background in the case of Sim-OSEM compared to single isotope SPECT reconstruction of data with no crosstalk. It should be noted that for comparison purposes all the reconstructed data sets with the exception of Sim-OSEM were scaled to actual injected activity levels. More uniform background is also evident from Figure 5.7(d)

5.2.2 Non-uniform Attenuation Map Simulation

In order to verify the accuracy of crosstalk compensation in MC based reconstruction in the case of projection data acquired using non-uniform attenuation map, the digital NURBS-based Cardio-torso (NCAT) phantom was used. For this purpose a tumor was introduced in the right axillary region and 10 MBq of ^{123}I was deposited in the tumor compare to 100 MBq of ^{99m}Tc deposited in bones. From Figure 5.8(b) in ^{99m}Tc images reconstructed using conventional reconstruction without crosstalk compensation, we can see that there is a tumor in ^{99m}Tc image which should not be there as it has only ^{123}I in it. This crosstalk has been compensated in case of

Table 5.4: Comparison of actual injected activity with activity values estimated using Sim-OSEM.

	Activity (MBq)		
Isotope	**Deposited**	**Estimated**	Error(%)
^{99m}Tc	100.0	99.69	-0.003
^{123}I	10.0	10.04	0.004

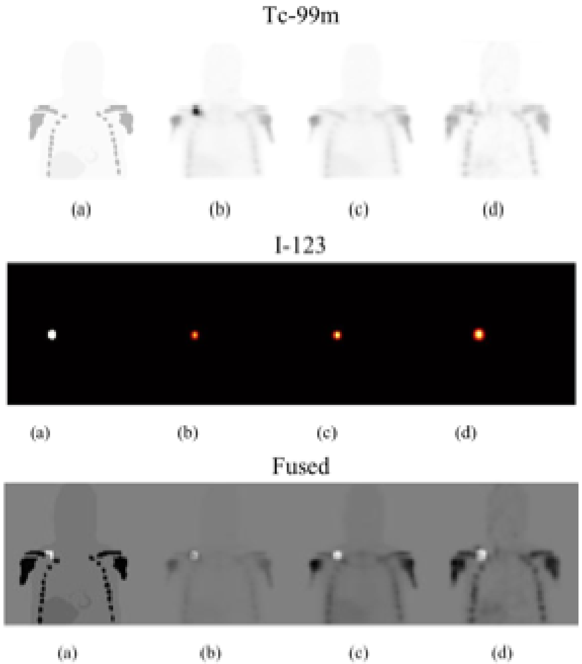

Figure 5.8: At top, in the middle and at bottom are the images for ^{99m}Tc, ^{123}I and fusion of ^{99m}Tc / ^{123}I images at top and in the middle respectively. (a) is the true image, (b) is the image reconstructed using conventional analytical reconstruction method without crosstalk compensation (c) image reconstructed using separately acquired data with no crosstalk using conventional reconstruction (d) image reconstructed using MC based reconstruction.

Sim-OSEM based reconstruction as can be seen in Figure 5.8(d) in ^{99m}Tc images. It is also evident from the fact that the estimated activity in images reconstructed using Sim-OSEM is 10.04 and 99.69 MBq for ^{123}I and ^{99m}Tc respectively, which is very close to the actually injected activities. The encouraging results of proposed method of reconstruction seem to be superior may be due to MC based scatter compensation and more uniform background that ones obtained by Sim-OSEM compare to reconstruction of separately acquired data for each isotope without scatter correction. Table 5.4 shows a comparison between administered and activity estimated for Sim-OSEM.

5.2.3 Breast SPECT

Simultaneous ^{99m}Tc/^{123}I has potential application in imaging for breast cancer [69, 70]. It has been mentioned previously that ^{123}I-estradiol is thought to complement ^{99m}Tc-MIBI in breast SPECT in order to distinguish between benign and potentially malignant lesions non invasively [71]. In order to evaluate SPECT reconstruction of simultaneously acquired ^{99m}Tc/^{123}I projection data three different breast size phantoms with spherical lesions were designed. Details of the designed phantoms can be seen in Section 4.3.5. For each of the breast sizes (i.e. small, medium and large) three lesions were simulated with ^{99m}Tc only, both ^{99m}Tc/^{123}I and ^{123}I only respectively. Ten different combination of lesions with three lesions per combination were selected randomly for simulation of each of the breast sizes. Table A.1 in appendix A shows the details of lesions combinations selected randomly for each of the three breast sizes.

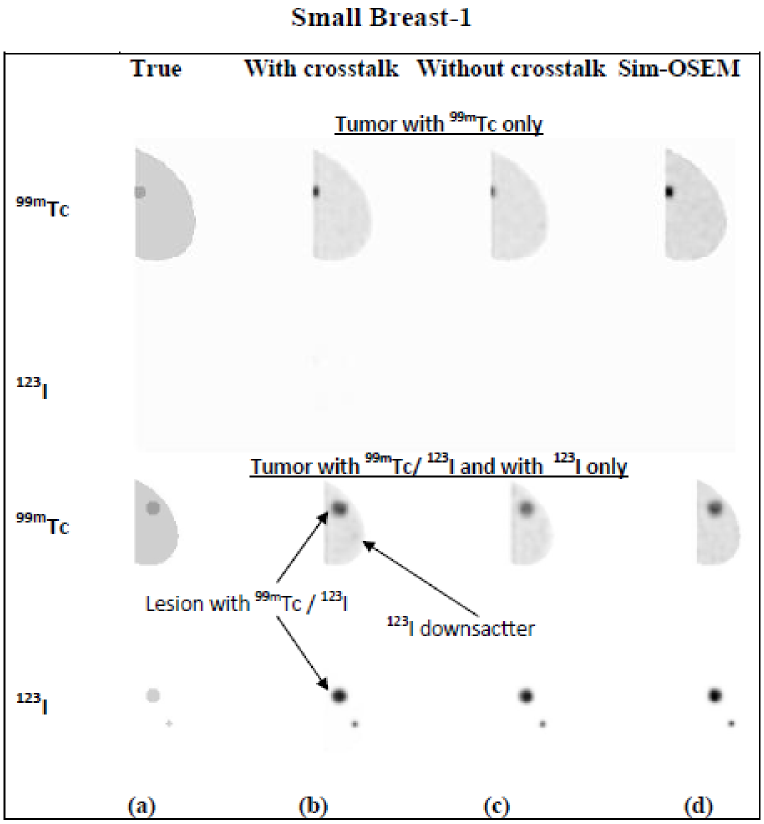

Figure 5.9: At top and at bottom are the slices through lesions with with ^{99m}Tc only and both ^{99m}Tc/^{123}I & ^{123}I only respectively (^{99m}Tc and ^{123}I shown on separate rows). (a) is the true image, (b) is the image reconstructed using conventional analytical reconstruction method without crosstalk compensation (c) image reconstructed using separately acquired data with no crosstalk using conventional reconstruction (d) image reconstructed using Sim-OSEM

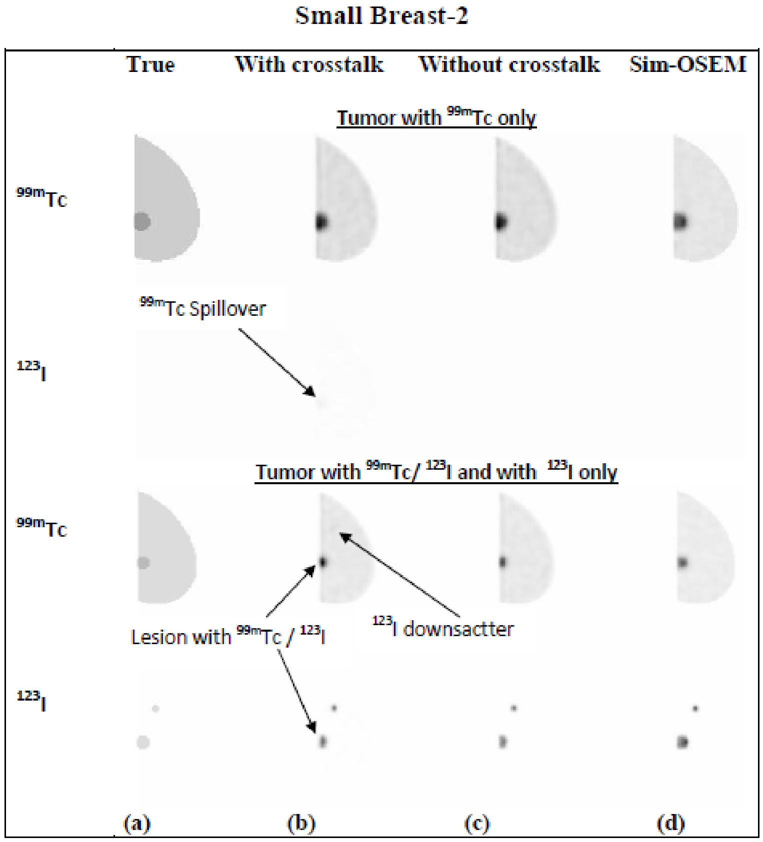

Figure 5.10: At top and at bottom are the slices through lesions with with ^{99m}Tc only and both ^{99m}Tc/^{123}I & ^{123}I only respectively (^{99m}Tc and ^{123}I shown on separate rows). (a) is the true image, (b) is the image reconstructed using conventional analytical reconstruction method without crosstalk compensation (c) image reconstructed using separately acquired data with no crosstalk using conventional reconstruction (d) image reconstructed using Sim-OSEM

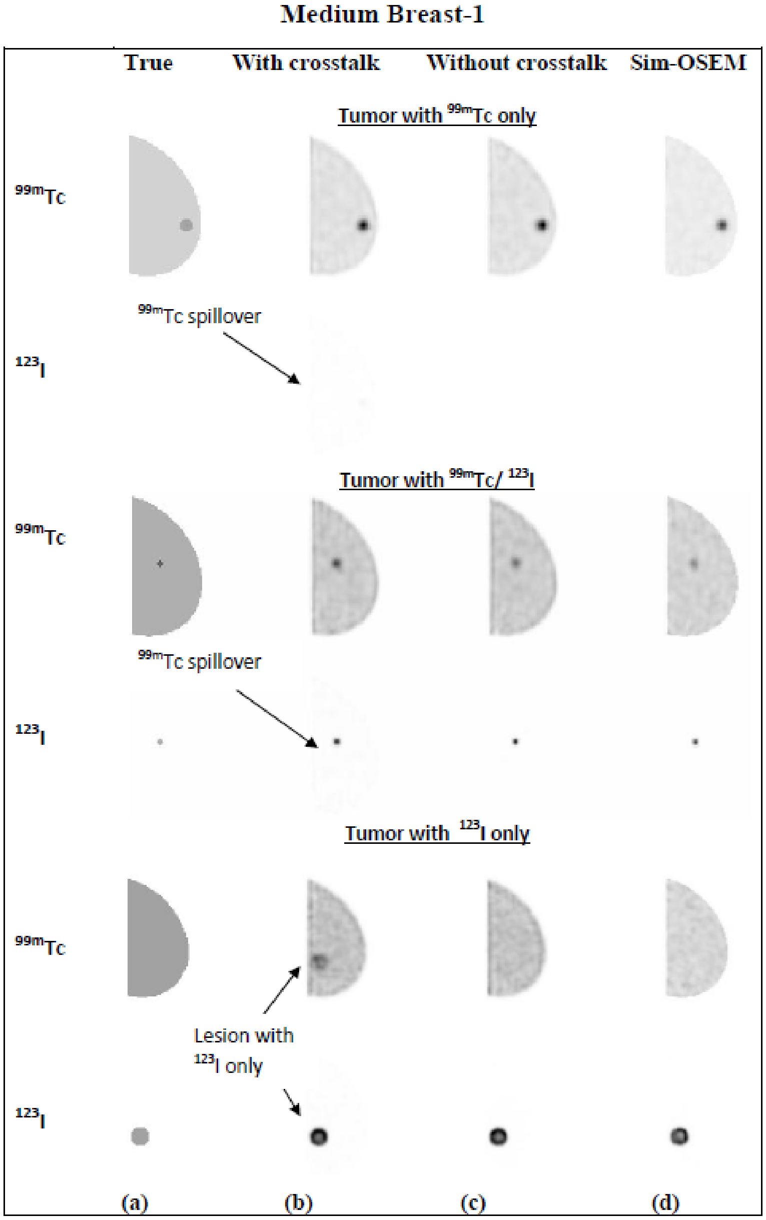

Figure 5.11: At top, in the middle and at bottom are the slices through lesions with ^{99m}Tc only and with both ^{99m}Tc/^{123}I and ^{123}I only respectively (^{99m}Tc and ^{123}I shown on separate rows). (a) is the true image, (b) is the image reconstructed using conventional analytical reconstruction method without crosstalk compensation (c) image reconstructed using separately acquired data with no crosstalk using conventional reconstruction (d) image reconstructed using Sim-OSEM

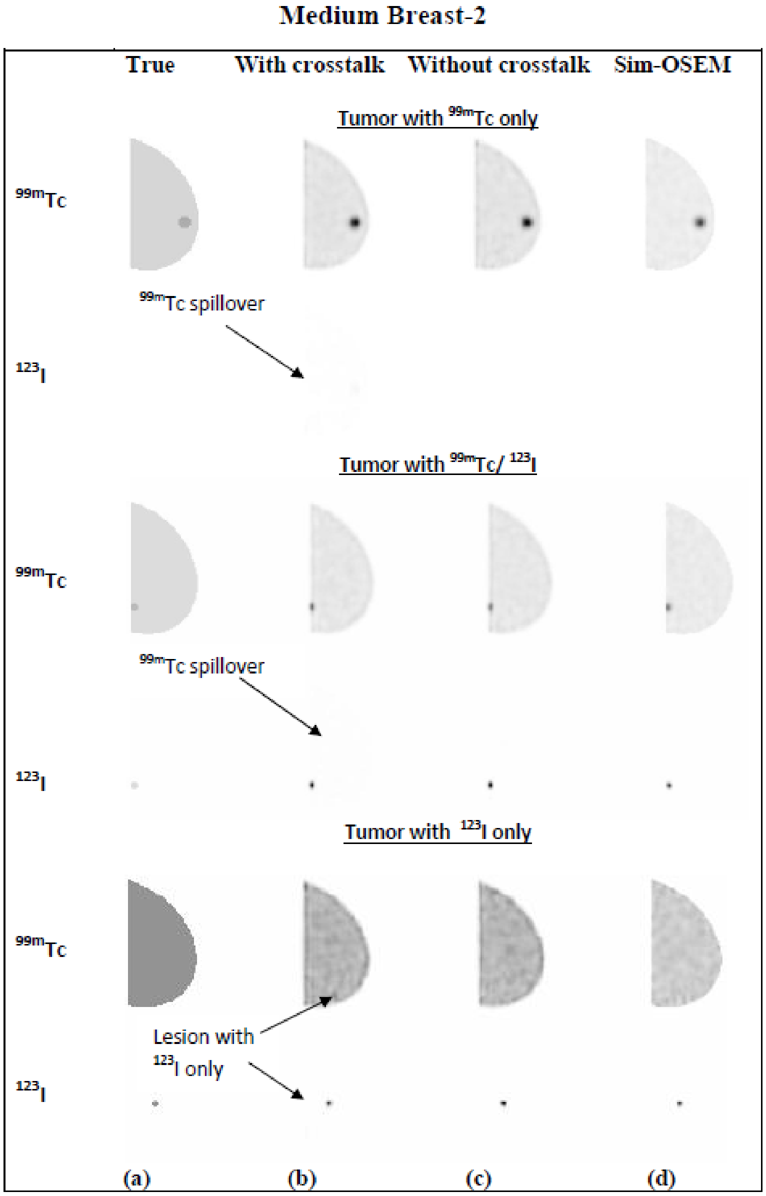

Figure 5.12: At top, in the middle and at bottom are the slices through lesions with ^{99m}Tc only and with both ^{99m}Tc/^{123}I and ^{123}I only respectively (^{99m}Tc and ^{123}I shown on separate rows). (a) is the true image, (b) is the image reconstructed using conventional analytical reconstruction method without crosstalk compensation (c) image reconstructed using separately acquired data with no crosstalk using conventional reconstruction (d) image reconstructed using Sim-OSEM

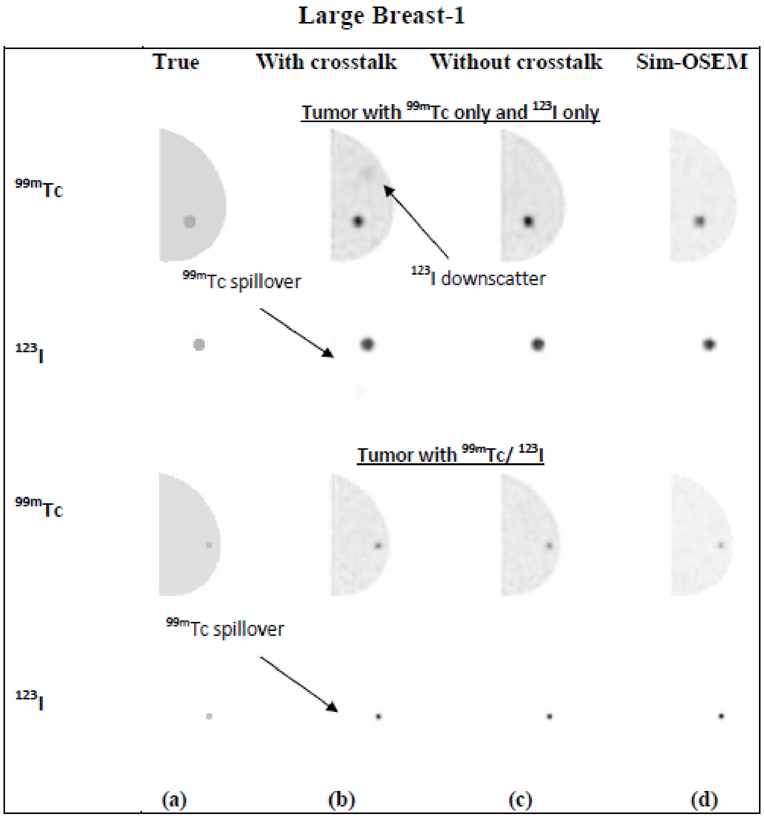

Figure 5.13: At top and at bottom are the slices through lesions with with ^{99m}Tc only & ^{123}I only and both ^{99m}Tc/^{123}I respectively (^{99m}Tc and ^{123}I shown on separate rows). (a) is the true image, (b) is the image reconstructed using conventional analytical reconstruction method without crosstalk compensation (c) image reconstructed using separately acquired data with no crosstalk using conventional reconstruction (d) image reconstructed using Sim-OSEM

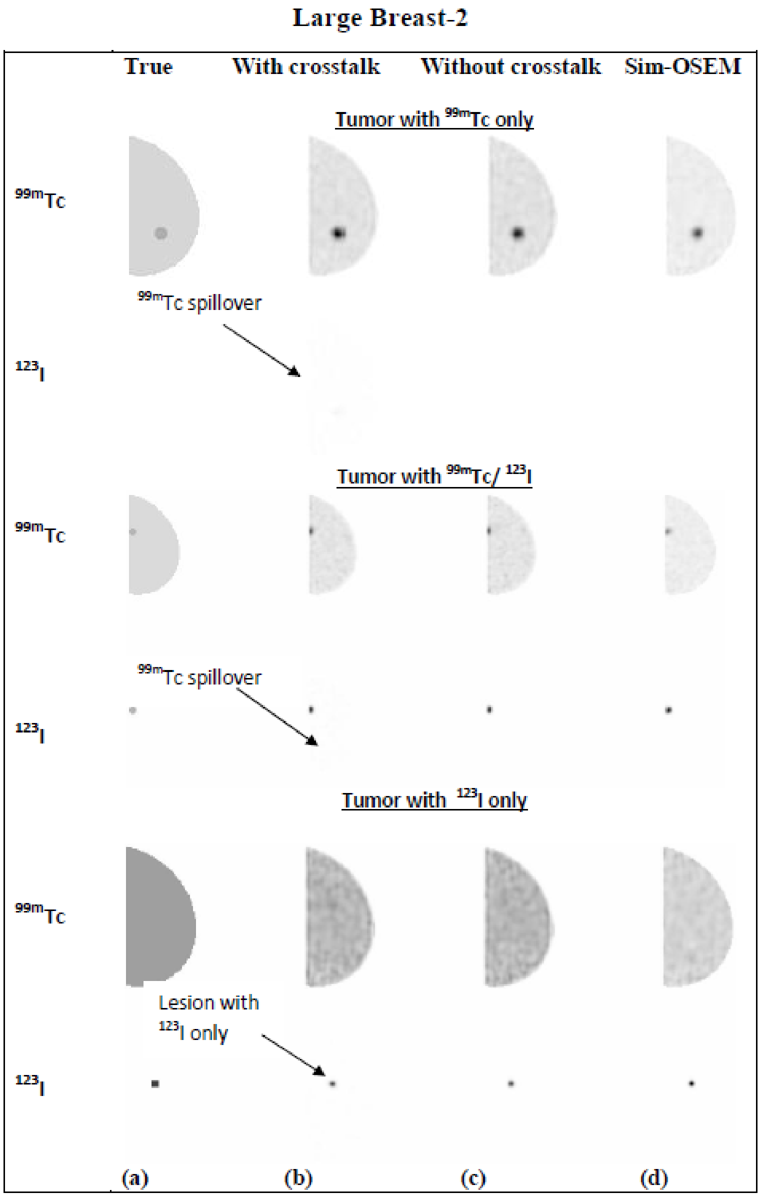

Figure 5.14: At top, in the middle and at bottom are the slices through lesions with ^{99m}Tc only and with both ^{99m}Tc/^{123}I and ^{123}I only respectively (^{99m}Tc and ^{123}I shown on separate rows). (a) is the true image, (b) is the image reconstructed using conventional analytical reconstruction method without crosstalk compensation (c) image reconstructed using separately acquired data with no crosstalk using conventional reconstruction (d) image reconstructed using Sim-OSEM

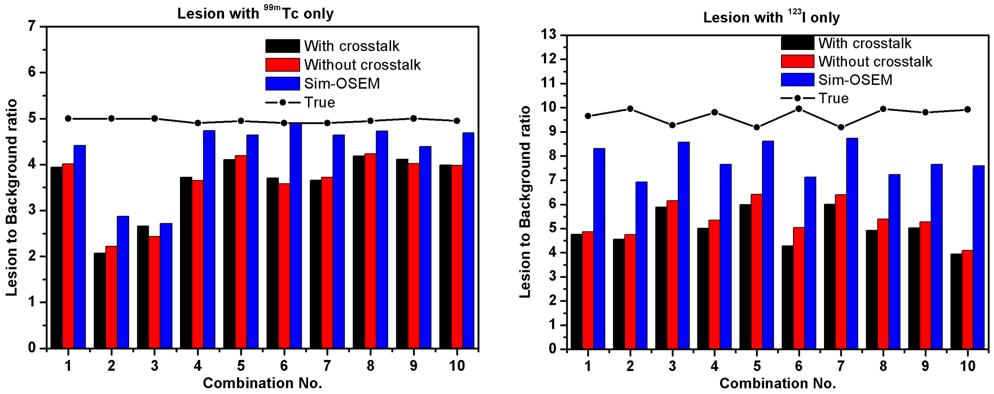

(a) Lesion to background ratios for lesions with ^{99m}Tc only.

(b) Lesion to background ratios for lesions with ^{123}I only.

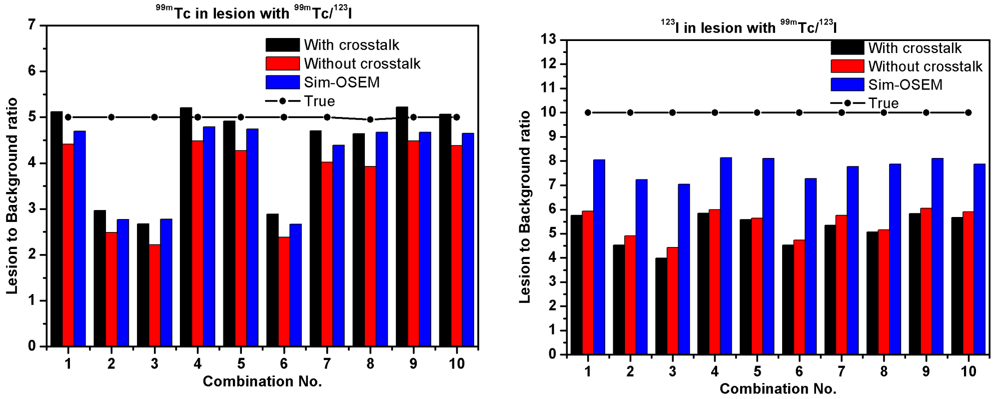

(c) ^{99m}Tc lesion to background ratios for lesions with ^{99m}Tc/^{123}I.

(d) ^{123}I lesion to background ratios for lesions with ^{99m}Tc/^{123}I.

Figure 5.15: Comparison of lesion to background ratios estimated for different reconstruction methods with the true values of lesion to background ratios in the case of small breast size.

Table 5.5: Comparison of mean lesion to background ratios between different reconstruction methods

	Isotope	**Small Breast**	**Medium Breast**	**Large Breast**
True	^{99m}Tc	4.96±0.05	5.00±0.00	4.99±0.08
	^{99m}Tc†	4.99± 0.05	4.99± 0.12	5.00±0.03
	^{123}I*	10.00±0.00	10.00± 0.00	10.00±0.00
	^{123}I	9.67±0.48	9.62±0.57	9.59±1.62
With Crosstalk	^{99m}Tc	3.62±1.54	4.50± 1.27	3.73±1.20
	^{99m}Tc†	4.34±1.66	4.00 ± 1.14	4.26±0.85
	^{123}I*	5.22±1.23	4.56 ± 0.80	4.32±0.66
	^{123}I	5.04±2.05	4.64± 1.62	4.17±0.73
Without Crosstalk	^{99m}Tc	3.61±1.38	4.53 ± 1.10	3.73±1.20
	^{99m}Tc†	3.71±1.49	3.40± 1.11	4.26±0.85
	^{123}I*	5.45±1.02	4.57± 0.95	4.32±0.66
	^{123}I	5.37±2.33	4.93± 1.28	4.17±0.73
Sim-OSEM	^{99m}Tc	4.27±1.56	4.46± 1.54	4.51±1.76
	^{99m}Tc†	4.08±1.41	3.87± 1.29	4.55±1.06
	^{123}I*	7.75±0.71	7.68± 0.65	7.88±1.00
	^{123}I	7.85±1.13	7.96 ± 1.05	8.30±0.85

† ^{99m}Tc lesion to background ratio for lesion with ^{123}I/^{99m}Tc.

* ^{123}I lesion to background ratio for lesion with ^{123}I/^{99m}Tc.

Reconstruction Results

The two simulation results for each of the breast sizes are shown in the Figures 5.9 & 5.9 , 5.11 & 5.12 and 5.13 & 5.14 respectively as examples. These results were obtained from i) analytical attenuation based reconstruction of data uncorrected for crosstalk, ii) single isotope data without any crosstalk contribution from other isotope and iii) reconstruction using Sim-OSEM for small, medium and large sized breast phantoms respectively. Analytical attenuation based reconstruction uses analytical projector/backprojector pair incorporated into standard OSEM reconstruction algorithm. It is quite evident from the results that Sim-OSEM based reconstruction gives images comparable to crosstalk-free single isotope reconstructed images. It can also be observed in the images reconstructed from the simultaneously acquired data without crosstalk compensation that crosstalk contribution becomes negligible for deep-seated small lesions. This may be due to the fact that size of the object with depth of lesion are important factor in determination of the amount of scatter that is larger the size and lesser the depth of object to be imaged greater is the amount of scatter and vice versa. In order to compare different reconstruction methods used for breast data reconstruction, lesion to background ratios were calculated for all the lesion combinations for each of the breast sizes. Figure 5.15 shows graphical representation of lesion to background ratios for lesions with ^{99m}Tc only, ^{123}I only and both ^{99m}Tc/^{123}I respectively in the case of small breast size. From the graph it can be seen that the Sim-OSEM give much better and much more realistic lesion to background ratios when compare to other reconstruction methods. It should also be noted from the figure that in case of lesion with both ^{99m}Tc/^{123}I show higher lesion to background ratios when images reconstructed without crosstalk correction. This may be due to downscatter from ^{123}I. Similar results can be seen for medium and large breast sizes from the Figure A.1 and A.2 in appendix A respectively. Table 5.5 compares the mean lesions to background ratios for different reconstruction methods to corresponding actual values of lesion to background ratios. Larger discrepancies in lesion to background ratios were observed for deep seated small lesions, which is an indication of under-compensation for attenuation effect. Detailed results in tabular form can be found in Tables A.2, A.3 and A.4 in appendix A.

Activity Estimation

As mentioned in Section 4.5 that estimation of deposited activity is also possible with Sim-OSEM based reconstruction method. Figure 5.16 shows comparison between actual administered activities to the activity values estimated using Sim-OSEM for all the lesion combinations simulated for each of the breast sizes. It is evident from the figure that the Sim-OSEM gives quite accurate estimates of total activities. These results are given in tabular form in Table B.5 in appendix B. Relatively small error can be seen in case of Sim-OSEM based reconstruction of data acquired using MC based forward projector. It should be noted that relatively large error was observed for small activities (<1 MBq). This may be due to under-correction of attenuation effects for deep seated small size lesions.

Figure 5.17 shows a comparison between Sim-OSEM based estimated lesion activities with the actual values of administered activities for the small breast. From the figure it can be seen that Sim-OSEM yields good estimate of actual administered lesion activities. It can be seen from the figure that in most of the cases the lesion activities are slightly underestimated. However, in some cases there is a slight over-estimation of ^{99m}Tc activities which indicates under-compensation of crosstalk. Similar results can be seen for medium and large breast sizes from the Figure B.3 and B.4 in appendix B respectively. The estimated and administered lesion activities for all the combinations for each of the breast sizes are given in Tables B.6, B.7 and B.8 in appendix B.

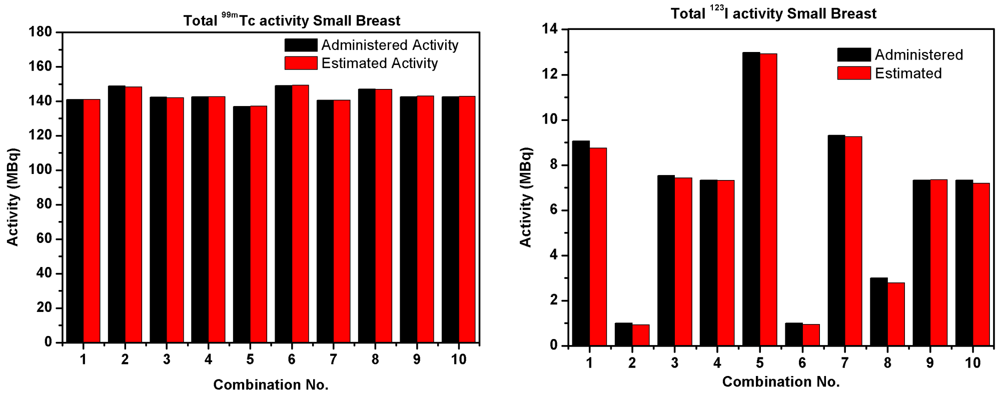

(a) Total ^{99m}Tc activity in small breast. (b) Total ^{123}I activity in small breast.

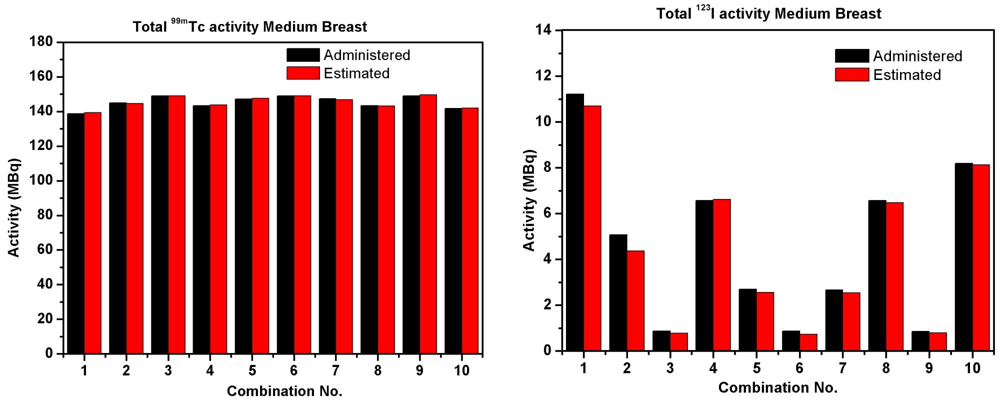

(c) Total ^{99m}Tc activity in medium breast. (d) Total ^{123}I activity in medium breast.

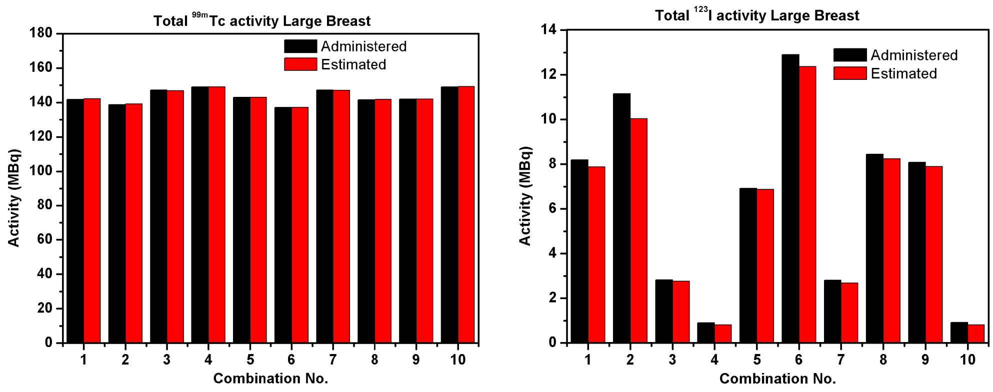

(e) Total ^{99m}Tc activity in large breast. (f) Total ^{123}I activity in large breast

Figure 5.16: Comparison of total ^{99m}Tc and ^{123}I activity estimated using Sim-OSEM with actually administered activity for all the lesion combinations for small, medium and large breast sizes respectively.

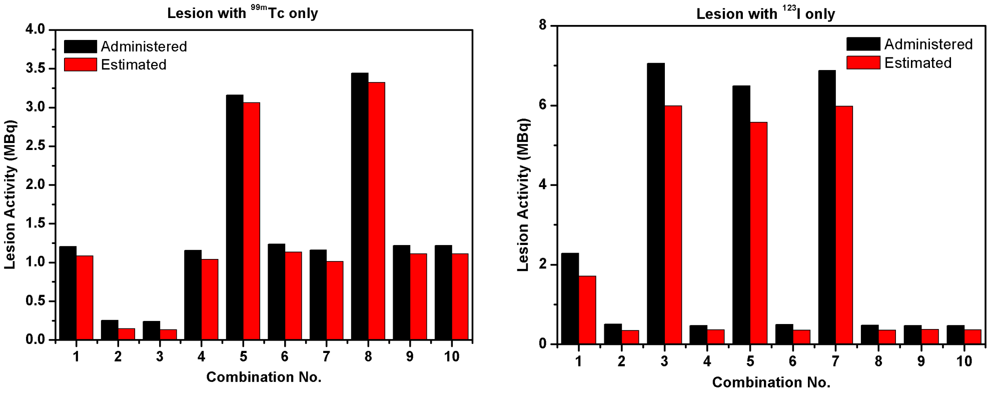

(a) Activity for lesion with ^{99m}Tc only. (b) Activity for lesion with ^{123}I only.

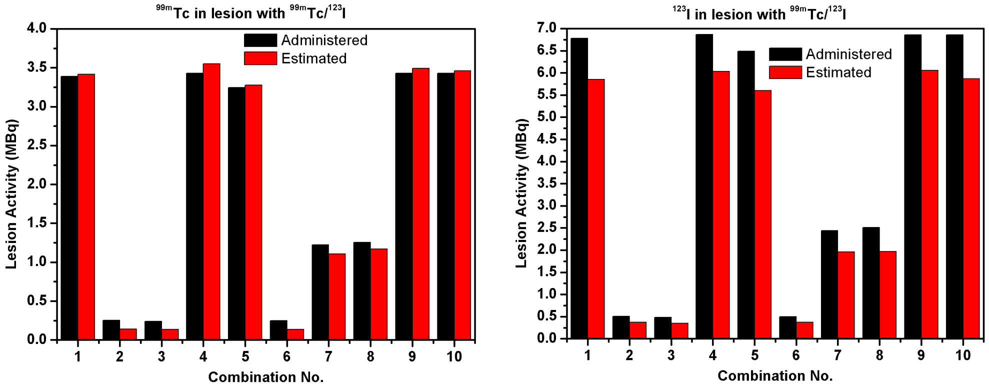

(c) ^{99m}Tc activity for lesion with ^{99m}Tc/^{123}I. (d) ^{123}I activity for lesion with ^{99m}Tc/^{123}I.

Figure 5.17: Comparison of lesion activities estimated from Sim-OSEM with the actually administered lesion activities in the case of small breast size.

Chapter 6

Conclusion and Future Work

The aim of this research work is to make simultaneous dual isotope SPECT data acquisition feasible without degradation of the resulting image. The main source of image degradation, if dual isotope data is acquired simultaneously, is the crosstalk between the isotopes involved in the imaging. In this thesis a dual isotope reconstruction method named Sim-OSEM, is introduced to correct for the crosstalk. This chapter briefly describes the conclusion and possible future work which can be done in order to validate, evaluate and to make the Sim-OSEM practically applicable.

6.1 Conclusion

As discussed in Section 4.2.1 SIMIND MC code has been made feasible to use in clinical time frames by implementation of VRT's such as convolution forced detection (CFD) [62]. In this work the accelerated SIMIND MC code has been incorporated into an algorithm used to reconstruct simultaneously acquired dual isotope SPECT data. The accuracy and compatibility of MC accelerated using convolution based forced detection (CFD), with experimental data was evaluated using point source data for ^{111}In/^{99m}Tc in terms of spatial resolution and sensitivity. The point source data showed some discrepancy in spatial resolution along the horizontal direction in case of MC code. All the simulation studies performed using ^{111}In/^{99m}Tc and ^{123}I/^{99m}Tc simultaneously acquired data showed almost complete crosstalk compensation in case Sim-OSEM based reconstruction compared to other reconstruction algorithm. The Sim-OSEM based reconstruction has an additional advantage of accurate activity estimation. The relatively large error in activity estimation in Sim-OSEM based reconstruction of ^{111}In/^{99m}Tc experimental data was observed, which may be due to slight difference between measured and simulated sensitivity values. In short, the results acquired using the proposed method of reconstruction (i.e. Sim-OSEM) so far are quite promising as far as compensation of crosstalk and estimation of deposited activity is concerned .

6.2 Future Work

Preliminary evaluation work has been performed only in the case of ^{99m}Tc/^{111}In simultaneous SPECT. Simulation as well experimental evaluation has been performed using a uniform attenuation map in form of NEMA IEC body phantom set. In the future, some experiment using non uniform maps should be performed to evaluate the effectiveness of Sim-OSEM. Experimental verification of Sim-OSEM in case of simultaneous ^{123}I/^{99m}Tc has yet to be performed. It should be noted that in simulation studies both uniform as well non uniform attenuation map in form of NCAT phantom were used. The studies using ^{123}I/^{99m}Tc also needed to be evaluated experimentally. Similar simulations as well as experimental studies should also be performed. One of the prime example of one such isotope duo is ^{201}Tl/^{99m}Tc used in cardiac imaging.

One of the goals of this work is to use data acquired using NaI(Tl) based gamma cameras. Currently Cadmium Zinc Telluride (CZT) based dedicated cardiac and scintimammography scanners are becoming popular. The costly CZT scanners are believed to provide dual radio-nuclide images comparable to those obtained from reconstruction of separately acquired data for each isotope as described by Ben Haim *et al* [72]. In the future a comparative study can be performed to compare the quality of images obtained using CZT scanners to the images reconstructed using Sim-OSEM.

In order to improve the accuracy and performance of the proposed algorithm, experiments to optimize acquisition parameters for different simultaneous dual isotope SPECT imaging as described by Wang *et al* [73] and Du *et al* [74] should also be performed.

The assessment of image quality is an important tool in medical imaging research in order to compare two competing systems or image processing algorithms. The most useful, meaningful and reproducible way to image quality assessment performed by a human observer is *receiver operating characteristic* (ROC) analysis. In ROC analysis a plot between true positive (or sensitivity) as a function of false positive (or 1-specificity) is used to compare different systems, protocols or image processing algorithm. ROC analysis of task based image quality assessment for Sim-OSEM based reconstruction compare to other dual isotope reconstruction algorithms may also be performed in future. Rather than using human observer, a mathematical observer, implemented in form of a computer algorithm, can also be used to perform the image quality assessment task. After establishing the accuracy and applicability of the proposed reconstruction method, mathematical observer studies may also be performed as done by Song *et al* [75] In this work mathematical observer studies were performed for evaluation of their model-based crosstalk compensation method in simultaneous ^{99m}Tc/^{201}Tl myocardial perfusion SPECT. The image quality assessment tasks should be performed for all the different isotope combinations, which are either being used as well as potential candidates for multi-isotope SPECT in future.

Last but not least Sim-OSEM based dual isotope reconstruction takes 6-8 hrs. for 2 iterations and 30 subsets. Therefore there is clearly room of improvement in terms of increase in the simulation speed of MC based forward projector.

Appendix A

Lesion to Background Ratios

Table A.1: Lesion Radii of randomly selected ten sets of lesions with 3 lesions per set for each of the breast sizes.

		Radius(mm) of Lesion with		
Breast Size	No.	^{99m}Tc only	^{123}I/^{99m}Tc	^{123}I only
Small	1	14	5.6	4
	2	2.4	2.4	2.4
	3	2.4	2.4	5.6
	4	4	5.6	2.4
	5	5.6	5.6	5.6
	6	4	2.4	2.4
	7	4	4	5.6
	8	5.6	4	2.4
	9	4	5.6	2.4
	10	4	5.6	2.4
Medium	1	5.5	7.7	7.7
	2	5.5	7.7	3.3
	3	5.5	3.3	3.3
	4	5.5	3.3	7.7
	5	3.3	3.3	5.5
	6	5.5	3.3	3.3
	7	5.5	5.5	3.3
	8	5.5	3.3	7.7
	9	7.7	3.3	3.3
	10	5.5	5.5	7.7
Large	1	7	9.8	7
	2	4.2	4.2	12.6
	3	4.2	7	4.2
	4	9.8	4.2	4.2
	5	7	4.2	9.8
	6	9.8	12.6	4.2
	7	7	7	4.2
	8	4.2	9.8	7
	9	12.6	9.8	7
	10	7	4.2	4.2

Table A.2: Comparison of lesion to background ratios for small breast size for different reconstruction algorithms.

	No./ Isotope	1	2	3	4	5	6	7	8	9	10	**Mean**
True	^{99m}Tc	5.00	5.00	5.00	4.90	4.95	4.90	4.90	4.95	5.00	4.95	4.96±0.05
	^{99m}Tc†	5.00	5.00	5.00	5.00	5.00	5.00	5.00	4.95	5.00	5.00	4.99± 0.05
	^{123}I*	10.00	10.00	10.00	10.00	10.00	10.00	10.00	10.00	10.00	10.00	10.00±0.00
	^{123}I	9.65	9.95	9.27	9.81	9.19	9.95	9.19	9.95	9.81	9.92	9.67±0.48
With Crosstalk	^{99m}Tc	3.94	2.07	2.66	3.72	4.11	3.71	3.66	4.19	4.12	3.99	3.62±1.54
	^{99m}Tc†	5.12	2.97	2.68	5.21	4.92	2.89	4.70	4.64	5.22	5.07	4.34±1.66
	^{123}I*	5.77	4.53	3.99	5.84	5.59	4.53	5.35	5.08	5.83	5.67	5.22±1.23
	^{123}I	4.77	4.56	5.89	5.02	5.99	4.28	6.00	4.92	5.03	3.95	5.04±2.05
Without Crosstalk	^{99m}Tc	4.01	2.23	2.44	3.65	4.19	3.59	3.72	4.23	4.02	3.99	3.61±1.38
	^{99m}Tc†	4.41	2.48	2.22	4.49	4.27	2.38	4.02	3.93	4.48	4.38	3.71±1.49
	^{123}I*	5.94	4.91	4.43	5.99	5.65	4.73	5.76	5.16	6.06	5.91	5.45±1.02
	^{123}I	4.87	4.74	6.16	5.35	6.41	5.05	6.40	5.39	5.28	4.09	5.37±2.33
Sim-OSEM	^{99m}Tc	4.42	2.88	2.71	4.74	4.64	4.89	4.64	4.73	4.39	4.69	4.27±1.56
	^{99m}Tc†	4.70	2.77	2.78	4.79	4.74	2.67	4.39	4.67	4.68	4.65	4.08±1.41
	^{123}I*	8.05	7.24	7.04	8.14	8.11	7.28	7.77	7.87	8.11	7.88	7.75±0.71
	^{123}I	8.32	6.92	8.58	7.66	8.61	7.13	8.74	7.24	7.65	7.60	7.85±1.13

† ^{99m}Tc lesion to background ratio for lesion with ^{123}I/^{99m}Tc.

* ^{123}I lesion to background ratio for lesion with ^{123}I/^{99m}Tc.

Table A.3: Comparison of lesion to background ratios for medium breast size for different reconstruction algorithms.

	Set No./ Isotope	1	2	3	4	5	6	7	8	9	10	**Mean**
True	^{99m}Tc	5.00	5.00	5.00	5.00	5.00	5.00	5.00	5.00	5.00	5.00	5.00±0.00
	^{99m}Tc†	5.00	4.87	5.00	5.00	5.00	5.00	5.00	5.00	5.00	5.00	4.99± 0.12
	^{123}I*	10.00	10.00	10.00	10.00	10.00	10.00	10.00	10.00	10.00	10.00	10.00± 0.00
	^{123}I	9.04	9.92	9.95	9.17	9.71	9.95	9.92	9.26	9.95	9.26	9.62±0.57
With Crosstalk	^{99m}Tc	3.79	3.82	4.86	4.87	3.23	4.85	4.83	5.22	4.48	5.03	4.50± 1.27
	^{99m}Tc†	5.14	3.98	3.32	2.94	4.10	3.84	4.81	3.61	3.86	4.45	4.00 ± 1.14
	^{123}I*	5.01	3.83	4.22	3.89	4.47	4.26	4.75	5.18	5.36	4.66	4.56 ± 0.80
	^{123}I	4.63	3.96	3.86	5.36	6.26	3.73	4.18	5.24	4.05	5.16	4.64± 1.62
Without Crosstalk	^{99m}Tc	3.87	3.87	4.87	4.87	3.43	4.84	4.86	5.11	4.41	5.14	4.53 ± 1.10
	^{99m}Tc†	4.51	3.46	2.91	2.34	3.21	3.14	4.13	3.34	3.16	3.78	3.40± 1.11
	^{123}I*	5.16	3.77	4.45	4.12	4.10	3.84	4.83	5.34	5.52	4.61	4.57± 0.95
	^{123}I	4.90	4.08	4.31	5.68	6.20	4.48	4.11	5.63	4.41	5.49	4.93± 1.28
Sim-OSEM	^{99m}Tc	4.50	4.47	4.69	4.52	2.91	4.58	4.68	4.66	4.85	4.69	4.46± 1.54
	^{99m}Tc†	4.97	4.77	2.97	2.58	4.14	4.02	4.74	2.95	2.96	4.61	3.87± 1.29
	^{123}I*	8.33	8.13	7.63	7.41	7.38	7.16	8.00	7.40	7.30	8.07	7.68± 0.65
	^{123}I	8.98	7.20	6.91	8.84	8.05	6.92	7.66	8.84	7.38	8.81	7.96 ± 1.05

† ^{99m}Tc lesion to background ratio for lesion with ^{123}I/^{99m}Tc.

* ^{123}I lesion to background ratio for lesion with ^{123}I/^{99m}Tc.

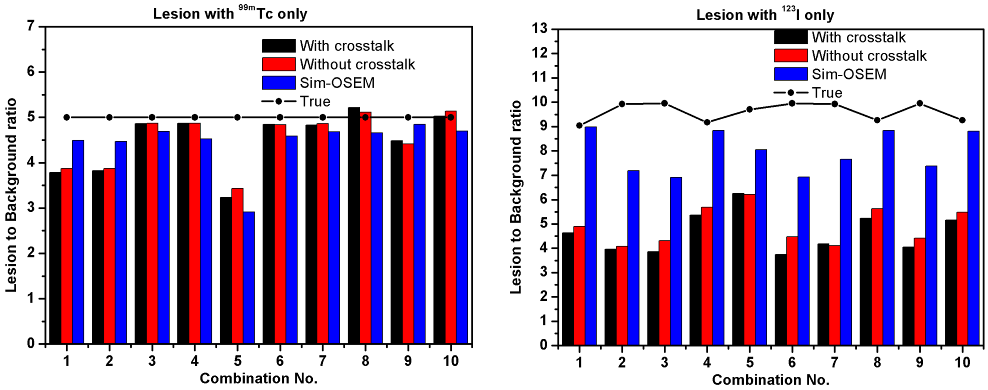

(a) Lesion to background ratios for lesions with ^{99m}Tc only

(b) Lesion to background ratios for lesions with ^{123}I only

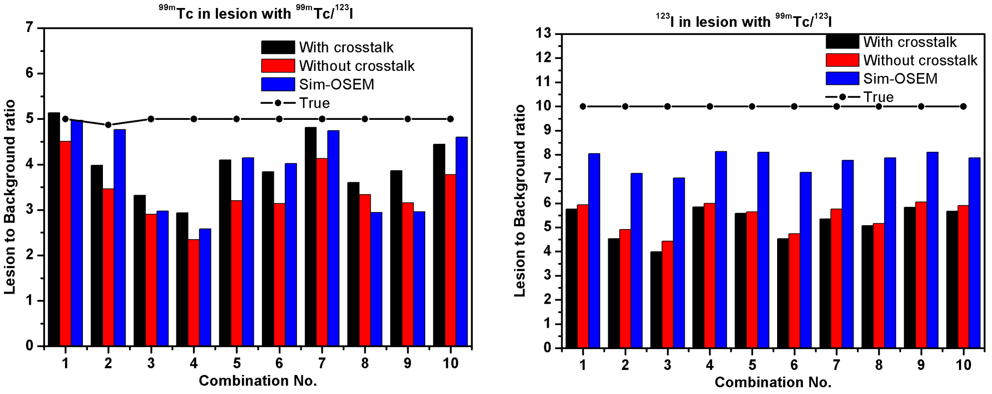

(c) ^{99m}Tc lesion to background ratios for lesions with ^{99m}Tc/^{123}I

(d) ^{123}I lesion to background ratios for lesions with ^{99m}Tc/^{123}I

Figure A.1: Comparison of lesion to background ratios estimated for different reconstruction methods with the true values of lesion to background ratios in the case of medium breast size.

Table A.4: Comparison of lesion to background ratios for large breast size for different reconstruction algorithms.

	Set No./ Isotope	1	2	3	4	5	6	7	8	9	10	**Mean**
True	^{99m}Tc	5.00	5.00	5.00	5.00	5.00	5.00	4.90	5.00	4.97	5.00	4.99±0.08
	^{99m}Tc†	5.00	5.00	5.00	5.00	5.00	4.97	5.00	5.00	5.00	5.00	5.00±0.03
	^{123}I*	10.00	10.00	10.00	10.00	10.00	10.00	10.00	10.00	10.00	10.00	10.00±0.00
	^{123}I	9.69	7.97	9.92	9.94	9.22	9.95	9.92	9.65	9.65	9.95	9.59±1.62
With Crosstalk	^{99m}Tc	3.89	3.25	2.53	4.38	3.90	4.25	3.46	3.46	4.17	4.01	3.73±1.20
	^{99m}Tc†	4.23	3.41	4.47	3.69	3.69	4.86	4.60	5.05	4.88	3.69	4.26±0.85
	^{123}I*	4.28	3.66	4.57	3.88	4.29	4.51	4.50	4.81	4.73	3.95	4.32±0.66
	^{123}I	3.94	4.39	4.00	4.51	4.90	4.09	4.00	4.08	3.81	4.01	4.17±0.73
Without Crosstalk	^{99m}Tc	3.89	3.25	2.53	4.38	3.90	4.25	3.46	3.46	4.17	4.01	3.73±1.20
	^{99m}Tc†	4.23	3.41	4.47	3.69	3.69	4.86	4.60	5.05	4.88	3.69	4.26±0.85
	^{123}I*	4.28	3.66	4.57	3.88	4.29	4.51	4.50	4.81	4.73	3.95	4.32±0.66
	^{123}I	3.94	4.39	4.00	4.51	4.90	4.09	4.00	4.08	3.81	4.01	4.17±0.73
Sim-OSEM	^{99m}Tc	4.53	4.67	2.76	4.94	4.67	4.94	4.93	4.22	4.87	4.60	4.51±1.76
	^{99m}Tc†	5.02	3.49	4.66	4.64	3.83	4.94	4.61	4.88	4.88	4.60	4.55±1.06
	^{123}I*	8.52	7.33	8.23	7.34	7.83	8.14	7.72	8.45	8.38	6.88	7.88±1.00
	^{123}I	8.52	9.15	7.70	7.67	8.95	8.16	7.67	8.63	8.71	7.87	8.30±0.85

† ^{99m}Tc lesion to background ratio for lesion with ^{123}I/^{99m}Tc.

⋆ ^{123}I lesion to background ratio for lesion with ^{123}I/^{99m}Tc.

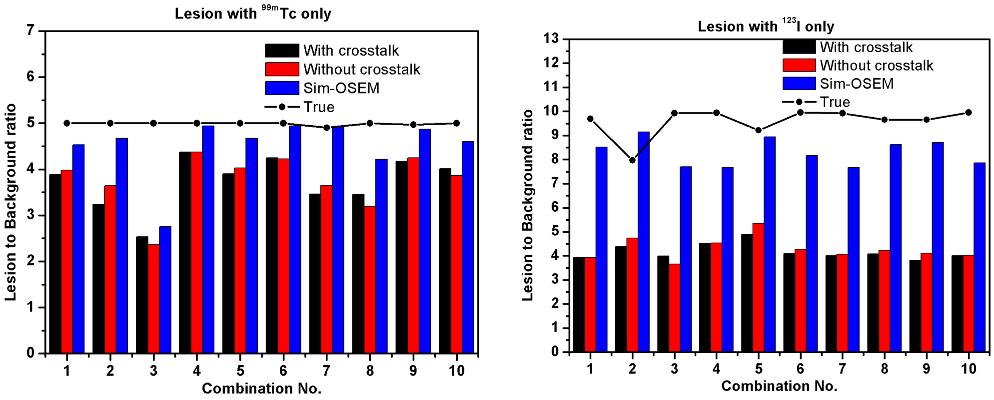

(a) Lesion to background ratios for lesions with ^{99m}Tc only (b) Lesion to background ratios for lesions with ^{123}I only

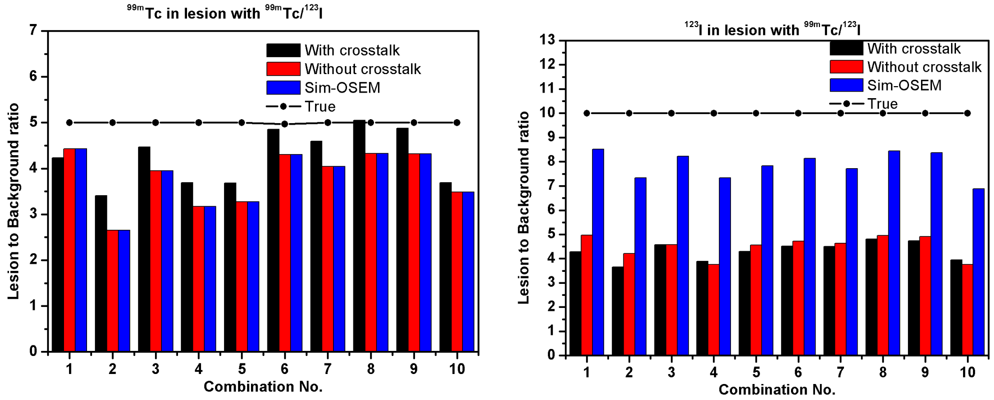

(c) ^{99m}Tc lesion to background ratios for lesions with ^{99m}Tc/^{123}I (d) ^{123}I lesion to background ratios for lesions with ^{99m}Tc/^{123}I

Figure A.2: Comparison of lesion to background ratios estimated for different reconstruction methods with the true values of lesion to background ratios in the case of large breast size.

Appendix B

Activity Estimation Data

Table B.5: Comparison of actual administered activity with activity values estimated using Sim-OSEM.

		^{99m}Tc Activity (MBq)			**^{123}I Activity (MBq)**		
Breast Size	No.	**Administered**	**Estimated**	**Error (%)**	**Administered**	**Estimated**	**Error (%)**
Small	1	140.94	140.98	0.02	9.06	8.76	-3.36
	2	148.99	148.38	-0.41	1.01	0.92	-8.48
	3	142.46	142.02	-0.31	7.54	7.43	-1.43
	4	142.67	142.59	-0.06	7.33	7.32	-0.16
	5	137.02	137.08	-0.05	12.98	12.92	-0.51
	6	149.00	149.27	0.18	1.00	0.94	-5.41
	7	140.68	140.57	-0.08	9.32	9.25	-0.75
	8	147.01	146.87	-0.09	2.99	2.78	-7.08
	9	142.67	143.04	0.26	7.33	7.34	0.18
	10	142.67	142.85	0.12	7.33	7.20	-1.78
Medium	1	138.78	139.42	0.46	11.22	10.69	-4.73
	2	144.93	144.62	-0.21	5.07	4.37	-13.82
	3	149.13	149.03	-0.07	0.87	0.77	-11.40
	4	143.43	143.85	0.29	6.57	6.62	0.64
	5	147.31	147.55	0.16	2.69	2.55	-5.13
	6	149.13	149.08	-0.03	0.87	0.73	-16.39
	7	147.34	146.81	-0.36	2.66	2.54	-4.53
	8	143.43	143.17	-0.18	6.57	6.49	-1.33
	9	149.14	149.62	0.32	0.86	0.79	-8.18
	10	141.80	141.89	0.06	8.20	8.13	-0.76
Large	1	141.80	142.11	0.22	8.20	7.88	-3.90
	2	138.85	139.07	0.16	11.15	10.04	-9.97
	3	147.18	146.82	-0.24	2.82	2.76	-2.27
	4	149.09	148.99	-0.07	0.91	0.80	-11.23
	5	143.08	142.97	-0.08	6.92	6.87	-0.66
	6	137.09	137.06	-0.02	12.91	12.37	-4.13
	7	147.20	147.12	-0.05	2.80	2.69	-4.17
	8	141.55	141.69	0.09	8.45	8.25	-2.37
	9	141.91	142.02	0.08	8.09	7.89	-2.49
	10	149.08	149.32	0.16	0.92	0.81	-11.65

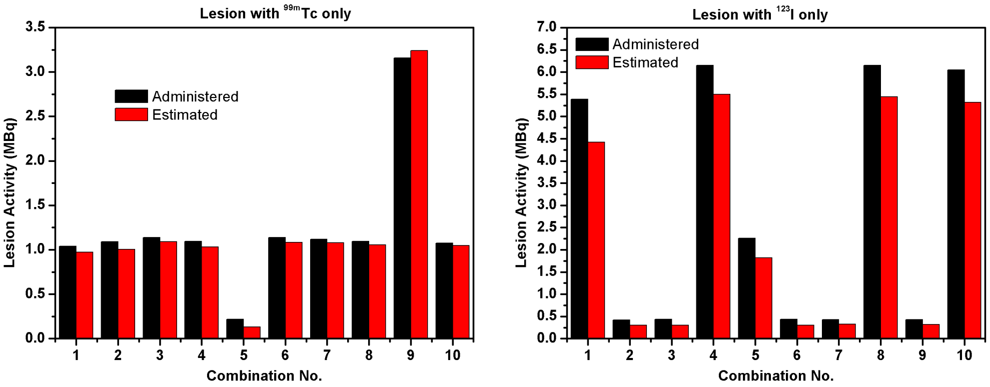

(a) Activity for lesion with ^{99m}Tc only. (b) Activity for lesion with ^{123}I only.

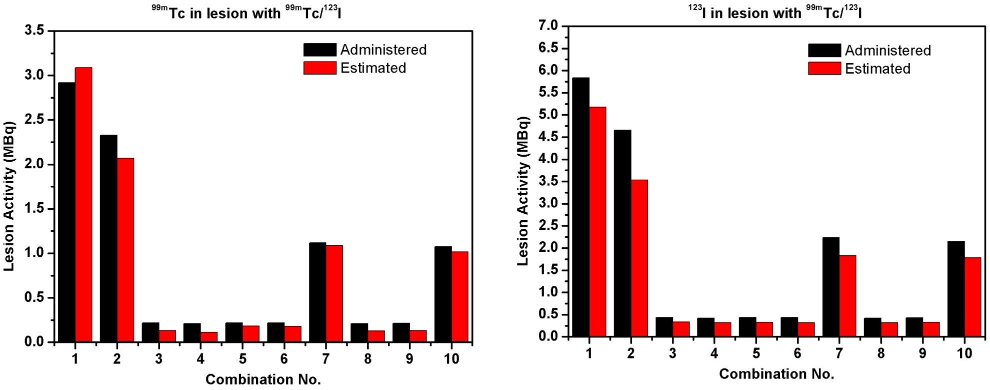

(c) ^{99m}Tc activity for lesion with ^{99m}Tc/^{123}I. (d) ^{123}I activity for lesion with ^{99m}Tc/^{123}I.

Figure B.3: Comparison of lesion activities estimated from Sim-OSEM with the actually administered lesion activities in the case of medium breast size.

Table B.6: Comparison between deposited and estimated lesion activities in case of small breast size.

No.		^{99m}Tc	^{99m}Tc†	^{123}I*	^{123}I
1	Deposited	1.20	3.39	6.78	2.28
	Estimated	1.08	3.41	5.85	1.71
2	Deposited	0.25	0.25	0.50	0.50
	Estimated	0.15	0.14	0.37	0.35
3	Deposited	0.24	0.24	0.48	7.06
	Estimated	0.13	0.14	0.35	5.99
4	Deposited	1.16	3.43	6.86	0.47
	Estimated	1.04	3.55	6.03	0.36
5	Deposited	3.16	3.25	6.49	6.49
	Estimated	3.06	3.27	5.60	5.58
6	Deposited	1.24	0.25	0.50	0.50
	Estimated	1.13	0.14	0.37	0.35
7	Deposited	1.16	1.22	2.44	6.87
	Estimated	1.01	1.11	1.96	5.97
8	Deposited	3.44	1.26	2.51	0.48
	Estimated	3.32	1.17	1.97	0.35
9	Deposited	1.22	3.43	6.86	0.47
	Estimated	1.11	3.49	6.06	0.37
10	Deposited	1.22	3.43	6.86	0.47
	Estimated	1.11	3.46	5.87	0.36

† ^{99m}Tc activity in lesion with ^{123}I/^{99m}Tc.

* ^{123}I activity in lesion with ^{123}I/^{99m}Tc.

Table B.7: Comparison between deposited and estimated lesion activities in case of medium breast size.

No.		^{99m}Tc	^{99m}Tc†	^{123}I*	^{123}I
1	Deposited	1.04	2.92	5.84	5.38
	Estimated	0.97	3.09	5.17	4.42
2	Deposited	1.09	2.33	4.66	0.42
	Estimated	1.00	2.07	3.53	0.30
3	Deposited	1.14	0.22	0.44	0.44
	Estimated	1.09	0.13	0.34	0.30
4	Deposited	1.09	0.21	0.42	6.15
	Estimated	1.03	0.11	0.32	5.50
5	Deposited	0.22	0.22	0.43	2.26
	Estimated	0.13	0.18	0.32	1.82
6	Deposited	1.14	0.22	0.44	0.44
	Estimated	1.08	0.18	0.32	0.30
7	Deposited	1.12	1.12	2.23	0.43
	Estimated	1.08	1.08	1.83	0.32
8	Deposited	1.09	0.21	0.42	6.15
	Estimated	1.05	0.13	0.32	5.44
9	Deposited	3.16	0.22	0.43	0.43
	Estimated	3.24	0.13	0.32	0.32
10	Deposited	1.07	1.07	2.15	6.05
	Estimated	1.05	1.02	1.78	5.32

† ^{99m}Tc activity in lesion with ^{123}I/^{99m}Tc.

* ^{123}I activity in lesion with ^{123}I/^{99m}Tc.

Table B.8: Comparison between deposited and estimated lesion activities in case of large breast size.

No.		^{99m}Tc	^{99m}Tc†	^{123}I*	^{123}I
1	Deposited	1.12	3.14	6.29	1.91
	Estimated	1.04	3.34	5.67	1.35
2	Deposited	0.22	0.22	0.43	10.72
	Estimated	0.20	0.15	0.32	8.73
3	Deposited	0.23	1.18	2.37	0.45
	Estimated	0.13	1.13	2.00	0.35
4	Deposited	3.33	0.23	0.45	0.45
	Estimated	3.50	0.22	0.34	0.35
5	Deposited	1.15	0.22	0.44	6.48
	Estimated	1.11	0.17	0.35	5.73
6	Deposited	2.92	6.25	12.51	0.40
	Estimated	3.05	6.69	11.02	0.32
7	Deposited	1.12	1.18	2.35	0.45
	Estimated	1.03	1.13	1.89	0.35
8	Deposited	0.22	3.16	6.32	2.13
	Estimated	0.18	3.28	5.68	1.66
9	Deposited	6.47	3.03	6.05	2.04
	Estimated	6.83	3.12	5.36	1.60
10	Deposited	1.20	0.23	0.46	0.46
	Estimated	1.13	0.21	0.32	0.36

† ^{99m}Tc activity in lesion with ^{123}I/^{99m}Tc.

* ^{123}I activity in lesion with ^{123}I/^{99m}Tc.

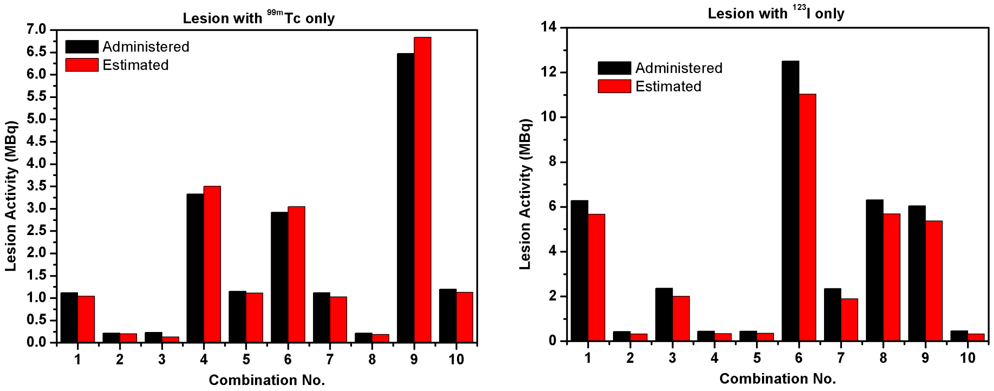

(a) Activity for lesion with ^{99m}Tc only. (b) Activity for lesion with ^{123}I only.

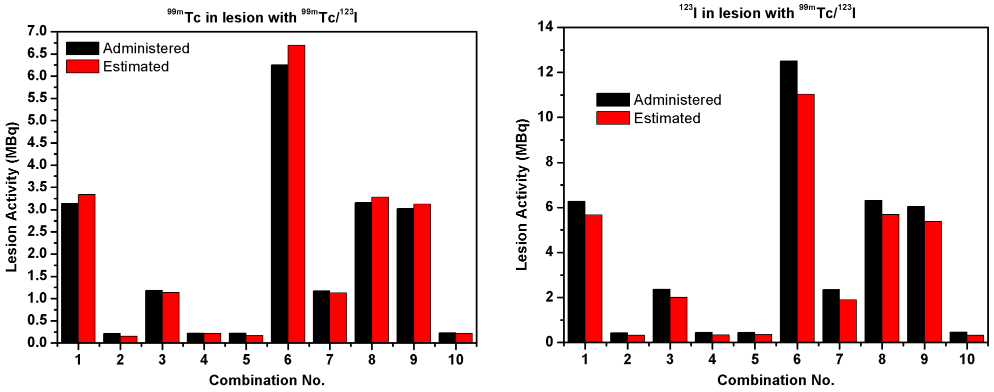

(c) ^{99m}Tc activity for lesion with ^{99m}Tc/^{123}I. (d) ^{123}I activity for lesion with ^{99m}Tc/^{123}I.

Figure B.4: Comparison of lesion activities estimated from Sim-OSEM with the actually administered lesion activities in the case of large breast size.

Bibliography

[1] S. R. Cherry, J. A. Sorenson, and M. E. Phelps, *Physics in Nuclear Medicine*, ch. Radionuclide and Radiopharmaceutical Production, pp. 45–64. Elsevier Science (USA), third ed., 2003.

[2] G. F. Knoll, *Radiation Detection and Measurements*, ch. Scintillation Detector Principles, pp. 220–247. Jhon Wiley & Sons Inc., third ed., 2003.

[3] S. R. Cherry, J. A. Sorenson, and M. E. Phelps, *Physics in Nuclear Medicine*, ch. The Gamma Camera: Performance Characteristics, pp. 227–252. Elsevier Science (USA), third ed., 2003.

[4] P. E. Kinahan, M. Defrise, and R. Cackdoyle, "Analytical image reconstruction methods," in *Emission Tomography: The Fundamentals of PET and SPECT* (M. N. Wernich and J. N. Aarvold, eds.), pp. 421–442, Nashville, Tennesee: Elsevier Academic Press, first ed., 2004.

[5] G. L. Zeng, *Medical Image Reconstruction: A Conceptual Tutorial*, ch. Iterative Reconstruction, pp. 125–167. Berlin, Heidelberg: Springer-Verlag, third ed., 2003.

[6] L. A. Shepp and Y. Vardi, “Maximum likelihood estimation for emission tomography,” *IEEE Trans. Med. Imaging*, vol. 1, pp. 113–121, 1982.

[7] K. Lange and R. Carson, “EM reconstruction for emission and transmission tomography,” *IEEE Trans. Med. Imaging*, vol. 8, pp. 306–316, 1984.

[8] H. M. Hudson and R. S. Larkin, “Accelerated image reconstruction using ordered subsets of projection data,” *IEEE Trans. Med. Imaging*, vol. 13, pp. 601–609, 1994.

[9] D. S. Lalush and B. M. W. Tsui, “Performance of ordered-subset reconstruction algorithm under attenuation and truncation in myocardial SPECT,” *J. Nucl. Med.*, vol. 41, pp. 737–744, 2000.

[10] C. R. Meyer, J. L. Boes, B. Kim, P. H. Bland, K. R. Zasadny, P. V. Kisan, K. Koral, K. A. Frey, and R. L. Wahl, “Demonstration of accuracy and clinical verstality of mutual information for automatic multimodality image using affine and thin plate spline warped geometric informations,” *Med. Imag. Anal.*, vol. 1, pp. 195–206, 1996.

[11] K. J. LaCroix, B. M. W. Tsui, B. H. Hasegawa, and J. K. Brown, “Investigation of the use of x-ray CT images for attenuation compensation in SPECT,” *IEEE Trans. Nucl. Sci.*, vol. 41, pp. 2793–2799, 1994.

[12] A. J. D. Silva, H. R. Tang, K. H. Wong, M. W. D. M C Wu, and B. H. Hasegawa, “Absolute quantification of regional mycardial uptake of ^{99m}Tc-sestamibi with SPECT: Experimental validation in a porcin model,” *J. Nucl. Med.*, vol. 48, pp. 58–64, 2001.

[13] D. L. Bailey, B. F. Hutton, and P. J. Walker, "Improved SPECT using simultaneous emission and transmission tomography," *JNM*, vol. 28, pp. 844–851, 1987.

[14] A. Celler, A. Sitek, E. Stoub, P. Hawman, R. Harrop, and D. Lyster, "Multiple line source array for SPECT transmission scans: simulation, phantom and patient studies," *JNM*, vol. 39, pp. 2183–2189, 1998.

[15] G. T. Gullberg, H. T. Morgan, G. L. Zeng, P. E. Christian, E. V. R. D. Bella, C. H. Tung, P. J. Maniawski, Y. L. Hsieh, and F. L. Datz, "The design and performance of a simultaneous transmission and emission tomography system," *IEEE Trans. Nucl. Sci.*, vol. 45, pp. 1676–1698, 1998.

[16] M. T. Madsen, P. T. Kirchner, J. P. Edlin, M. A. Nathan, and D. Kahn, "An emission based technique for obtaining attenuation correction data for mycardial SPECT studies," *Nucl. Med. Comm.*, vol. 14, pp. 689–695, 1993.

[17] T. S. Pan, M. A. King, D. S. Luo, S. T. Dhalberg, and B. J. Villegas, "Estimation of attenuation maps scatter and photopeak windows in single phton emission computed tomography," *J. Nucl. Card.*, vol. 4, pp. 42–51, 1997.

[18] A. Welch, R. Clark, F. Natterer, and G. T. Gullberg, "Towarsd accurate attenuation correction in SPECT without transmission measurements," *IEEE Trans. Med. Imag.*, vol. 16, pp. 532–541, 1997.

[19] L. T. Chang, "A method for attenuation correction in SPECT in radionuclide computed tomography," *IEEE Trans. Nucl. Sci.*, vol. 25, pp. 638–642, 1978.

[20] K. Murase, H. Itoh, and H. Mogami, “A comparative study of attenuation correction algorithms in single photon emission computed tomography(SPECT),” *J Nucl. Med.*, vol. 13, pp. 55–62, 1987.

[21] M. Ljunberg and S. E. Strand, “Attenuation correction in SPECT based on transmission studies and Monte Carlo simulations of build up functions,” *J Nucl. Med.*, vol. 31, pp. 493–500, 1990.

[22] M. A. King, B. M. W. Tsui, T. S. Pan, S. J. Glick, and E. J. Soares, “Attenuation compensation fo cardiac single photon emission computed tomographic imaging: Part2. attenuation compensation algorithms,” *J Nucl. Med.*, vol. 3, pp. 55–64, 1996.

[23] M. Ljunberg, M. A. King, G. J. Hademenos, and S. E. Strand, “Comparison of four scatter correction methods using Monte Carlo simulated source distribution,” *J Nucl. Med.*, vol. 35, pp. 143–151, 1994.

[24] M. A. King, G. J. Hademenos, and S. J. Glick, “A dual photopeak window method for scatter corection,” *J Nucl. Med.*, vol. 33, pp. 605–612, 1993.

[25] G. J. Hademenos, Dhalbon, Mand, and E. J. Hoffman, “Simultaneous dual-isotope Technetium-99m/Thallium-201 cardiac SPECT imaging using a projection-dependent spilldown correction factor,” *Eur. J. Nucl. Med.*, vol. 22, pp. 465–472, 1995.

[26] T. Ichihara, K. Ogawa, N. Motomura, A. Kubo, and S. Hashimoto, “Compton scatter compensation using triple energy window method for single and dual isotope SPECT,” *J. Nucl. Med*, vol. 34, pp. 2216–2221, 1993.

[27] B. Axelson, P. Msaki, and Israelson, “Subtraction of Compton Scatter photons in single-photon emission computed tomography,” *J. Nucl. Med.*, vol. 25, pp. 490–494, 1984.

[28] F. J. Beekman, H. W. A. M. deJong, and E. Slipjen, “Efficient SPECT scatter calculations in non-uniform media using correlated Monte Carlo simulation,” *Phys. Med. Biol.*, vol. 44, pp. 183–192, 1999.

[29] M. A. King, P. W. Doherty, and R. B. Schwinger, “Fast count dependant digital filtering of nuclear medicine images: concise communication,” *J. Nucl. Med.*, vol. 24, pp. 1039–1045, 1983.

[30] M. A. King, P. W. Doherty, and R. B. Schwinger, “A Weiner filter for nuclear medicine images,” *Med. Phys.*, vol. 10, pp. 876–880, 1983.

[31] M. A. King., R. B. Schwinger, and P. W. Doherty, “Two-dimensional filtering of SPECT images using the Metz and Weiner filters,” *J. Nucl. Med.*, vol. 25, pp. 1234–1240, 1984.

[32] H. Kiat, G. Germano, J. Frieman, K. V. Train, G. Silgan, and F. P. Wang, “Comparative feasibility of separate or simultaneous rest Tl-201/Stress Tc-99m sestamibi dual isotope perfusion SPECT,” *J. Nucl. Med.*, vol. 35, pp. 542–548, 1994.

[33] K. A. Williams, K. A. Hill, and M. C. Sheridan, “Noncardiac finding on dual isotope myocardial perfusion SPECT,” *J. Nucl. Cardiol.*, vol. 10, pp. 395–402, 2003.

[34] X. J. Yang, Y. M. He, Y. W. Wu, B. Zhang, H. Ji, T. B. Jiang, J. P. SOng, Z. H. Liu, and W. P. Jiang, "Hypoxia imaging of patients with acute myocardial infarction by using dual isotope ^{201}Tl and ^{99m}Tc-HL91.," *Nucl. Med. Comm.*, vol. 29, pp. 230–238, 2008.

[35] M. D. Devous., J. L. Lowe, and K. J. Payne, "Dual isotope brain SPECT imaging with ^{99m}Tc and ^{123}I: validation by phantom studies," *J. Nucl. Cardiol.*, vol. 10, pp. 395–402, 2003.

[36] H. I. Li, W. S. Huang, C. B. Yeh, M. H. Liao, C. C. Chen, S. H. S. Hen, J. C. Liu, and K. H. Ma, "Dual isotope SPECT for dopamine and serotonin transporters in normal and Parkinson monkey brains," *Nucl. Med. Biol.*, vol. 36, pp. 605–611, 2009.

[37] E. Hindie, D. Milliere, C. Jeanguillaume, L. Perlemuter, F. Chehade, and P. Galle, "Parathyroid imaging using simultaneous double window recording of Tc-99m sestamibi and I-123," *J. Nucl. Med.*, vol. 39, no. 6, pp. 1100–1105, 1998.

[38] S. C. Moore, R. J. English, C. Syravanh, D. E. Tow, R. E. Zimmerman, K. H. Chan, and M. F. Kijewski, "Simultaneous Tc-99m/Tl-210 imaging using energy based estimation of the spatial distribution of contaminant photons," *IEEE Trans. Nucl. Sci. trans*, vol. 42, no. 3, pp. 1189–1195, 1995.

[39] K. Knesaurek and J. Machac, "Comparison of correction techniques for simultaneous ^{201}Tl/^{99m}Tc myocardial perfusion SPECT imaging: a dog study," *Nucl. Med. Biol.*, vol. 45, pp. N167–N176, 2000.

[40] J. M. Links, J. L. Prince, and S. N. Gupta, “A vector Wiener filter for dual radionuclide imaging,” *IEEE Trans. Med. Imaging*, vol. 15, pp. 700–709, 1996.

[41] A. Tsuji, A. Kojima, M. Matsumoto, Y. Oyama, S. Tomiguchi, T. Kira, Y. Takagi, O. Shimomura, and M. Takashi, “A new method for crosstalk correction in simultaneous dual –isotope myocardial imaging with Tl-201 and I-123,” *Ann. Nucl. Med.*, vol. 13, no. 5, pp. 317–323, 1999.

[42] P. Hannequin, J. Mas, and G. Germano, “Photon energy recovery for crosstalk correction in simultaneous ^{99m}Tc/^{201}Tl imaging,” *J. Nucl. Med.*, vol. 41, no. 4, pp. 728–736, 2000.

[43] E. C. Frey and B. M. W. Tsui, “A new method for modeling the spatially variant, object shape dependent scatter response function in SPECT,” in *IEEE Nuclear Science Symp.*, vol. 2 of *Conf. Proc.*, pp. 1082–1086, IEEE, IEEE, 1996.

[44] W. T. Wang, E. C. Frey, B. Tsui, and C. Tocharoenchai, “A model-based crosstalk compensation method for simultaneous Tl-201 and Tc-99m dual isotope myocardial SPECT imaging,” in *IEEE Medical Imaging Conf.*, vol. 4, pp. 1732–1736, 2001.

[45] Y. Du and E. C. Frey, “Quantitative evaluation of simultaneous reconstruction with ’ model-based crosstalk compensationTc-99m/I-123 dual isotope simultaneous acquisition brain SPECT,” *Med. Phys.*, vol. 36, no. 6, pp. 2021–2033, 2009.

[46] X. Song, E. C. Frey, W. T. Wang, Y. Du, and B. M. W. Tsui, “Validation and evaluation of model-based crosstalk compensation method in simultaneous

^{99m}Tc stress and ^{201}Tl rest myocardial perfusion SPECT," *IEEE Trans. Nucl. Sci.*, vol. 51, no. 1, pp. 72–79, 2004.

[47] G. E. Fakhri, P. Maksud, M. F. Kijewski, M. O. Hebert, T. Pokropek, A. Aurengo, and S. C. Moore, "Scatter and crosstalk correction in simultaneous Tc-99m/I-123 brain SPECT using constraint factor analysis and artificial neural networks," *IEEE Trans. Nucl. Sci.*, vol. 47, no. 4, pp. 1573–1580, 2000.

[48] M. X. Zheng, I. G. Zubal, J. P. Seibyl, and M. A. King, "Correction for crosstalk contamination in dual radionuclide ^{99m}Tc and ^{123}I images using artificial neural network," *IEEE Trans. Nucl. Sci.*, vol. 51, no. 5, pp. 2649–2653, 2004.

[49] C. J. Chang, W. S. Huang, K. H. Su, and J. C. Chen, "Separation of two radionuclides in simultaneous dual-isotope imaging with independent component analysis," *Biomed. Eng. Appl. Basis Comm.*, vol. 18, pp. 264–269, 2006.

[50] H. B. Yang, S. J. Wang, J. S. Lee, M. L. Jan, C. J. Chang, and J. C. Chen, "Physical Phantom evaluation of simultaneous ^{99m}Tc and ^{123}I SPECT imaging," *Nucl. Instr. and Meth A.*, 2010.

[51] J. Bai, J. Hashimoto, K. Ogawa, T. Nakahara, T. Suzuki, and A. Kubo, "Scatter correction based on an artificial neural network for ^{99m}Tc and ^{123}I dual isotope SPECT in myocardial and brain imaging," *Ann. Nucl. Med.*, vol. 21, no. 1, pp. 25–32, 2007.

[52] S. Shcherbinin, A. Celler, M. Trummer, and T. Humphries, "An APD-based iterative reconstruction method for simultaneous ^{99m}Tc/^{123}I SPECT imaging," *Physica Medica*, vol. 25, pp. 192–200, 2009.

[53] H. W. A. M. deJong, F. J. Beekman, M. A. Viergever, and P. P. vanRijk, “Simultaneous ^{99m}Tc/^{201}Tl dual-isotope SPET with Monte Carlo-based down-scatter correction,” *Eur. J. Nucl. Med.*, vol. 28, no. 8, pp. 1063–1071, 2002.

[54] M. Ljunberg and S. E. Strand, “A Monte Carlo Program for the simulation of scintillation camera characteristics,” *Comput. Methods Programs Biomed.*, vol. 29, pp. 257–272, 1989.

[55] W. H. Press, S. A. Teukolsky, W. T. Vetterling, and B. P. Flannery, *Numerical Recipes in Fortran 77: The Art of Scientific Computing*, vol. 1 of *Numerical Recipes in Fortran 77*, ch. Random Numbers, pp. 267–269. Cambridge University Press, 2 ed., 1997.

[56] M. Ljunberg, *Monte Carlo Calculations in Nuclear Medicine*, ch. Introduction to Monte Carlo Methods, pp. 1–12. Medical Science Series, Institute of Physics Publishing, London, 1998.

[57] C. Levin, “Basic physics of radionuclide imaging,” in *Emission Tomography: The Fundamentals of PET and SPECT* (M. N. Wernich and J. N. Aarvold, eds.), pp. 153–168, Nashville, Tennesee: Elsevier Academic Press, first ed., 2004.

[58] M. J. Berger and J. H. Hubbell, *XCOM: Photon cross sections on a personal computer.* National Bureau of Standard, 1987.

[59] S. Weinberg, ed., *The Quantum Theory of Fields.* United Kingdom: Cambridge University Press, 1995.

[60] M. Ljunberg, A. . Larsson, and L. Johansson, “A new collimator simulation in

simind based on the delta-scattering technique," *IEEE Trans. Nucl. Sci.*, vol. 52, no. 5, pp. 1370–1375, 2005.

[61] M. Ljunberg, "Simulation techniques and phantoms," in *Emission Tomography: The Fundamentals of PET and SPECT* (M. N. Wernich and J. N. Aarvold, eds.), pp. 551–563, Nashville, Tennesee: Elsevier Academic Press, first ed., 2004.

[62] S. Liu, M. A. King, A. B. Brill, M. G. Stabin, and T. H. Farncombe, "Accelerated SPECT Monte Carlo simulation using multiple projection sampling and convolution based force detection," *IEEE Trans. Nucl. Sci.*, vol. 55, no. 1, pp. 560–567, 2008.

[63] W. P. Segars, *Development and application of the new dynamic NURBS-based cardiac-torso (NCAT) phantom.* PhD thesis, Biomedical Engineering, University of North Carolina: Chapel Hill, NC, 2001.

[64] L. Zhou, J. Oldan, P. Fisher, and G. Gindi, "Low-contrast lesion detection in tomosynthesis breast imaging using a relealistic breast phantom," in *SPIE Proceeding*, 2006.

[65] K. Bliznakova, Z. Bliznakov, V. Bravou, Z. Kolitsi, and N. Pallikarakas, "A three dimensional breast software phantom for mammography simulation," *Phys. Med. Biol.*, vol. 48, pp. 3699–3719, 2003.

[66] J. Ouyang, G. E. Fakhri, and S. C. Moore, "Fast Monte Carlo based joint iterative reconstruction for simultaneous ^{99m}Tc/^{123}I SPECT imaging," *Med. Phys.*, vol. 34, no. 8, pp. 3263–3272, 2007.

[67] M. J. Blend and V. A. Bhadkamkar, "Impact of radioimmunoscintigraphy on management of colorectal and ovarian cancer patients: a retrospective impact of radioimmunoscintigraphy on management of colorectal and ovarian cancer patients: a retrospective study," *Cancer Invest.*, vol. 16, pp. 431–441, 1998.

[68] J. C. Quintana and M. J. Blend, "The dual-isotope prostascint imaging procedure: clinical experience and staging results in 145 patients," *Clin. Nucl. Med.*, vol. 25, pp. 33–40, 2000.

[69] F. Bénard and É. Turcotte, "Imaging in breast cancer: Single-photon computed tomography and positron-emission tomography," *Breast Cancer Research*, vol. 7, pp. 153–162, 2005.

[70] E. Hsiao, T. Huynh, R. Mansberg, G. Bautovich, and P. Roach, "Diagnostic I-123 Scintigraphy to Assess Potential Breast Uptake of I-131 Before Radioiodine Therapy in a Postpartum Woman With Thyroid Cancer," *Clin. Nucl. Med.*, vol. 29, no. 8, pp. 498–501, 2004.

[71] T. Y. T. Wang and J. M. Phang, "Effects of Estrogen on Apoptotic Pathways in Human Breast Cancer Cell Line MCF-7," *Cancer Research*, vol. 55, pp. 2487–2489, 1995.

[72] S. B. Haim, K. Kacperski, S. Hain, D. V. Gramberg, K. E. B F Hutton, N. Roth, W. A. Waddington, D. S. Berman, and P. J. Ell, "Simultaneous dual-radionuclide myocardial perfusion imaging with solid state dedicated cardiac camera," *Eur. J. Nucl. Med.*, vol. 37, pp. 1710–1721, 2010.

[73] W. T. Wang, B. M. W. Tsui, D. S. Lalush, C. Tocharoenchai, and E. C. Frey,

"Optimization of acquisition parameters for simultaneous ^{201}Tl and ^{99m}Tc dual-isotope myocardial imaging," *IEEE Trans. Nucl. Sci.*, vol. 52, no. 5, pp. 1227–1235, 2005.

[74] Y. Du, E. C. Frey, W. T. Wang, and B. M. W. Tsui, "Optimization of acquisition energy windows in Simultaneous ^{99m}Tc/^{123}I brain SPECT," *IEEE Trans. Nucl. Sci.*, vol. 50, no. 5, pp. 1556–1561, 2003.

[75] X. Song, E. C. Frey, X. He, W. P. Segars, and B. M. W. Tsui, "A mathematical observer study for evaluation of a model-based compensation method for crosstalk in simultaneous dual isotope SPECT," in *IEEE Nuclear Science Symposium Conference Record*, 2003.